Check for updates

Interdisciplinary Materials

WILEY

Interdisciplinary Materials Open Access

REVIEW OPEN ACCESS

Advanced Functional Materials for Marine Energy Utilization

Qiang Yu[1,2] | Peipei Ge[2] | Fazhou Wang[1,3] | Shichao Bi[1] | Bo Tang[1] | Ion Tiginyanu[4] | Kenneth I. Ozoemena[5] | Xiao-Yu Yang[1,3]

[1]Laoshan Laboratory, Qingdao, China | [2]Qingdao Marine Science and Technology Center, Qingdao, China | [3]State Key Laboratory of Silicate Materials for Architectures & State Key Laboratory of Advanced Technology for Materials Synthesis and Processing & School of Chemistry, Chemical Engineering and Life Sciences, Wuhan University of Technology, Wuhan, China | [4]National Center for Materials Study and Testing, Technical University of Moldova & Academy of Sciences of Moldova, Chisinau, Republic of Moldova | [5]Molecular Sciences Institute, School of Chemistry, University of the Witwatersrand, Johannesburg, South Africa

Correspondence: Fazhou Wang (fzhwang@whut.edu.cn) | Bo Tang (tangb@sdnu.edu.cn) | Xiao-Yu Yang (xyyang@whut.edu.cn)

Received: 11 October 2025 | **Revised:** 9 March 2026 | **Accepted:** 9 March 2026

Funding: Major Program (JD) of Hubei Province, Grant/Award Number: 2023BAA003; National Natural Science Foundation of China, Grant/Award Numbers: 52130208, 42406221; Key R&D Program of Shandong Province, Grant/Award Number: 2023CXGC010314; Laoshan Laboratory, Grant/Award Number: LSKJ202501700; South Africa's DSI-NRF-Wits SARChI Chair in Materials Electrochemistry and Energy Technologies, Grant/Award Numbers: MEET, UID #132739; Shandong Institute of Chinese Engineering S&T Strategy for Development, Grant/Award Number: 202502SDZD02

Keywords: environmental durability | marine energy materials | marine energy utilization

ABSTRACT

Several features of marine energy, including large reserves, sustainable utilization, environmental friendliness, make it a promising area of exploration. In recent years, the progress in the material sciences has promoted a rapid development of materials that are vital for the conversion, storage, and transmission of renewable marine energy. However, the excessively large restrictions that are placed on materials used in marine environments have given an impetus to continued studies in this area. Thus far, few reports exist that categorize and integrate the types and requirements of materials that are employed for capturing, converting and storing marine energy. The goal of this review is to provide a detailed description of advanced materials that have been developed for use in these purposes. The review contains sections that cover materials used in (1) the capture and conversion of energy arising from ocean phenomena including tidal, wave and current fluctuations, and thermal and salinity gradients, (2) systems for the transmission of marine energy derived power including submarine cables and hydrogen production, and (3) electrodes for lithium-ion batteries and supercapacitors for marine energy storage and utilization. Finally, the review contains a brief discussion of shortcomings of materials used currently for marine energy purposes, and proposals that could advance the industrialization of power generation using marine energy sources.

1 | Introduction

In conjunction with the rapid growth of the global population and complexity, the demand for energy has dramatically increased. The continuing use of non-renewable resources such as fossil fuels, coal, and oil for energy production has led to serious economic and environmental problems. Owing to these issues, greater worldwide attention has been given to the development of systems for efficient conversion of solar, wind, and marine energy [1–4]. In this group, ocean-derived marine energy has attracted enhanced attention owing to its large quantity, wide distribution, renewability, and low level of pollution. Oceans receive, store, and emit energy that can be

This is an open access article under the terms of the Creative Commons Attribution License, which permits use, distribution and reproduction in any medium, provided the original work is properly cited.

© 2026 The Author(s). *Interdisciplinary Materials* published by Wuhan University of Technology and John Wiley & Sons Australia, Ltd.

harvested using a variety of physical processes that are linked to ocean tides, waves, currents, and thermal and salinity gradients [5]. The long history of the utilization of these forms of marine energy is summarized in Figure 1. The earliest human use of marine energy can be traced back to the development of tidal mills, exemplified by the preserved mill in Suffolk, England, which dates back to 12th century [6]. In the 1950s, 42 tidal power plants were constructed to capture tidal energy generated along the coast of China [7].

The world's first patent for a system that utilizes wave energy was filed by the French scientist, Girard, in 1799, which stimulated many later studies of this technology [8]. In the 1940s, the father of modern wave energy technology, Yoshio Masuda, invented a buoy-based oscillating water column power generation device. This topic was described in a 1974 publication in the *Nature* magazine authored by S.H. Salter, who proposed several wave power generation devices and energy storage schemes [9]. The French physicist Arsonval in 1881 formulated the first system that employs ocean thermal gradients to generate energy [10], and his student G. Claude utilized this design to build an experimental device that demonstrated the plausibility of ocean thermoelectric power generation. In 1930, the world's first seawater thermal power station was fabricated in the Cuban seaside. Generation of energy using the ocean's salinity gradient was proposed in 1939, and in a 1954 publication, R.E. Pattle first introduced the concepts of osmotic energy and salinity gradients [11]. In 1973, the Israeli, Sidney Loeb, demonstrated experimentally that a salinity gradient-driven energy system for power generation is feasible. Research in China targeted at the development of systems for salinity gradient energy power generation began in 1979, and in 1985, a salt differential laboratory power generation device that utilizes a semipermeable membrane was developed in Xi'an. The range of electric power generation using this system was 0.9–1.2 W.

With the rapid development of advanced manufacturing technologies and new materials, the exploration of marine energy has become more sophisticated. It is worth noting at this point that the form which specific marine energy sources take is geographical location dependent. For example, the earliest and now most mature marine tidal energy resource is mainly located in estuaries and waterways, such as those that are present along the East China Sea and the western European coasts [12]. In addition, the best locations for wave energy systems are along ocean coastlines at mid-high latitudes (40°–60°) such as those found along the northwestern coast of the United States, and other regions that experience significant wind fields [13]. Open ocean currents for energy production are generally located along the Gulf Stream in the Atlantic and the Kuroshio in the Pacific [14, 15]. Acceptable thermal gradients for energy generation present in specific locations in the 0°–35° latitude regions [16], while locations for optimal salinity gradient-derived energy are at river-sea junctions where salt concentration differences are high [17].

Although large fluctuations exist in the locations of different types of marine energy sources, the reserves of energy at each are astonishingly large. The yearly world tidal (including current energy), wave, and thermal and salinity gradient energy reserves are 1200, 29 500, 44 000, and 1650 TWh, respectively [18–20]. Because worldwide annual electricity consumption is about 20000 TWh, harvesting only a fraction of the marine energy would meet mankind's electricity needs. Owing to the significance of its potential annual output and renewability, marine energy requires great attention [21–23].

The ability to effectively utilize marine energy depends on several factors, including geographical location relative to that of seacoasts, seawater depth and government policies in these areas, and the efficient use of materials to construct the device. Among issues that need to be considered is the complex environment of the ocean including a high degree of corrosion caused by chloride ion and fouling caused by biological components in seawater, both of which place high demands on the design and performance of materials employed in devices [24–26]. In recent years, advances in materials science have expanded the breadth and depth of marine renewable energy system designs. Nanocomposite materials with special functions such as those that are corrosion, pressure and temperature

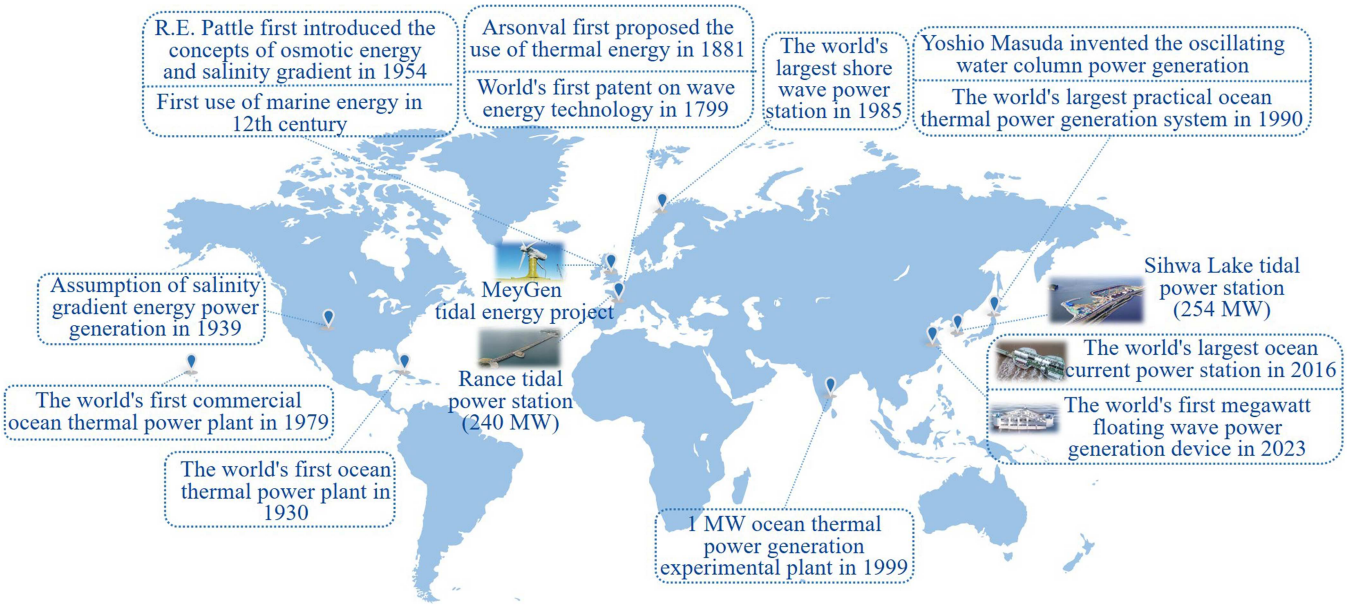

FIGURE 1 | History of marine energy generation.

2767441x, 2026, 3, Downloaded from https://onlinelibrary.wiley.com/doi/10.1002/idm2.70047 by Battelle Memorial Institute Pacific Northwest Division, Wiley Online Library on [22/06/2026]. See the Terms and Conditions (https://onlinelibrary.wiley.com/terms-and-conditions) on Wiley Online Library for rules of use; OA articles are governed by the applicable Creative Commons License

resistant, and that have anti-biological fouling properties have been developed and applied to devices for conversion, transmission, storage and utilization of marine energy. However, consensus has not yet been reached about optimal materials that should be employed for exploitation of marine energy. Aiming at the goal of bridging this gap, this review categorizes and describes materials involved in the capture/conversion, transmission and storage/utilization of marine energy in a detailed manner (Figure 2). Also, applications and unique functions of different materials in marine energy systems, including metals, organic polymers, inorganic nonmetals and composite materials are summarized and discussed in the context of their contribution to the development of novel marine energy systems.

2 | Materials for Marine Energy Capture and Conversion

At the present time, marine energy is mainly harvested for use in power generation. The capacity of existing systems for generating global marine energy-derived power is about 625 MW [27]. The assessment of the potential of marine energy is helpful to select available sites and develop the appropriate capacity for the utilization of marine energy, as well as to determine the most appropriate type of energy converters. Many kinds of materials are involved in the processes for converting marine energy into electrical energy, including metals, inorganic non-metals, and polymers. In the following sections, materials employed in the processes for capture and conversion of tidal, wave, ocean current and thermal energy, and salinity gradient energy into electrical energy will be discussed in detail.

2.1 | Materials for Tidal Energy Systems

Tidal energy, one of the most available marine sources, is associated with gravitational interactions between the moon and Earth, along with the Earth's rotation [15]. These forces cause seawater to flow back and forth between the ocean and coastline that results in periodic fluctuation of sea levels. Tidal energy derives from reversibly changing potential energies

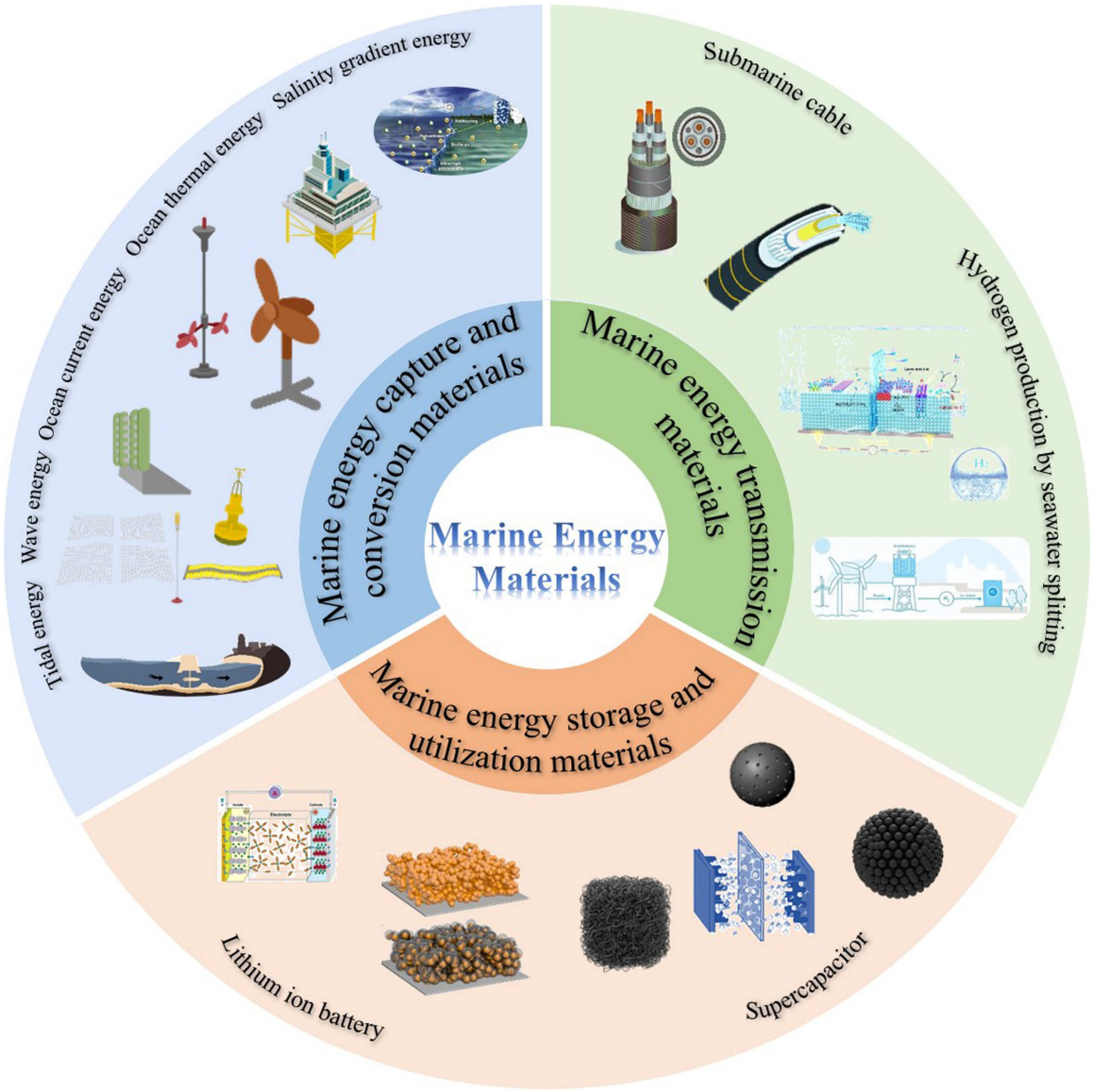

FIGURE 2 | Classification of marine energy materials in this review.

2767441x, 2026, 3, Downloaded from https://onlinelibrary.wiley.com/doi/10.1002/idm2.70047 by Battelle Memorial Institute Pacific Northwest Division, Wiley Online Library on [22/06/2026]. See the Terms and Conditions (https://onlinelibrary.wiley.com/terms-and-conditions) on Wiley Online Library for rules of use; OA articles are governed by the applicable Creative Commons License

associated with sea level differences on the sides of dams placed at inlets of coastal waters. The tide promoted reversible flow of water is then used to drive electricity-generating hydraulic turbines (Figure 3A). As a result, a wide variety of materials are involved in the tidal power generation process, including those used in turbines, dams, waterways, bearings and seals [30].

2.1.1 | *Surface Coating Materials for Hydraulic Turbines*

Hydraulic turbines are composed of blades, bearings, sealing sleeves and other structural components that function in the cascade involved in converting the kinetic energy of flowing water into mechanical energy and then electrical energy. Because components of hydraulic turbines are in contact with seawater over long time periods, they need to be composed of materials that resist corrosion and biofouling.

Surface coatings materials such as inorganic hard layers (oxides, carbides, and nitrides), polymer-based soft layers, and reinforced composite cermet coatings are commonly used to protect turbine components. Mann et al., in a systematic investigation of the effects of coatings on the corrosion, demonstrated that tungsten carbide coating applied using high velocity oxy-fuel (HVOF) creates a remarkably elevated corrosion resistance [31]. The results of studies by Mann on the effect of hard coatings on deleterious high-energy impacts show that borided T410 steel effectively blocks crack and void formation [32]. Grewal et al. utilized Ni–Al_2O_3-based composite coatings applied using a high velocity flame spray (HVFS) system, to form a highly microhard coating having an Al_2O_3 content of 60 wt% [33]. In addition, Zhang et al. prepared fluorinated polyurethane coatings that significantly improve the anti-corrosion performance of materials in a manner that is dependent on the fluorine content of the polymer [34]. Lastly, Syamsundar et al. demonstrated that a 20 wt% B_4C and 10 wt% SiC nanoparticle-reinforced polyurethane coating possesses optimal corrosion resistance and a low production cost [35]. Furthermore, superhydrophobic coatings not only effectively separate surfaces from seawater to prevent corrosion, but they also impart low friction resistance, self-cleaning, anti-icing and -biological fouling [36]. Haghighi et al. showed that a superhydrophobic coating causes turbine blades to have an increased efficiency by ca. 4% and significantly reduced energy consumption at guide vanes and draft tubes (Figure 3B,C) [28].

The development of these coatings is fundamentally driven by the need to mitigate synergistic failure modes, such as erosion–corrosion and fatigue under cavitation, which dictate the long-term service life of turbine components in seawater. Thus, consideration needs to be given to requirement that coating materials on turbine components must have multifunctional properties, including resistance to cavitation, corrosion, and wear, along with light weights, high vibration damping and

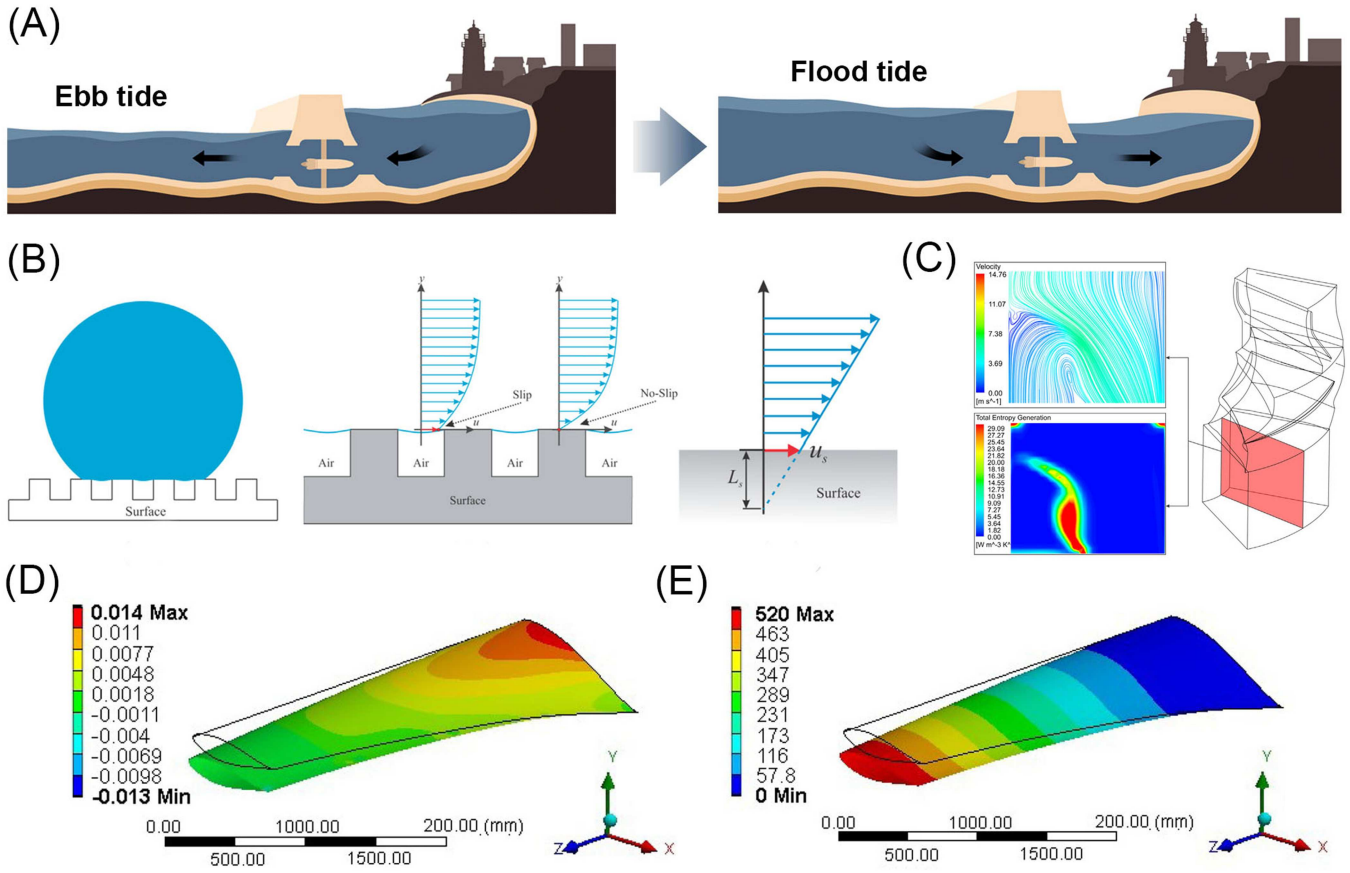

FIGURE 3 | (A) Schematic of tidal power generation. (B) Surface slip mechanism of superhydrophobic material coatings. (C) 2D streamlines at the central axial plane of the draft tube and contour of the total entropy generation rate at the same plane for $Q = 26$ m^3/s. Reproduced with permission [28]. Copyright 2020, Elsevier. Finite Element contour plots of (D) flap-wise strain distribution and (E) tip deflection of GFRP composite blade due to a tidal current velocity of 7 m/s. Reproduced with permission [29]. Copyright 2021, Elsevier.

2767441x, 2026, 3, Downloaded from https://onlinelibrary.wiley.com/doi/10.1002/idm2.70047 by Battelle Memorial Institute Pacific Northwest Division, Wiley Online Library on [22/06/2026]. See the Terms and Conditions (https://onlinelibrary.wiley.com/terms-and-conditions) on Wiley Online Library for rules of use; OA articles are governed by the applicable Creative Commons License

hydrophobicity, and smooth adhesion to base material. Unfortunately, many studies carried out thus far have failed to account for the need for this level of versatility. Consequently, an urgent demand exists for surface coating materials for hydraulic turbines that have low cost, multiple functions, long lifetimes and environmental friendliness.

2.1.2 | *Substrate Composite Materials for Hydraulic Turbines*

Introduction of coating materials requires a second phase in the construction of hydraulic turbines. To avoid this added step, methods for direct preparation of corrosion-resistant, high-strength, and lightweight hydraulic turbines that do not require secondary application of coatings should be more efficient. Owing to their high stiffness, light weight, corrosion resistance, easy shaping and reasonable cost, composite materials have been employed to form turbine blades [30]. Compared with those generated using traditional stainless steel, turbine components prepared from composite materials have 80% lower weights, and densities in range of 1500–2500 kg/m^3.

Recently, fiber reinforced composites have been adopted for construction of turbine blades that possess improved strengths and stiffness [37]. The fiber reinforcement phase of these materials, typically composed of glass, carbon and aramid fiber, is encased in the matrix phase of polymers. Unlike their steel counterparts, composite blades do not require expensive anti-corrosion coatings. The first tidal turbine prototype (SeaGen) employed carbon/glass fiber composites. This device has advantages of having a light weight, high stiffness, an effective strength to weight ratio and high ease of formation. Significantly, Jaksic et al. showed that the weight of turbine blades is significantly reduced when a carbon fiber reinforced composite is utilized instead of a glass fiber reinforced composite [38]. Furthermore, Gonabadi et al. predicted that glass fiber composite blade laminates need to be three times thicker than carbon fiber composite blades to enable safe operation of equipment (Figure 3D,E) [29].

Although having obvious advantages in hydraulic turbine applications, composite materials have not been widely used due to their high costs. In addition, composites generally have higher deformabilities, which would negatively impact high-speed rotating turbines. More advanced materials and technologies, including graphene-based materials and 3D printing, need to be developed to meet the rapidly growing demand for tidal energy.

2.1.3 | *Materials for Dams and Bearings*

Dams for temporary storage and release during tide cycles have traditionally been constructed using reinforced concrete. In recent years, novel dam materials such as glass fiber reinforced and rock-filled concrete, bituminous conglomerates, and inflatable rubber have been developed for this purpose. Liu et al. created a novel cement having superhydrophobicity and self-cleaning properties by transferring the lotus-leaf-like microstructure to the cement surface by using a nano-casting technology [39]. In another effort, You et al. probed the corrosion behavior of different rebars in cements in tidal environments [40]. The results show that the addition of steel slag caused refinement of the interface between the rebar and mortar, thus reducing corrosion. Concretes containing various chemical additives and installed using advanced casting technologies have been shown to have significantly improved anti-corrosion properties, structural stability and durability.

Materials that reduce friction in components of hydraulic turbines have received attention. At the current time, self-lubricating bearings, fabricated using polytetrafluoroethylene (PTFE) and possessing an extremely low friction coefficient, have been employed in turbines. In recent years, advanced materials, including carbon nanotube (CNT) and graphene-based polymer composites, have been developed to effectively solve problems associated with bearing friction and wear [41]. Moreover, pressurized fluids composed of water-based and ecological/vegetable lubricant oils have been used to lubricate turbine bearings.

2.2 | Materials for Wave Energy Systems

Wave-promoted power generation is the second most rapidly developing marine energy technology. So far, Japan, the United Kingdom, the United States, and China have built wave power generation devices that either float on the ocean or are anchored underwater (Figure 4A). Wave energy is widely distributed and has high energy density (Figure 4B). This conclusion is demonstrated by the fact that wave-associated devices have the potential of producing about 200 MW per second over 1 km^2 of the ocean surface.

A wave energy converter (WEC) is a device that captures and converts wave energy into electricity. Falcao and Drew et al. have provided a detailed review of the types of advanced technology WEC devices that have been designed [46, 47]. The thousands of WEC devices probed thus far can be classified into six categories according to their mode of operation, including point absorbers, oscillating water columns, submerged pressure differential devices, oscillating wave surge converters, attenuators, terminators, and overtopping devices. Constraints on WECs and their operating environments must be fully understood to design efficient and durable materials for their construction.

In most WECs, a rotary power generator is driven by an air/hydraulic turbine or hydraulic motor. Therefore, materials selected for most WECs are similar to those employed to fabricate the tide energy system described in Section 2.1 and are not discussed in this section. Instead, materials employed in the fabrication of novel WECs such as triboelectric nanogenerators (TENGs) will be covered. TENGs serve as an emerging material-centric approach with distinct potential for specific applications, and therefore, it represents a complementary research frontier in marine energy conversion materials.

Collection and conversion of wave energy using TENGs has the advantageous feature of high efficiency at low operating frequency [48, 49]. TENGs operate at up to a 55% instantaneous energy conversion efficiency and 1200 W/m^2 power density [50]. Electricity generation in TENGs occurs through the triboelectric effect caused by coupling the effects of contact electrification and electrostatic induction when two materials change from a contacted to a separated state. A key approach to improve the wave energy conversion efficiency of a TENG is to utilize two large charge density triboelectric materials ranging from polymers to metals that have large differences in their electron affinities.

2767441x, 2026, 3, Downloaded from https://onlinelibrary.wiley.com/doi/10.1002/idm2.70047 by Battelle Memorial Institute Pacific Northwest Division, Wiley Online Library on [22/06/2026]. See the Terms and Conditions (https://onlinelibrary.wiley.com/terms-and-conditions) on Wiley Online Library for rules of use; OA articles are governed by the applicable Creative Commons License

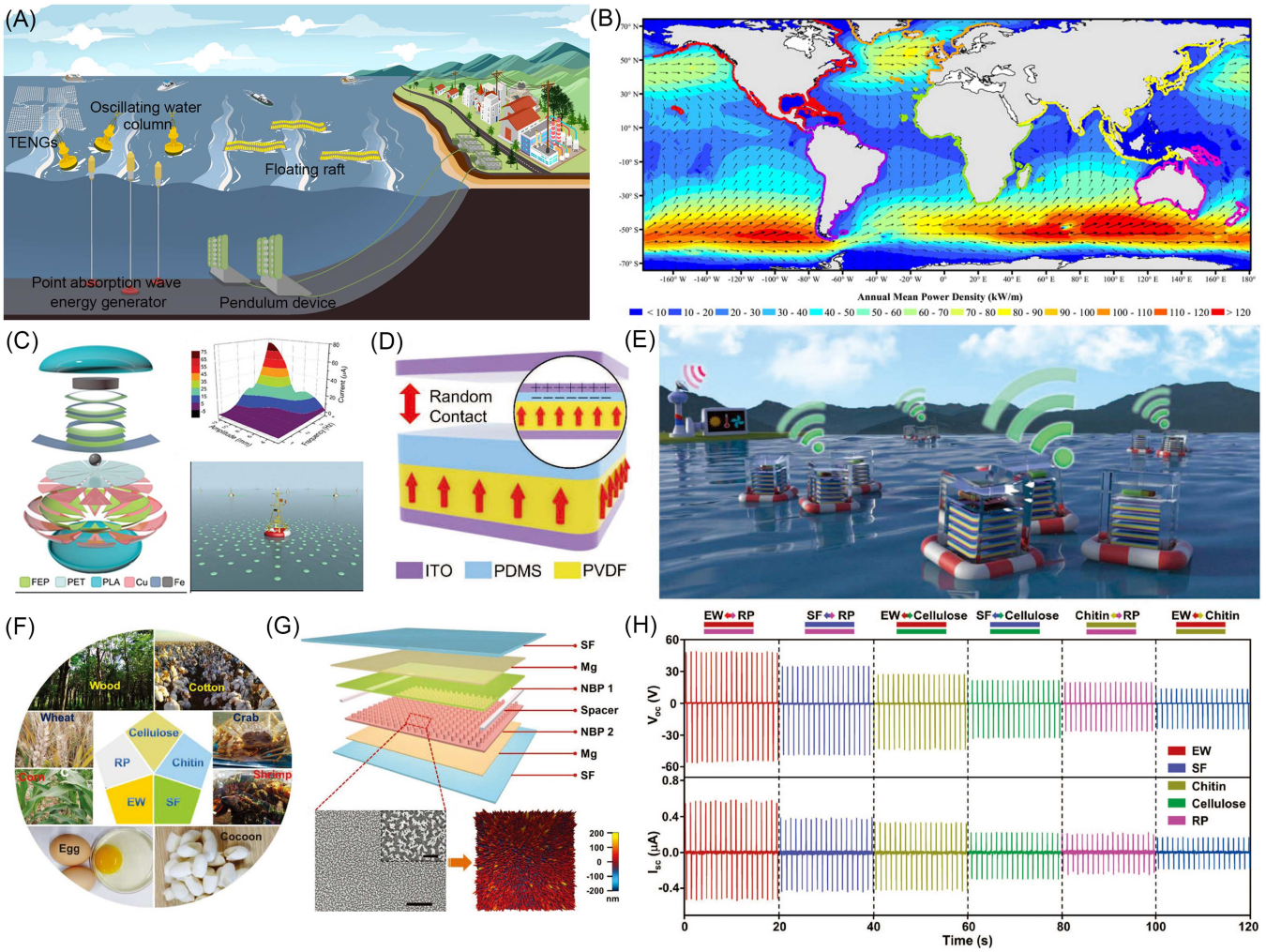

FIGURE 4 | (A) Diagram of a representative wave energy power generation device. (B) Annual mean wave power density (color) and annual mean best direction (→). Reproduced with permission [42]. Copyright 2012, Elsevier. (C) Oblate spheroidal TENG for all-weather blue energy harvesting. Reproduced with permission [43]. Copyright 2019, Wiley-VCH. (D) Schematic illustrations of FE-TENG and (E) schematic illustration of self-powered FE-TENG arrays in the ocean. Reproduced with permission [44]. Copyright 2019, Wiley-VCH. (F) Natural bioresorbable polymers originating from nature with wide raw material sources, (G) diagram of the structure of a typical BN-TENG device and (H) its output performances utilizing different combinations of triboelectric pairs. Reproduced with permission [45]. Copyright 2018, Wiley-VCH.

2.2.1 | Polymer Materials Utilized in TENGs

Polymer materials are the most widely used tribo-negative as well as tribo-positive materials in TENGs because of their excellent flexibility, plasticity, stretchability, and lightweight [51]. Owing to the strong electron absorption affinity of fluorine, polyvinylidene fluoride (PVDF), polydimethylsiloxane (PDMS), PTFE, polyethylene terephthalate (PET), and fluorinated ethylene propylene (FEP) are ideal polymeric tribo-negative materials. Conversely, polypyrrole (PPy), nylon, polyethylene oxide, cellulose, and melamine formaldehyde resin possessing electron-donating properties are commonly used as tribo-positive polymers in TENGs.

The tribo-negative polymer PTFE paired with tribo-positive metals has received great interest, as is exemplified by the ultra-high energy conversion efficiency, swing-structured TENGs developed by Jiang et al. for low-frequency marine wave energy collection [52]. The inner wall of this TENG contains six Cu electrodes and four groups of PTFE thin strips. The maximum peak power and average power of Jiang's TENG are 4.56 and 0.48 mW, respectively. Li et al. fabricated a liquid-solid-contact TENG that has enhanced friction and excellent energy output [53]. This buoy-like TENG converts ambient wave energy into electricity by using PTFE films and Ag electrodes. The wave-induced up-down movement, the TENG network possessing 18 PTFE films generates a current of 290 μA, 16725 nC transferred charges and a 300 V output voltage. The related polymer FEP has a completely fluorinated structure that gives it a strong electron-accepting ability. As a result, FEP is often used as a tribo-negative material in triboelectric pairs. By using FEP, Liu et al. developed an all-weather oblate spheroidal TENG (OS-TENGs) that collects wave energy in both rough and tranquil waters. The arched triboelectric units in the device contain an FEP film as the upper part and a lower part comprised of two Cu-coated FEP or PET polymer films and iron shot (Figure 4C) [43]. The upper part of the OS-TENGs has a maximum output voltage of 281 V and a short-circuit current of 76 μA.

It is worth noting that polymers having relatively weak electron-withdrawing abilities can not only serve as tribo-negative materials but also as tribo-positive materials. Zheng

2767441x, 2026, 3, Downloaded from https://onlinelibrary.wiley.com/doi/10.1002/idm2.70047 by Battelle Memorial Institute Pacific Northwest Division, Wiley Online Library on [22/06/2026]. See the Terms and Conditions (https://onlinelibrary.wiley.com/terms-and-conditions) on Wiley Online Library for rules of use; OA articles are governed by the applicable Creative Commons License

et al. were the first to explore a device of this type in which porous chitosan aerogel film and porous polyimide aerogel film serve as tribo-positive and tribo-negative materials, respectively [54]. The TENG, designed based on this consideration, exhibits a high voltage output of 60.6 V and current of 7.7 μA owing to the increased porosity and surface area of the polymer aerogel. A tribo-positive polymer-based TENG designed by Xu et al. contains a nylon film and PTFE balls as triboelectric materials [55]. Yao and co-workers fabricated a TENG device possessing cellulose nanofiber film paired with FEP film [56]. Other TENGs that utilize two polymeric triboelectric materials include one developed by Wang et al. that employs a micro/nanostructured PPy film as tribo-positive materials [57], and another by Kwak et al. that couples melamine formaldehyde resin with PTFE film [58]. Critical factors that need to be considered in creating a TENG that has an optimal operating efficiency are selection and modification of polymer materials that maximize surface charge density. Therefore, material surface modification protocols, such as those that modify surface morphology and add surface functionalization at the molecular level, need to be developed. Moreover, efforts devoted to the development of new polymer materials and the mechanism for the triboelectric effect should receive accelerated study.

2.2.2 | *Ferroelectric Materials Used in TENGs*

Ferroelectric materials are a class of substances that maintain permanent polarization after being removed from an electric field, a property that is known as the ferroelectric effect [59]. TENGs assembled using ferroelectric materials have the advantages of high power output, excellent sensitivity, and superior reliability [60, 61]. Barium titanate ($BaTiO_3$), the first hydrogen-lacking oxide ferroelectric material discovered, has been thoroughly investigated and widely used [62]. $BaTiO_3$ has a high charge-attracting ability due to its high dielectric constant. Seung et al. described a TENG containing a triboelectric active nanocomposite composed of a highly dielectric ceramic material ($BaTiO_3$) and a ferroelectric copolymer matrix (poly(vinylidene fluoride-co-trifluoroethylene), P(VDF-TrFE)) [63]. This nanocomposite-based TENG has a high-power generation performance associated with a 1130 V output voltage and 1.5 mA output current.

The service lifetimes of TENGs on the sea surface is an important consideration because repeated wave fluctuations lead to deformation of the component triboelectric materials and consequent gradual degradation of the performances of the TENGs. To solve this problem, Park et al. developed a multilayer composite of alternating P(VDF-TrFE) and $BaTiO_3$ nanoparticles for use in a high-performance triboelectric device [64]. The alternating soft/hard layer creates friction, which leads to an increase in the stress concentration, along with stress-induced polarization and interfacial polarization. A triboelectric device containing the multilayered nanoparticle composites exhibits a high-pressure sensitivity of 0.94 V/kPa and a 29.4 $\mu W/cm^2$ output power density. Importantly, it maintains high reversibility during 10 000-cycle tests at a current density.

In addition, using ferroelectric materials to assemble contactless mode TENGs is an effective approach to improve functional lifetimes. Kim and co-workers developed a contactless ferroelectric polymer-based TENG (FE-TENG), comprised of indium tin oxide electrodes and a PDMS elastomer (Figure 4D,E), which has a high output over fewer contact cycles, a property that increases the functional lifetime of the device [44]. Specifically, the optimized FE-TENG powers the function of a wireless temperature sensor network by collecting irregular and random water wave mechanical vibration.

2.2.3 | *Natural Materials Used in TENGs*

Because of their low costs, environmental friendliness, and sustainability, natural materials are frequently used to fabricate TENGs. Materials employed for this purpose include wood- and cotton-derived cellulose, chitin extracted from crab and shrimp shells, and plant and animal proteins. In one example, Jiang et al. fabricated bioabsorbable natural-materials-based TENGs (BN-TENGs) that contain cellulose, chitin, silk fibroin, rice paper, and egg white (Figure 4F–H) [45]. The electron gain and loss abilities of these materials are ranked from positive to negative in the following order: egg white > silk fibroin > chitin > cellulose > rice paper. The surfaces of these five materials were subjected to inductively coupled plasma-reactive ion etching to form nanostructured arrays to expand their contact areas and enhance the corresponding contact electricity. Pairs of the etched materials were used as friction layers in TENGs. The optimized BN-TENG generated in this manner exhibits 55 V output voltage, 0.6 μA current and 21.6 mW/m^2 power density. In addition, Jie et al. developed a high-output voltage and current TENG using a natural leaf design [65]. In a later effort, Feng et al. modified a powder, derived from dried plant leaves, with poly-*L*-lysine to generate material for a high-performance TENG [66]. Similarly, Chen et al. constructed a contact separation mode TENG using dried rose petals and polymethyl methacrylate [67].

Proteins and cellulose are natural materials that are also commonly used as components of TENGs. An et al. developed a TENG that incorporates soy protein and lignin blend biopolymer nanofibers as triboelectric materials [68]. The solution-blown biopolymer nanofibers are porous and fluffy, and as a result they produce a high voltage output. The electricity-generating properties of TENGs can be significantly enhanced by using chemically modified cellulose. For example, Roy et al. grafted allicin onto surfaces of cellulose nanofibers using the "thiol-ene" click method [69]. Studies showed that the electron-donating ability and surface roughness of the modified films are greater than those of cellulose fibers. The enhancement enables the TENG created by coupling of this material with a tribo-negative PVDF layer to have an excellent voltage and current output. Transparent and flexible bacterial cellulose has been used by Kim et al. for assembly of a TENG [70]. A determination of the contact angle and surface potential of the modified cellulose showed that the electrical output is directly related to curvature and friction area. Finally, Chandrasekhar et al. fabricated a TENG system by coupling a cellulose/PDMS composite film with Al [71]. A TENG containing 5 wt% of the cellulose-containing film displays an output voltage of 28 V and a circuit current of 2.8 μA.

2.3 | Materials for Ocean Current Energy Systems

In addition to the surface waves, ocean currents at various temporal and spatial scales are also important renewable

2767441x, 2026, 3, Downloaded from https://onlinelibrary.wiley.com/doi/10.1002/idm2.70047 by Battelle Memorial Institute Pacific Northwest Division, Wiley Online Library on [22/06/2026]. See the Terms and Conditions (https://onlinelibrary.wiley.com/terms-and-conditions) on Wiley Online Library for rules of use; OA articles are governed by the applicable Creative Commons License

marine energy resources. Ocean currents as energy sources have several advantageous features including long-term regularity, predictability and stability, as well as a high energy density. Generally, ocean currents, arising from difference between the wind strength and water density, have velocities greater than 2 m/s [15]. The total power of currents in the world's oceans is about 5 TW, which is one of the largest among all marine energy sources. The fundamental principles used to design systems for ocean current power generation are the same as those used for tidal kinetic energy power generation described above, except that creation of the former devices must account for the fact that they will be utilized in deep seawater. The main factors that govern the economic feasibility of ocean current energy generation at a certain location include power density at the site (Figure 5A,B), distance between the site and coast, and the local seabed depth [15, 72].

Compared with materials utilized in tidal energy conversion systems, those required for ocean current energy generation need to have even greater corrosion and fouling properties, as well as the ability to prevent water intrusion. Like tidal turbines, those that are driven by underwater currents need to capture kinetic energy associated with moving water and transfer it to rotor blades to produce electricity. As a result, neither the structural design nor materials selected to create a current driven turbine can be the same as those used for tidal turbines. To overcome stress corrosion cracking, Matarru et al. utilized Al–10Si–5Mg alloy as the material for ocean current turbine (OCT) blades owing to its toughness and strength [73]. The results of studies showed that upon being submerged and exposed to different stresses, the blades did not break even after signs of cracking and corrosion were detected. To produce a full-scale underwater OCT, design and size changes need to be implemented, but specific strength and stiffness will be key factors guiding material selection.

Another noteworthy requirement is that underwater OCTs cannot impact the environment of fish and other marine organisms. Thus, novel patterns and shapes of OCTs need to be considered, both of which require that higher plasticity materials be employed. Therefore, composite materials with high corrosion resistance, light weight, high stability and plasticity remain preferred choices for fabrication of OCTs. Aimed at these goal, Wang et al. developed a new manufacturing method that is similar to filament winding to prepare a ducted composite OCT [74]. At the same time, a steady and incompressible three-dimensional simulation was carried out using computational fluid dynamics (CFD) to assess the distribution of ocean flow fields and hydrodynamic performances under an array of different configurations (Figure 6A–C) [75]. Similarly, Ke et al. designed a crack resistant Al alloy/nanoparticle reinforced polypropylene composite blade based on the results of a CFD numerical simulation carried out to evaluate fatigue [77]. The results indicate that the composite blade successfully withstands long cycle tensile (100 N) and torque (5.15 N m) loads following immersion pretreatment. To ensure long-term durability of these composite structures, consideration should not only be given to static strength but also on fatigue resistance and the potential for stress corrosion cracking under the combined action of hydrodynamic loads and seawater exposure.

Ocean current power generation systems often operate in the high-pressure environment of the seabed, which means that sealing systems with low friction torque are crucial to prevent entrance of seawater. Nakanishi et al. showed that a polyvinyl formal (PVF) sealing lip has an excellent seawater leakage prevention ability and low friction torque [78]. To avoid deformation of the PVF seal ring under high-pressure seawater conditions, this group developed a rotating system containing a rotatable PVF seal ring on a shaft and a fixed ceramic seal ring on machine body (Figure 6D–F) [76]. In this system, the PVF and ceramic rings are pressed together to prevent seawater leakage. Wang et al. described an underwater flag-like TENG that can be driven by ocean currents [79]. In this device, the TENG contains conductive ink-coated PET and PTFE films, and PTFE tape is a sealant that separates the triboelectric layer from seawater.

Ocean current energy conversion systems need to be made of robust materials because it is difficult to address malfunctions that arise. In addition, the impact of noise generated during device operation on marine organisms needs to be considered. Although at the current time, ocean current power generation are only at the experimental research stage and many difficulties need to be addressed to enable practical applications, the pace of studies of these systems should be accelerated.

2.4 | Materials for Ocean Thermal Energy Systems

More than 70% of the earth's oceans absorb solar energy equivalent to that derived from 250 billion barrels of oil [20]. Because of the effect of solar radiation, the surface

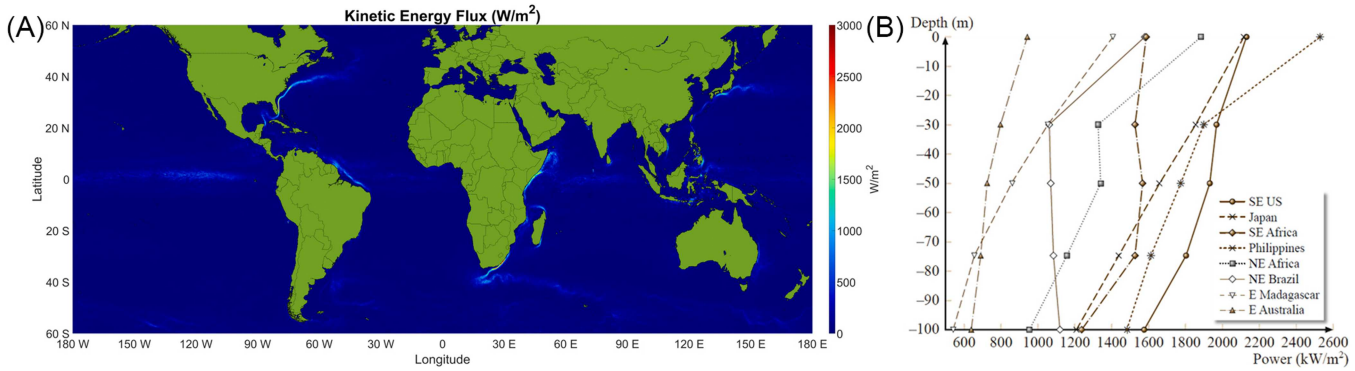

FIGURE 5 | (A) Global average power density calculated using drifter data in W/m^2. Reproduced with permission [72]. Copyright 2025, Elsevier. (B) Time average maximum power density in each region as a function of ocean depth. Reproduced with permission [15]. Copyright 2016, Springer Nature.

2767441x, 2026, 3, Downloaded from https://onlinelibrary.wiley.com/doi/10.1002/idm2.70047 by Battelle Memorial Institute Pacific Northwest Division, Wiley Online Library on [22/06/2026]. See the Terms and Conditions (https://onlinelibrary.wiley.com/terms-and-conditions) on Wiley Online Library for rules of use; OA articles are governed by the applicable Creative Commons License

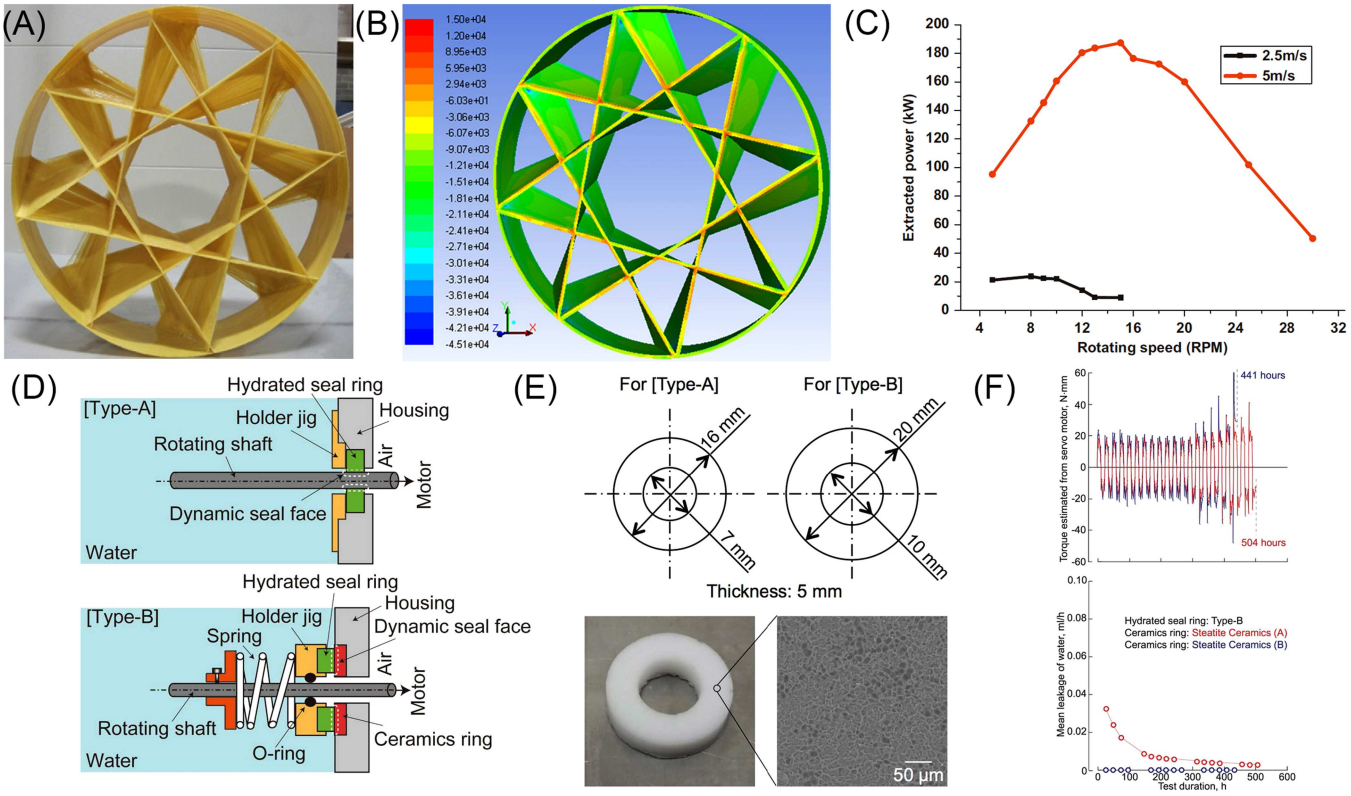

FIGURE 6 | (A) Prototypes of composite material wheels. (B) Absolute pressure distribution on a Material Marine Current Turbines (CMNMCT). (C) Extracted power variation with inlet flow velocity and rotation speed. Reproduced with permission [75]. Copyright 2012, Elsevier. (D) Schematic illustrations of shaft seals with the hydrated PVF seal rings. (E) Dimensions and images of hydrated seal rings. (F) Frictional torque and water leakage in hydrated seal rings (Type B). Reproduced with permission [76]. Copyright 2019, The Japan Society of Mechanical Engineers.

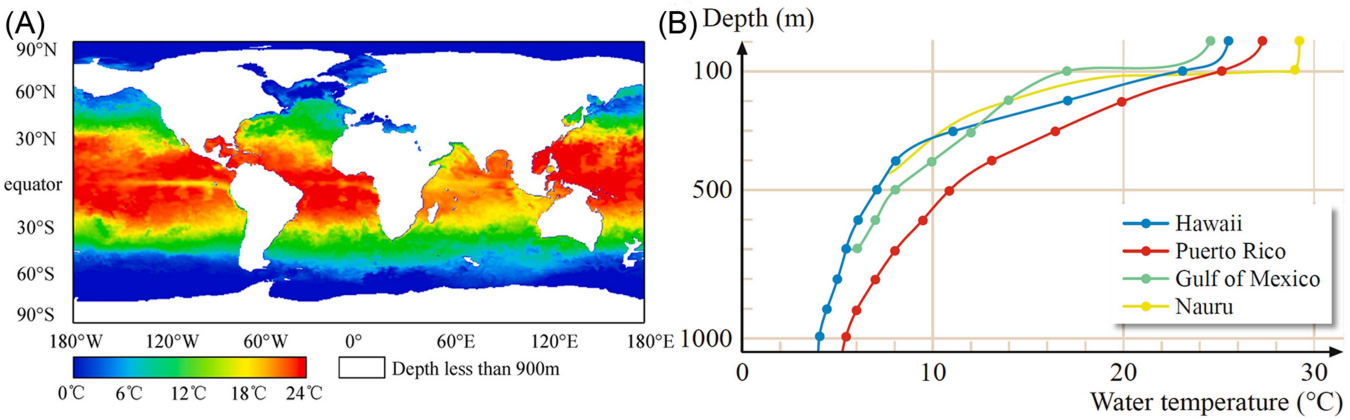

FIGURE 7 | (A) Global ocean thermal gradient. Reproduced with permission [81]. Copyright 2023, Elsevier. (B) Vertical temperature distributions at four different locations. Reproduced with permission [15]. Copyright 2016, Springer Nature.

temperature (25°C–28°C) of seawater differs greatly that at a depth of 500–1000 m (4°C–7°C). Thermoelectric power generation technologies have been developed that use the seawater temperature gradient to operate electricity producing heat engines. Differing from systems that depend on ocean waves and tides, those that are based on thermal energy conversion continuously generate considerable amounts of energy when the temperature difference between warm surface and cold deep water is about 20°C [16]. Although the annual power generated using ocean thermal energy conversion is about 30 TW [80], thermal energy gradients required to drive systems of this type are only in the equatorial regions between 20° N and 20° S spanning the Pacific, Atlantic and Indian oceans except for the west coast of South America. The distributions of differences between surface and 1000 m deep seawater temperatures on a global scale are shown in Figure 7 [15, 81].

Ocean thermal energy converters (OTECs) and ocean thermoelectric generators (OTEGs) are core components of ocean thermal energy systems. The OTEC system contains two heat exchangers comprised of an evaporator and condenser, a seawater pump, and a steam turbine (Figure 8A,B) [82, 83].

2767441x, 2026, 3, Downloaded from https://onlinelibrary.wiley.com/doi/10.1002/idm2.70047 by Battelle Memorial Institute Pacific Northwest Division, Wiley Online Library on [22/06/2026]. See the Terms and Conditions (https://onlinelibrary.wiley.com/terms-and-conditions) on Wiley Online Library for rules of use; OA articles are governed by the applicable Creative Commons License

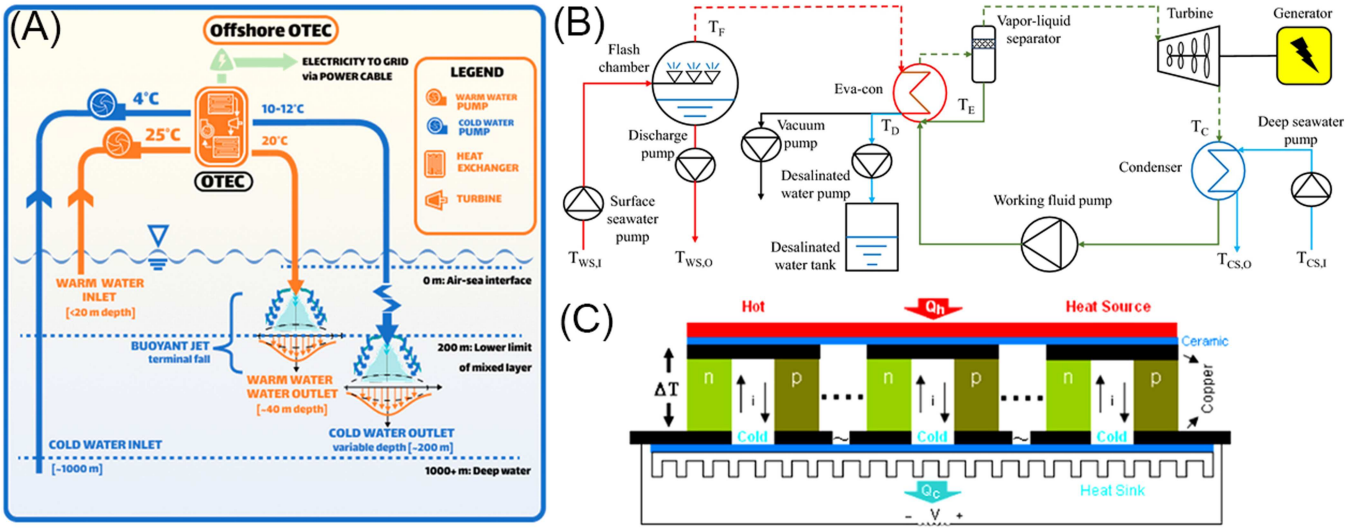

FIGURE 8 | (A) Offshore OTEC plant. Reproduced under terms of the CC-BY license [82]. Copyright 2026, The Authors, published by MDPI. (B) Diagram of the hybrid cycle OTEC system. Reproduced under terms of the CC-BY license [83]. Copyright 2024, The Authors, published by Springer Nature. (C) A model of cascaded OTEG units thermally in parallel and electrically in series. Reproduced with permission [20]. Copyright 2017, Elsevier.

Typically, the OTEC system uses a low boiling point substances such as ammonia as the working fluid to drive steam turbines for power generation [84]. Materials for use in the OTEC heat exchanger must combine corrosion resistance to ocean environments and compatibility with the working fluid. The principle of operation of a typical OTEG is based on the Seebeck effect caused by charge carrier diffusion and phonon dragging that take place in n-type and p-type semiconductor materials (Figure 8C) [20]. A temperature difference leads to a higher e^- density in the n-type material and a higher hole density in the p-type material. The efficiency of thermoelectric materials is determined by the thermoelectric figure of merit ($ZT = \sigma S^2 T/\kappa$, σ and κ are electrical and thermal conductivity, respectively; and S is the Seebeck coefficient) [85]. The OTEG efficiency can be improved by maximizing the S and reducing the resistivity and κ.

2.4.1 | *Materials for OTEC Systems*

This subsection focuses on metallic and alloy materials used in OTEC components such as heat exchangers, turbines, and pipelines, where corrosion resistance, thermal conductivity, and structural integrity in seawater are critical.

Based on the above considerations, a variety of materials including Al, Ti and stainless steel have been utilized in OTECs [86]. Because Al has high thermal conductivity, low density and good ductility, it can be safely employed when any working fluid is used [87]. Due to the presence of an oxidized protective layer on its surface, Al is inert at seawater velocities of less than 2.2 m/s. These factors led Cavrot to suggest that Al is a cost-effective and efficient heat exchanger material [88]. It is worth mentioning that Cu-Ni alloy also has corrosion resistance under a high seawater flow rate (< 4.5 m/s), and Cu-Ni-Fe alloy (90/10/1.5) resists biologically promoted destruction. Moreover, stainless steel has good machinability and weldability. However, high chromium content stainless steel alloys need to be used in the marine environments [89]. In addition, because stainless steel with molybdenum, such as 326, has excellent corrosion resistance at low seawater speeds [90], an impeller comprised of 3% molybdenum has been successfully used in an OTEC system. OTEC turbine blades are typically fabricated using 17-4 PH stainless steel, which combines greater lateral ductility and fracture toughness [91, 92]. Besides, suitable materials such as high-density polyethylene and fiber reinforced plastics are employed to construct large diameter, compression and corrosion resistant pipelines for transport low-temperature deep seawater to the platform of an OTEC system. Because the lengths of pipes used in OTEC systems are about 1–5 km, the economics and service lifetimes of materials are also important considerations.

2.4.2 | *Material for OTEG Systems*

In general, thermoelectric materials need to enable charge carriers to have optimized mobilities, concentrations and effective masses. Thus, the microstructures, densifications and sizes of materials affect their thermoelectric properties. The performances of thermoelectric materials are also significantly improved by doping, nanostructuring and compositing [93]. Here, the focus shifts to semiconductor, polymer, and nanostructured thermoelectric materials for OTEGs.

Traditional inorganic materials such as metal oxides and chalcogenides, silicon, silicon-germanium alloys, silicides and skutterudites have excellent thermoelectric properties. Although inorganic materials are widely applied in OTEG, their mechanical properties are barely satisfying due to the existence of strong ionic or covalent bonds in the crystal structure. Metal chalcogenides are ideal thermoelectric materials because of their smaller band gaps. Goldsmid first published research on the thermoelectric properties of Bi_2Te_3, and then p-type $Bi_{2-x}Sb_xTe_3$ and n-type $Bi_2Te_{3-x}Se_x$ became the preferred thermoelectric materials [94–96]. The development of the microelectronic industry and the economy of silicon have promoted the thermoelectric application of Si and SiGe alloys. Geballe and

2767441x, 2026, 3, Downloaded from https://onlinelibrary.wiley.com/doi/10.1002/idm2.70047 by Battelle Memorial Institute Pacific Northwest Division, Wiley Online Library on [22/06/2026]. See the Terms and Conditions (https://onlinelibrary.wiley.com/terms-and-conditions) on Wiley Online Library for rules of use; OA articles are governed by the applicable Creative Commons License

Hull have conducted in-depth research on the thermoelectric properties of single crystal silicon [97]. Dismukes et al. first studied and measured the maximum *ZT* values of n-type and p-type $Si_{0.70}Ge_{0.30}$ alloys as ≅1 and 0.7 [98]. Zhu et al. analyzed the effect of nanostructures and point defects in SiGe alloys on thermoelectric properties, and found that nanoparticles in $Si_{95}Ge_5$ resulted in a twofold decrease in thermal conductivity compared with bulk samples (Figure 9A–C) [99]. The thermoelectric properties of metal oxides are lower than those of traditional thermoelectric materials, and their carrier mobility is 2–3 orders of magnitude lower than that of chalcogenide homologs [103]. Typical p-type and n-type metal oxides include $Na_xCo_2O_4$, $Ca_3Co_4O_9$, Sr_2TiO_4, BiCuSeO, $CaMnO_3$, and ZnO (Figure 9D) [100, 104–111]. The efficiency of oxide-based thermoelectric generators may be 10%–15%. Beyond that, skutterudites, zintl phases, clathrates and heusler compound are also commonly used thermoelectric materials [112–114].

Recently emerging conductive polymers and carbon nanomaterials, such as polyaniline (PANI), poly-(3,4-ethylenedioxythiophene) (PEDOT), polypyrrole and graphene, possess excellent thermoelectric properties and processability. Because the polymers themselves have low carrier concentrations and poor electrical conductivities, materials which contain additional charge carriers introduced by doping are useful for OTEG applications. The main disadvantage of utilizing PEDOT in OTEG systems is its low electronic conductivity [90, 115]. For example, Seebeck coefficients of PEDOT's containing p-type dopants are ~100 μV/K and those containing n-type dopants are ~140 μV/K. Also, addition of polystyrene sulfonate (PSS) to PEDOT effectively improves electronic conductivity and thus thermoelectric performance. Zhang et al. showed that a PEDOT:PSS membrane, prepared by using a simple cosolvent and/or salt cosolvent solution post-treatment method, has significantly improved the thermoelectric properties [116]. The conductivity and power factor of the PEDOT:PSS membrane are

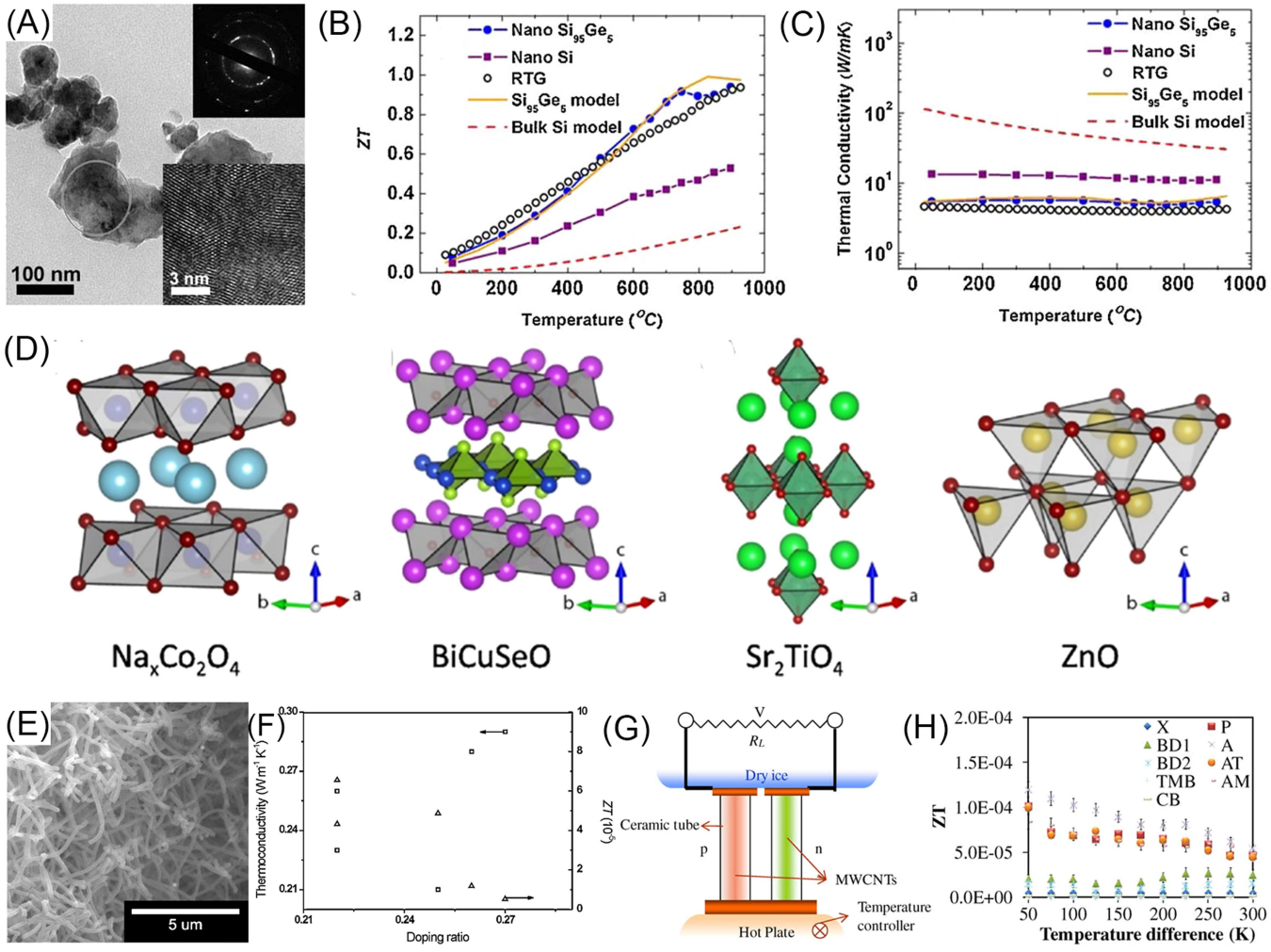

FIGURE 9 | (A) Transmission electron microscope (TEM) image of ball milled $Si_{95}Ge_5$ nanopowders, the insets are the diffraction pattern and high resolution transmission electron microscope (HRTEM) image for the circled region. (B) Temperature-dependent *ZT* and (C) thermal conductivity of nanostructured Si, nanostructured $Si_{95}Ge_5$, bulk Si model, and bulk $Si_{80}Ge_{20}$ alloy (RTG) samples. Reproduced with permission [99]. Copyright 2009, American Physical Society. (D) Crystal structures of the main metal oxides discussed in this section. Reproduced with permission [100]. Copyright 2019, Elsevier. (E) SEM image of PANI-NSA nanotubes (NTs). (F) Thermal conductivities (□) and *ZT* value (△) of PANI NTs as a function of the doping ratio. Reproduced with permission [101]. Copyright 2010, Elsevier. (G) Thermoelectric (TE) cell with p-type and n-type TE elements electrically connected across hot ends and connected to a multimeter at the cold end. (H) Diagram of merit *ZT* (non-dimensional) of TE device for as-produced, B-doped, and N-doped multi-walled CNTs, and carbon black (CB). Reproduced with permission [102]. Copyright 2009, Elsevier.

2767441x, 2026, 3, Downloaded from https://onlinelibrary.wiley.com/doi/10.1002/idm2.70047 by Battelle Memorial Institute Pacific Northwest Division, Wiley Online Library on [22/06/2026]. See the Terms and Conditions (https://onlinelibrary.wiley.com/terms-and-conditions) on Wiley Online Library for rules of use; OA articles are governed by the applicable Creative Commons License

1831 S/cm and 144 μW/m respectively. As depicted in Figure 9E,F, Sun et al. demonstrated that doping PANI nanotubes with β-naphthalene sulfonic acid (β-NSA) increases the electrical conductivity from 0.0045 to 0.0077 S/cm, and decreases the thermal conductivity by 27.5% [101]. In addition to doping, organic polymers can also be combined with other materials to produce high performance flexible functioning OTEGs [117].

Although carbon nanomaterials, such as CNTs and graphene, have high electrical conductivities, it is a challenge to control their thermal conductivity. Fujii et al. devised a novel method to detect the thermal conductivity of a single CNTs, and employed it to show that the thermal conductivity of multi-walled CNTs decreases with increases in their diameter [118]. Kunadian et al. prepared B- and N-doped multi-walled CNTs, and demonstrated that doping not only reduces thermal conductivity but also increases the Seebeck coefficient (Figure 9G,H) [102]. Similarly, graphene has extremely high thermal conductivity and, as a result, it is not itself an ideal thermoelectric material. Studies have shown that graphene nanoribbons with disordered edge structures or graphene quantum dots have improved thermoelectric properties [119]. In addition, the introduction of weak coupling interface also reduces thermal conductivity [120, 121]. Although carbon nanomaterials themselves have poor thermoelectric performances, their combination with high-performance thermoelectric materials makes them suitable for OTEG applications.

The high *ZT* values and power factors given in this section, which are primarily measured under controlled laboratory conditions, demonstrate the significant intrinsic potential of these thermoelectric materials. However, their effective performance in real OTEC/OTEG systems will be critically dependent on long-term stability against seawater corrosion, thermal cycling fatigue, and fouling on heat exchanger surfaces.

2.5 | Materials for Salinity Gradient Energy Systems

Ocean salinity gradient energy refers to the chemical potential energy difference between seawater and freshwater present at junctions of oceans and estuaries or between two seawater areas having different salt concentrations. Salinity gradient energy conversion (SGEC) can be used for osmotic pressure, steam pressure and mechanical-chemical types of power generation [122]. According to estimates, the salinity gradient energy in various regions of the world is about 30 TW, 2.6 TW of which is readily available [123]. At present, the most common and promising SGEC processes include membrane-based pressure retarded osmosis (PRO) and reverse electrodialysis (RED) [124, 125]. In the PRO process, an asymmetric porous membrane is placed between solutions with different salinities. The osmotic pressure difference between the solutions drives water flow from the low to high concentration side, creating an increase in the volume at the high concentration side that drives a turbine to generate electricity. In contrast, in RED devices contain an ion selective permeation membrane between solutions having a salinity difference. The concentration difference causes directed migration of the salt with consequent redox-based conversion of chemical potential energy into electrical energy. Compared with PRO, RED is more suitable for power generation at locations where a low salinity difference exists (eg., river estuary) owing to advantages associated with high energy density, low membrane pollution and low cost (Figure 10).

In RED systems, an electrochemical process takes place to convert ionic flux directly into current. In order to improve the conversion efficiency of SGECs, it is important to utilize ion exchange membranes that have highly selective permeabilities and high ionic conductivities [127, 128]. In recent years, the development of novel polymer-based materials has greatly improved the function of ion exchange membranes leading to increases in the output power of SGECs [129, 130]. Inspired by euryhaline-fish which readily adapt to high salinities, Hao et al. designed a sulfonated poly(ether ether ketone)/anodic aluminum oxide (AAO)/PPy nanochannel system that has salinity adaptability [131]. The rich surface charges and narrow pores in membranes comprised of this material enable the density for osmotic power generation of this device to reach 26.22 W/m^2. Also, as illustrated in Figure 11A–C, Li et al. constructed a device consisting of a mushroom shaped nanochannel array membrane having an ultra-thin selective layer, that has a power density of 22.4 W/m^2 under a 500 times salinity gradient. The stem of the mushroom nanochannel is created by self-assembly of a block copolymer and the cap is formed using monomolecular hyperbranched polyethylenimine. The enhanced power output of this system is mainly due to unidirectional transport in ion channels and excellent ion selectivity [132].

Thus far, attaining a balance between the permeability and ionic conductivity of an ion exchange membrane remains challenging. Recently, Li et al. employed self-assembly of block copolymers to produce a membrane that has a small ion exchange capacity. The membrane produces an ultra-high power density of 19.3 W/m^2 at a salt concentration ratio of 50 [135]. Studies by this group showed that high density helical porphyrin channels in the membrane possess high Cl^- selectivity and good conductivity, which contributes to efficient SGEC performance. Materials with nanofluid channels are often fragile and difficult to process in fabrication of SGECs. To overcome these problems, Zhang et al. prepared covalently bonded organic polymer films by using the sol-gel method and demonstrated that the films have excellent mechanical properties and stability, and a system in which they are employed as a membrane has a maximum output power density of 6.21 W/m^2 (Figure 11D–F) [133]. In addition, among materials that control transport of nanofluids, polymer/MOF hybrid membranes have become the focus of SGEC related studies owing to a combination of the advantageous features including well-developed pores and polymer rich functional groups. Li et al. prepared a PSS/MOF composite for use as an asymmetric hybrid nanochannel membrane in conjunction with a anode of aluminum oxide (AAO) [136]. The cationic selectivity of the new membrane containing an optimized PSS content has a power density of 2.87 W/m^2.

In addition to regulation of the ion exchange and selectivity and permeability of membranes, fouling is a particularly important problem to solve in generating ocean SGEC systems. In these devices, membrane fouling leads to a sharp decline in permeability and an increase in ion transport resistance. Therefore, materials with inherent antifouling properties, such as graphene and MXene that have antibacterial activities, have been developed for use as nanofluidic membranes. Studies have shown that the antibiotic properties of these materials

2767441x, 2026, 3, Downloaded from https://onlinelibrary.wiley.com/doi/10.1002/idm2.70047 by Battelle Memorial Institute Pacific Northwest Division, Wiley Online Library on [22/06/2026]. See the Terms and Conditions (https://onlinelibrary.wiley.com/terms-and-conditions) on Wiley Online Library for rules of use; OA articles are governed by the applicable Creative Commons License

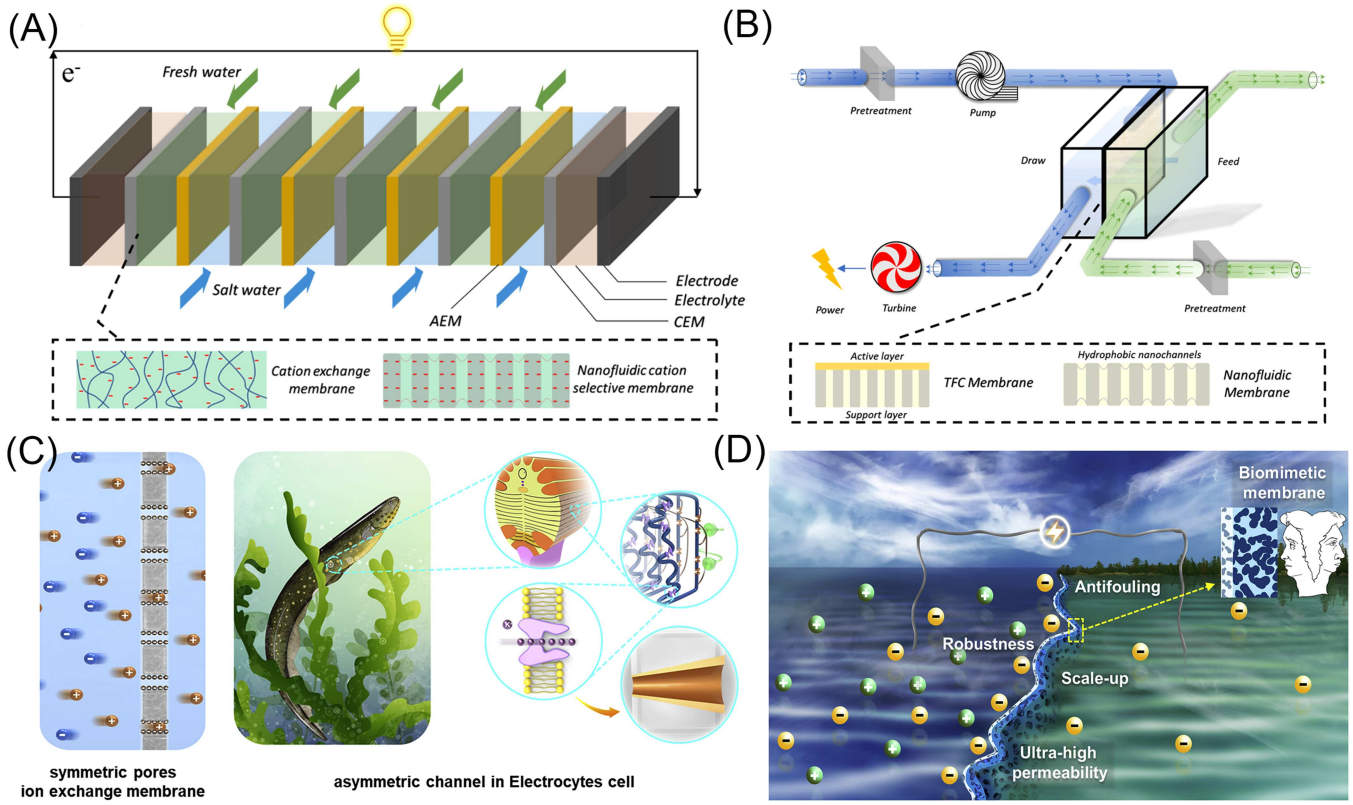

FIGURE 10 | Schematic flowcharts show the principles of (A) RED and (B) PRO. Reproduced with permission [126]. Copyright 2021, American Chemical Society. (C) Membrane science development considering the RED approach for the salinity gradient generators. (D) Challenges and perspective for future RED membrane design. Reproduced with permission [127]. Copyright 2020, Elsevier.

are mainly associated with the production of reactive oxygen species that enter cells where they destroy DNA and proteins. Hu et al. found that graphene-based carbon nanomaterials effectively inhibit propagation of *Escherichia coli* cells and show minimal cytotoxicities (Figure 11G–J) [134]. Gao et al. obtained high performance $Ti_3C_2T_x$ MXene/GO hybrid PRO membrane for use in SGECs. The hybrid membrane has excellent antifouling and antibacterial activities, which enable the system to have a high power density of about 56.4 W/m^2 [137]. These workers showed that the main reasons for the excellent antifouling performance brought about by increasing GO content of the hybrid membrane are enhancements in hydrophilicity and surface negative charges. To the best of our knowledge, only a few reports exist describing technologies for the preparation of large-scale antifouling nanofluidic membranes that can be utilized industrially in a cost effective manner [126, 138].

3 | Materials for Marine Energy Transmission

As mentioned above, marine energy is mainly used for power generation. As a result, the transmission of marine energy mainly refers to transmission of electric power. Submarine cables, wrapped in insulating materials and located on the seabed, are employed for power transmission. The electric energy generated at the marine energy production site is moved to and collected at a booster station by utilizing submarine cables, and then it is transmitted to a centralized control center on land through high-voltage submarine cables (Figure 12). Typically, the collecting-line submarine cables operate at 35 kV, while the submarine cables linked to the land can carry 110 or 220 kV, depending on the distance they span. In 1850, the world's first submarine cable was laid between Calais (France) and Dover (Britain) [139], and at the present time the total length of worldwide submarine cables is about 10^6 km [140]. The submarine location enables the cable to be free from negative natural environmental impacts such as wind, waves and the interference from human caused activities. Thus, the cables are both stable and safe, which makes them cost effective.

When the distance between the sites for generation and utilization are large (> 2000 km), the costs of electricity transmission using submarine cables are significantly high [141]. An approach that circumvents this problem involves conversion of the electricity at the site of its production into longer lived and more easily transported hydrogen gas. The hydrogen evolution reaction (HER) via seawater splitting is an attractive and sustainable hydrogen production technology, but its practical applications are limited currently by the slow nature of the process, chloride corrosion, and the high costs of noble metal-based catalysts [142]. Thus, an urgent need exists to develop highly active, low-cost and corrosion resistant catalyst materials that reduce the HER overpotential and improve the efficiency for hydrogen production.

3.1 | Materials for Submarine Cable

Submarine power cables (SPCs) for underwater transmission of high-power electricity play a key role in marine energy generating systems. Currently, nearly 8000 km of high-voltage direct

2767441x, 2026, 3, Downloaded from https://onlinelibrary.wiley.com/doi/10.1002/idm2.70047 by Battelle Memorial Institute Pacific Northwest Division, Wiley Online Library on [22/06/2026]. See the Terms and Conditions (https://onlinelibrary.wiley.com/terms-and-conditions) on Wiley Online Library for rules of use; OA articles are governed by the applicable Creative Commons License

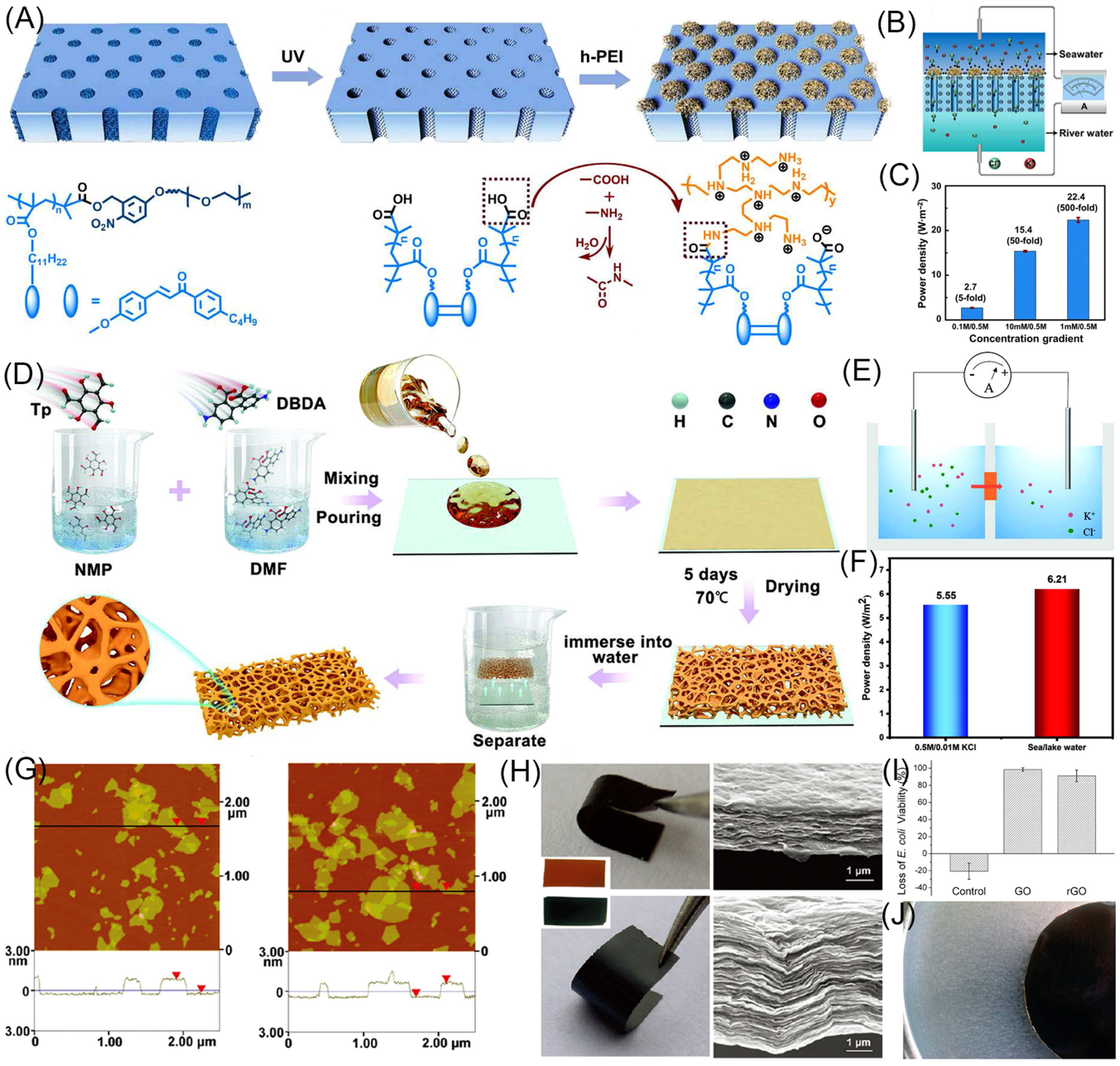

FIGURE 11 | (A) Robust h-PEI-capped nanochannel array membrane for osmotic power generator. (B) Illustration of osmotic energy conversion by the h-PEI-capped nanochannel membrane. (C) Maximum output power densities at various salt gradient concentration. Reproduced with permission [132]. Copyright 2021, American Association for the Advancement of Science. (D) Schematic diagram of the pathway for synthesis of the covalent organic polymer membrane. (E) Schematic diagram of the salinity gradient energy conversion. (F) Salinity gradient energy conversion under artificial and real gradient conditions. Reproduced with permission [133]. Copyright 2022, Wiley-VCH. (G) AFM images of GO and rGO sheets. (H) Photographs of freestanding and flexible GO (top) and rGO paper (bottom); thickness of GO (top) and rGO (bottom) paper as measured via SEM. (I, J) Antibacterial activities. Reproduced with permission [134]. Copyright 2010, American Chemical Society.

current (DC) SPCs exist in the world, of which more than 70% are located in adjacent sea areas in Europe (Figure 13) [140, 143]. Since seabed surroundings are extremely harsh environments, SPCs are required to have special properties such as waterproofed, corrosion and pressure resistant, and sustainability to uncontrollable external collisions, in addition to high electrical transmission performance and safety.

Figure 14A displays the constituents and arrangements of materials in a typical SPC [144]. The core of an SPC is composed of a Cu or Al conductor surrounded by several insulating layers. Although the current carrying capacity of Cu is better than that of Al, generally, the deep ocean section of SPCs need to be Al conductors, while the shallow ocean part (< 400 m) can be constructed using Cu. The main reason for the use of Al is to reduce the weight and limit the tension on the SPC during installation. To protect the core from corrosion, an SPC possesses three protective layers including an insulation, protective and armor layer. Examples of materials for the insulation layer in high voltage cables are ethylene propylene rubber and

2767441x, 2026, 3, Downloaded from https://onlinelibrary.wiley.com/doi/10.1002/idm2.70047 by Battelle Memorial Institute Pacific Northwest Division, Wiley Online Library on [22/06/2026]. See the Terms and Conditions (https://onlinelibrary.wiley.com/terms-and-conditions) on Wiley Online Library for rules of use; OA articles are governed by the applicable Creative Commons License

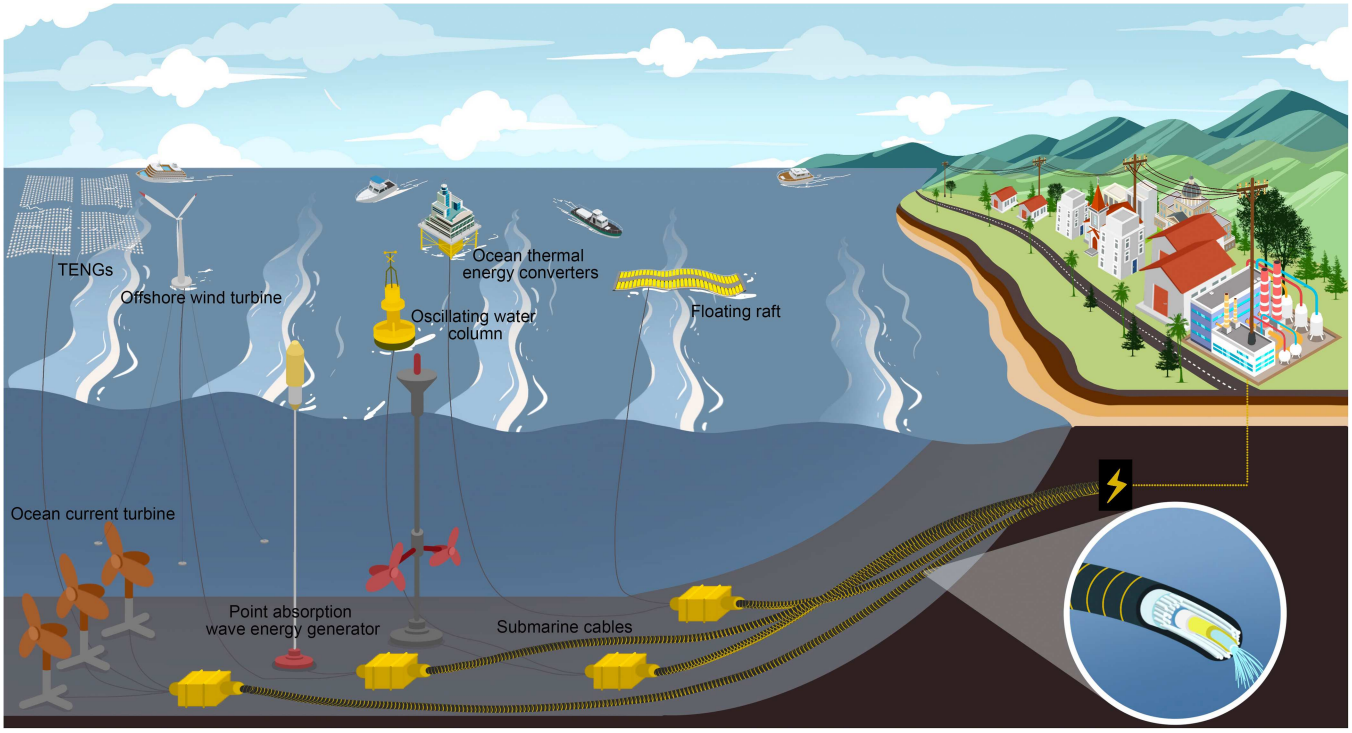

FIGURE 12 | Schematic illustration of ocean energy transmission based on submarine cables.

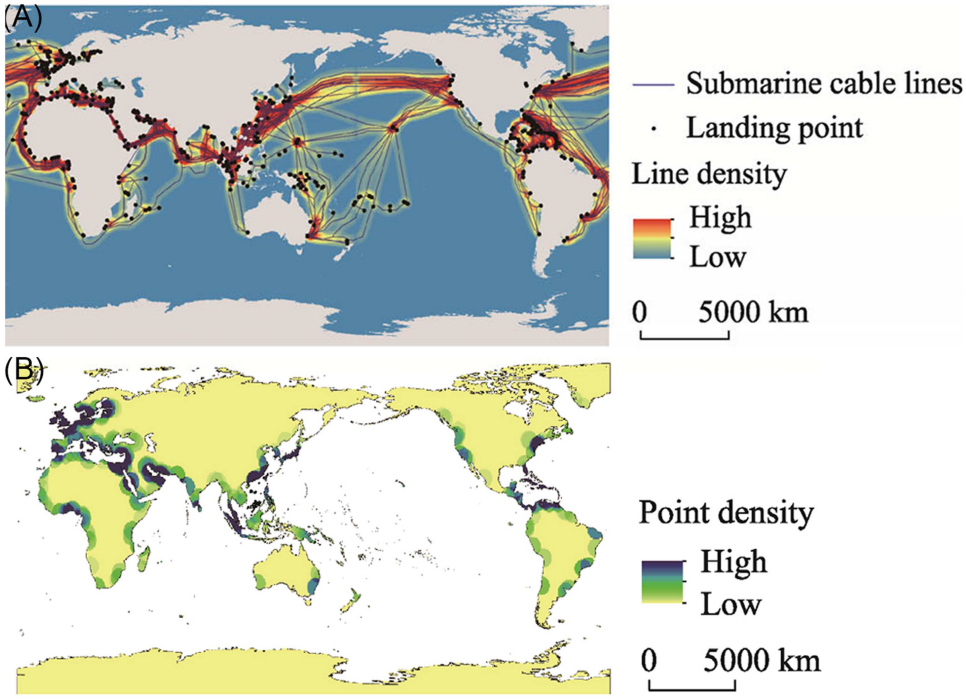

FIGURE 13 | (A) Distribution pattern of global submarine cable lines and their density and (B) the point density distribution of global submarine cable landing points in 2023. Reproduced with permission [143]. Copyright 2025, Springer Nature.

crosslinked polyethylene, which provide excellent electrical insulation, and heat/cold and aging resistance. Polyethylene (PE) is comprised of a 3D network which provides the mechanical strength needed to make it stable under high temperature and chemical corrosion conditions [146–149]. The inside and outside of SPCs also contain protective layers, with the inner sheath comprised of PE and the outer sheath being either rubber cotton tape, asphalt or a polypropylene inner cushion which together have strong seawater corrosion resistance. When an SPC is exposed to a heavy electrical load, thermal and mechanical stress arises leading to insulation degradation and fatigue of the sheath. To gain insight into the design of optimal SPC materials, modeling and simulation studies have been performed. For example, Hamdan et al. used

2767441x, 2026, 3, Downloaded from https://onlinelibrary.wiley.com/doi/10.1002/idm2.70047 by Battelle Memorial Institute Pacific Northwest Division, Wiley Online Library on [22/06/2026]. See the Terms and Conditions (https://onlinelibrary.wiley.com/terms-and-conditions) on Wiley Online Library for rules of use; OA articles are governed by the applicable Creative Commons License

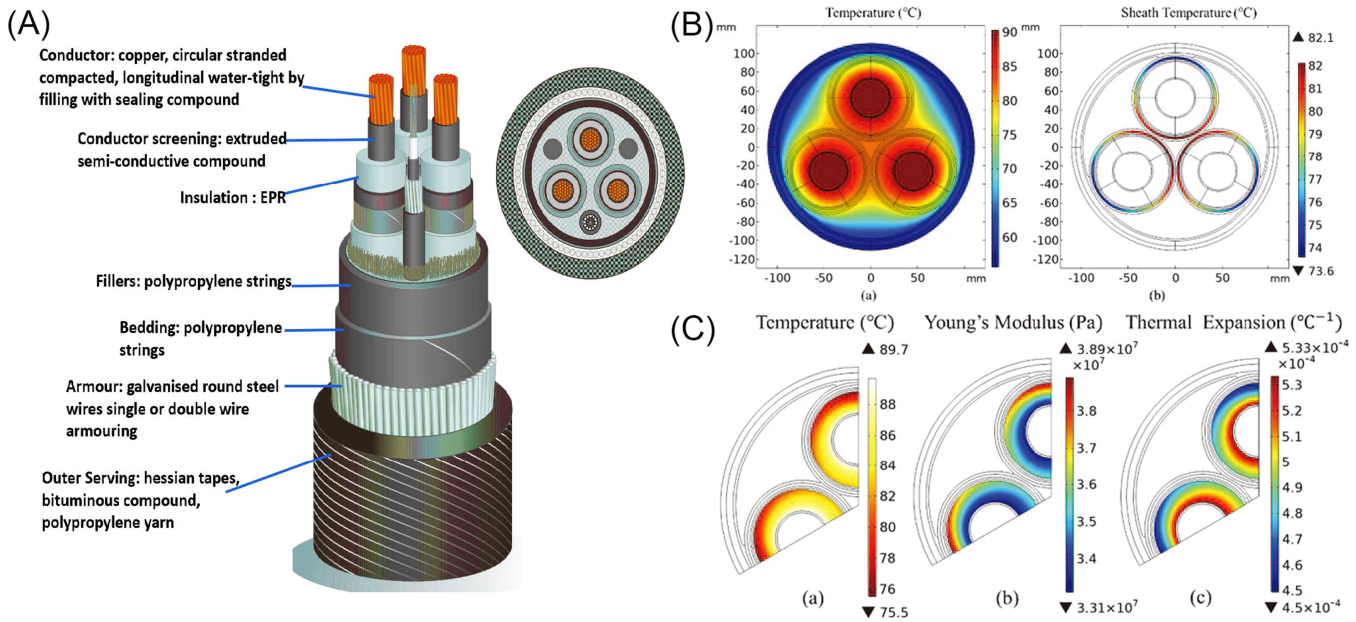

FIGURE 14 | (A) Constituents in SPCs. Reproduced with permission [144]. Copyright 2019, IEEE. (B) Temperature distribution of a three-core cable at 90°C and sheath temperature distribution. (C) Temperature, insulation elastic modulus, and insulation thermal expansion distributions at 90°C. Reproduced with permission [145]. Copyright 2020, IEEE.

the finite element method to simulate and analyze thermal mechanical stress inside a three-core SPC [145]. The results show that the thermal expansion and elastic modulus of cross linked-PE have a great influence on radial plastic deformation of the sheath (Figure 14B,C). Finally, bronze, brass, Al and/or other metals are typically twisted with a pitch in accord with the extension direction of the cable to form an armor layer to mechanically protect the SPC.

The cores of closely related submarine communication cables (SCCs) consist of high-purity and hair-thin optical fiber materials, which guide light along the path by internal reflection. It is worth mentioning that SPC and SCC need not be independent units, but components of the latter can be integrated into the former to monitor parameters such as temperature, strain and vibration, as well as to accurately detect and track faults. The optical fiber components of dual functioning cable are a core and outer coating. Core materials are required to have high purity and light transmittance to minimize power loss associated with light absorption by impurities [150]. Moreover, the refractive index requirements of the core greatly differ from those of the coating but their thermal expansion coefficients need to be similar.

Both materials and fabrication technologies are key issues that must be addressed in creating high light transmitting cables [151, 152]. Optical fibers in these cables can be divided into groups based on the types of materials used for their construction. The groups include quartz glass (QGOF), composite, silicate, fluoride, and plastic optical fibers. The high refractive index material SiO_2 is employed to produce the core of QGOF, which has a large diameter, high light transmittance and mechanical strength, and an ease for coupling to the light source. However, SiO_2 optical fiber has a strong hydroxyl related light absorption at 2 μm that causes a large optical loss. In recent years, the main components of optical fibers have been extended beyond pure SiO_2 to composites with B_2O_3, Tl_2O_3, P_2O_5, GeO_2, and Na_2O [153–155]. The important characteristics of these multi-component glasses are low softening points and large differences in refractive index between core and outer layers.

Chalcogenide glass optical fibers (CGOF) have also been widely studied due to their low transmission loss in the mid-infrared wavelength region of 2–12 μm. Mossadegh et al. prepared a single-mode CGOF composed of a $As_{40}S_{58}Se_2$ core and a $As_{40}S_{60}$ cladding by using a double-crucible technique [156]. This fiber has an optical loss that is less than 1 dB/m. Churbanov conducted a study to assess the influence of C, H and O impurities, and heterophase impurity inclusion on the optical loss of CGOFs [157]. An investigation by Davies et al., in which a combination of raw material purification and glass distillation was employed to significantly reduce the content of impurities in CGOF, led to the preparation of high-purity CGOF having an optical loss as low as 0.2–0.3 dB/m [158–160]. Moreover, composites of rare-earth dopants (Yb^{3+}, Er^{3+}, Tm^{3+}, Ce^{3+}, Tb^{3+}, Nd^{3+}, etc.) with SiO_2 has been given more attention in a search for ideal waveguide optical fibers. Dragic et al. discussed in detail the three most common rare-earth element (Yb^{3+}, Er^{3+}, and Tm^{3+}) doped glass fibers, as well as the importance of materials engineering in applications of high power fiber lasers [150].

Although glass optical fibers have been given great attention, their weak mechanical properties and lack of bendability are detrimental issues. As a result, studies have been carried out to determine if the large core diameter, simple connectability and readily bendability of plastic optical fibers (POFs) enable them to have broader utility in submarine cables (Figure 15A) [161]. The composition of POF is different from other traditionally employed materials in that their core and outer layers are composed of polymethyl methacrylate-, polystyrene-, and polycarbonate-based polymers. Koike et al. reviewed the development and current status of POFs, and highlighted

2767441x, 2026, 3, Downloaded from https://onlinelibrary.wiley.com/doi/10.1002/idm2.70047 by Battelle Memorial Institute Pacific Northwest Division, Wiley Online Library on [22/06/2026]. See the Terms and Conditions (https://onlinelibrary.wiley.com/terms-and-conditions) on Wiley Online Library for rules of use; OA articles are governed by the applicable Creative Commons License

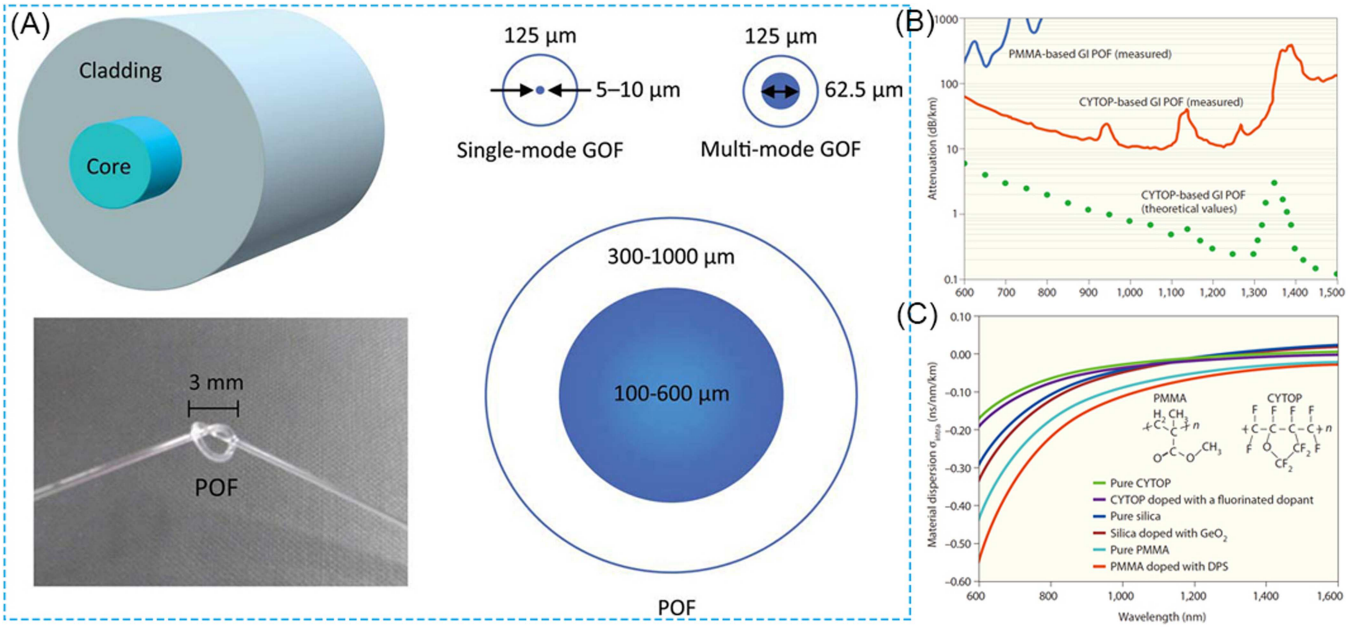

FIGURE 15 | (A) Cross-section views of representative optical fibers and an image of a POF with a 3 mm knot. (B) Comparison of attenuation spectra of PMMA and CYTOP GI POFs. (C) Comparison of material dispersion of polymer matrices of pure and doped CYTOP, silica and PMMA. Reproduced with permission [161]. Copyright 2009, Springer Nature.

the potential use of graded index POFs as materials for next-generation optical fibers [162]. Electronic transition and bond vibrations are the main reasons for the inherent light loss occurring in POFs. It was found that light attenuation can be significantly reduced by replacing H atoms in the polymer backbones with F or Cl atoms owing to a reduction of bond vibration associated light absorption. Perfluoro(1-butenyl vinyl ether) polymer (CYTOP) is a highly transparent perfluorinated material with high thermal stability and extremely low material dispersion. The plots in Figure 15B,C show that the theoretical attenuation limit of the CYTOP-based graded index POF is ca. 0.7 dB/km at 1 μm [161, 163]. Garito et al. suggested that mode coupling in a POF is the key to improving the bandwidth of an optical fiber that determines its information carrying capacity [164].

Pressure monitoring of deep-sea SPCs is critical to maintain the power transmission process. Rothmaier et al. created a pressure sensor composed of a flexible POF and tested its sensitivity [165]. Although applied in textile weaving, the preparation technology and flexible design concept developed by Rothmaier et al. serve as guides for the application of submarine cables.

3.2 | Materials for Hydrogen Production by Electrolytic Seawater Splitting

As mentioned above, marine energy can be converted into electric energy and then transmitted to a land located grid connection via submarine cables. However, the construction and material costs for transmitting electric energy from deep sea areas via submarine cables are high. Seawater splitting driven by marine energy is a sustainable and environmentally friendly method to produce hydrogen fuel [166, 167]. Thus, marine energy driven seawater splitting to produce readily transportable hydrogen would be an indirect but less expensive way to transport marine energy to land locations. At present time, one key factor for the success of hydrogen production technology by seawater splitting is the availability of low-cost and efficient electrocatalyst materials.

Under standard conditions, the Gibbs free energy change of water electrolysis is 237.2 kJ/mol, which corresponds to the theoretical equilibrium potential of 1.23 V [168]. Owing to factors including solution resistance, intrinsic conductivity and catalyst activity, the voltage required for water splitting is greater than 1.23 V [169–171]. To lower the difference between the theoretical and required voltages for promoting the HER, referred to as an overpotential, catalyst materials with high conductivity and large numbers of active sites have been developed, including noble metals, transition metal nitrides, carbides and heteroatom-doped carbon materials. As depicted in Figure 16, because of its complex components, especially Cl^- (~0.5 mol), seawater causes catalyst corrosion [172–174]. In addition, the pH near the electrode surface changes sharply during water electrolysis, Ca^{2+} and Mg^{2+} present in large amounts in seawater, precipitate on the electrode surface, blocking the active sites and reducing catalytic activity [175, 176]. Kirk and Ledas proved that the amount of adhered precipitates formed during seawater electrolysis is proportional to the salt concentration [177]. Therefore, the design and preparation of highly active HER electrocatalysts are crucial for advancing the indirect method of transporting marine energy.

3.2.1 | *Noble Metal-Based Catalysts*

As can be clearly seen by inspection of Figure 17A, noble metals (Pt, Ru, Ir, etc.) have excellent HER electrocatalytic performances and they are often benchmarks for these types of catalysts [178, 183, 184]. In particular, Pt possesses the highest HER catalytic activity recorded thus far, and loading Pt on carbon support materials with high conductivities and high specific surface areas effectively prevents aggregation and leaching of Pt nanoparticles during the HER. By utilizing the atomic layer

2767441x, 2026, 3, Downloaded from https://onlinelibrary.wiley.com/doi/10.1002/idm2.70047 by Battelle Memorial Institute Pacific Northwest Division, Wiley Online Library on [22/06/2026]. See the Terms and Conditions (https://onlinelibrary.wiley.com/terms-and-conditions) on Wiley Online Library for rules of use; OA articles are governed by the applicable Creative Commons License

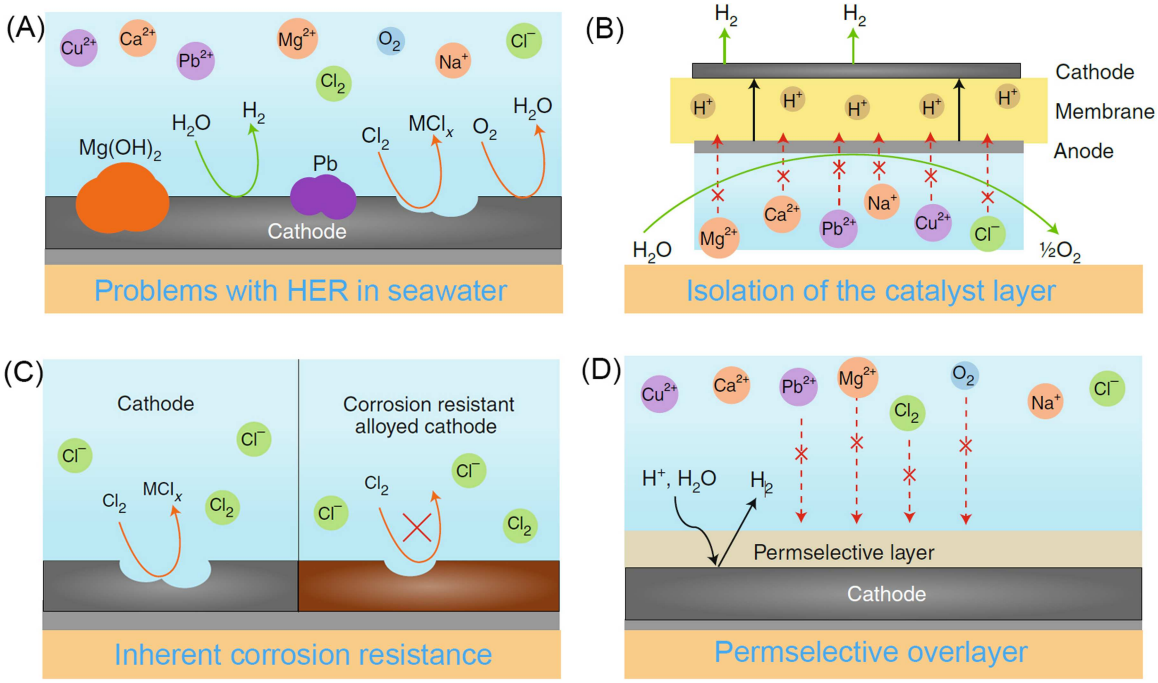

FIGURE 16 | Challenges and potential solutions to improve long-term stability of the HER in low-grade water. Reproduced with permission [172]. Copyright 2020, Springer Nature.

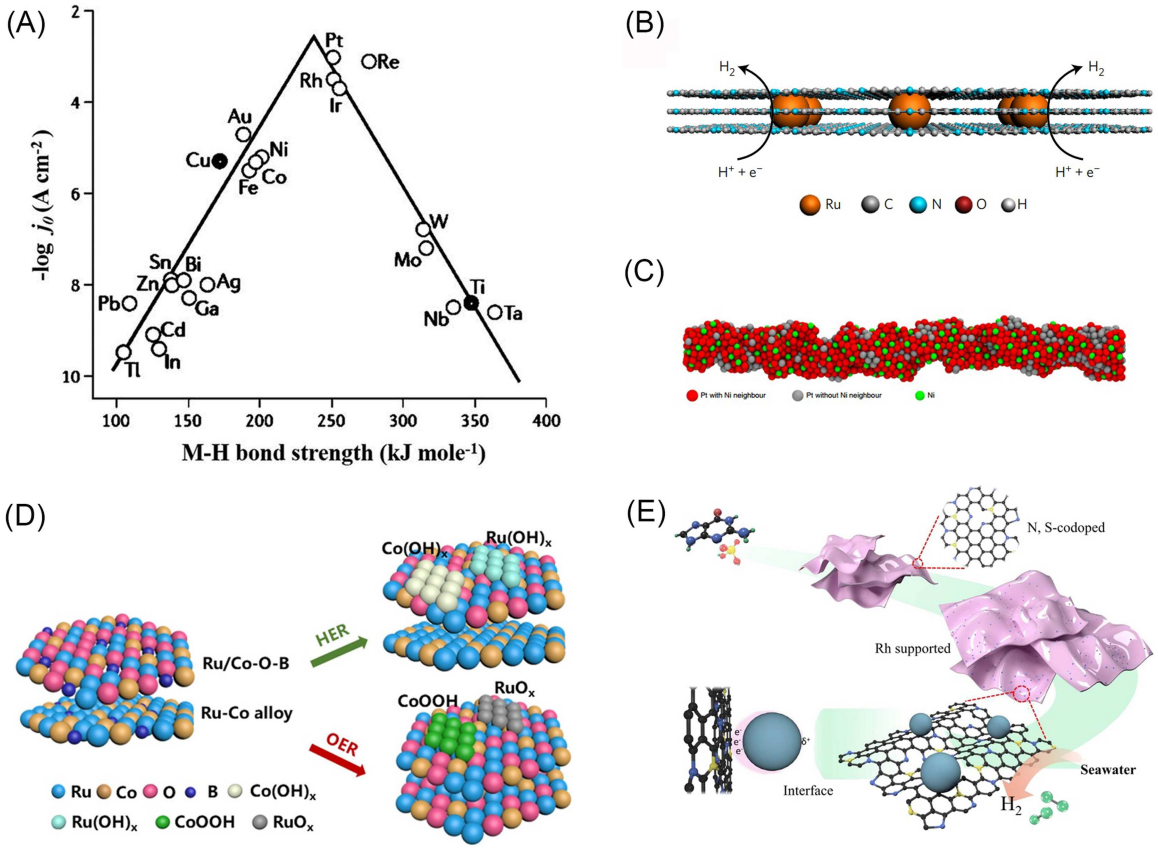

FIGURE 17 | (A) Volcano plots for the HER. Reproduced with permission [178]. Copyright 1972, Elsevier. (B) Schematic illustration of the structure of Ru@C_2N electrocatalyst. Reproduced with permission [179]. Copyright 2017, Springer Nature. (C) Schematic diagram for SANi-PtNWs. Reproduced with permission [180]. Copyright 2019, Springer Nature. (D) Schematic illustration of Ru_2Co_1BO-350 surface reconstructed in the HER and OER. Reproduced with permission [181]. Copyright 2023, American Chemical Society. (E) Preparation of Rh-GS1000 materials. Reproduced with permission [182]. Copyright 2019, American Chemical Society.

2767441x, 2026, 3, Downloaded from https://onlinelibrary.wiley.com/doi/10.1002/idm2.70047 by Battelle Memorial Institute Pacific Northwest Division, Wiley Online Library on [22/06/2026]. See the Terms and Conditions (https://onlinelibrary.wiley.com/terms-and-conditions) on Wiley Online Library for rules of use; OA articles are governed by the applicable Creative Commons License

deposition (ALD) technique, Cheng et al. loaded Pt single atoms, clusters and nanoparticles on N-doped graphene nanosheets to generate efficient HER catalysts [185]. These ALDPt/NGNs catalysts have higher HER catalytic activities, associated with Tafel slopes of 29 mV/dec, than that of the commercial Pt/C catalyst. The reason for this activity is the presence of partial unoccupied density of states in 5d orbital of the Pt atom on N-doped graphene in the ALDPt/NGNs. ALD50Pt/NGNs catalyst have excellent stabilities, with their activities remaining almost unchanged after 1000 HER cycles. Ru, a less expensive substitute for Pt, has a similar bond strength with hydrogen as does Pt. Mahmood et al. reported that Ru nanoparticles dispersed on two-dimensional C_2N support, has a comparable catalytic HER activity to that of Pt/C (Figure 17B) [179]. The capacity for hydrogen adsorption and desorption on the surface of this catalyst plays a key role in regulating the HER reaction rate. Noble metal Ir facets (111) possess thermal stability and relatively balanced hydrogen adsorption/desorption capacity, making it an ideal alternative to Pt in HER catalysts. Li et al. found that interaction between electronegative N atoms and Ir reduces the energy of the unfilled metal d orbital leading to effective balancing of the hydrogen adsorption/desorption processes [186]. When the mass loading of Ir nanoparticles in the nitrogenated carbon support reaches 7.16 wt%, is catalysis of the HER has only a small overpotential of 4.5 mV at 10 mA/cm^2.

Although noble metal-based catalysts display high electrocatalytic performances, their intrinsic high costs, and poor stabilities and scarcities restrict their use for large-scale hydrogen production driven by marine energy. However, material surface engineering, defect engineering and alloying methods have been devised to enhance their HER performance [187, 188]. Recently, the high cost problem associated with HER catalysts has been somewhat alleviated by reducing the mass loading of noble metals or forming alloys with inexpensive transition metals (Fe, Co, or Ni). d-orbital interactions between transition metals and Pt in the alloy materials is conducive to adsorption of H atoms on the catalyst and consequent acceleration of hydrogen generation from seawater. For example, Duan's group, using an electrochemical dealloying-based single atom tailoring strategy, prepared Pt nanowires modified by Ni single atoms that have improved HER activities owing to a minimization of the loss of surface active sites (Figure 17C) [180]. In further studies of the properties of different transition metal alloys with Pt, Zheng et al. prepared PtM (M = Fe, Co, Ni, Cr, Mo) alloy modified Ti mesh by using electrodeposition [189]. The authors emphasized that transition metals in the alloys participate in the reaction between platinum and Cl_2 in seawater, which is beneficial to improve the corrosion resistance and long-term stability of the catalyst. Similarly, Li et al prepared Pt-Ru-M (M = Cr, Fe, Co, Ni, Mo) supported on Ti mesh using the same method [190]. The optimized nanoporous Pt-Ru-Mo catalyst prepared in this manner contains more active sites for the HER and maintains it catalytic function for 172 h. Shen et al. reported a highly active RuCoBO-based catalyst that has high stability and Cl^- corrosion resistance [181]. Surface reconstruction of the catalyst occurs during the HER and results in a modified catalyst that has an overpotential of 14 mV and continuous seawater splitting activity for up to 230 h at 50 and 100 mA/cm^2 (Figure 17D). Defects on the catalyst surface are thought to be active sites that adsorb H_2O to form M—H bonds. Liu et al. described N/S co-doped carbon nanosheets modified with Rh nanoparticles (Figure 17E) [182]. The results of studies with this material show that the heteroatom dopant enhances the interaction between Rh and the carbon matrix by forming an electron-rich interface. This catalyst exhibits high HER activity and stability, and its current density remained at 95% after promoting the HER in seawater for 10 h.

3.2.2 | *Non-Noble Metal-Based Catalysts*

To make the conversion of electricity generated from marine energy to hydrogen for transmission cost effective, it is imperative to develop less expensive non-noble metal-based HER catalysts. Non-noble metal catalysts, including transition metal Mo-, Ni-, and Co-based materials, have moderate H* adsorption/desorption capacities. This feature coupled with recent progress that has been made in theoretical studies and advanced characterization methods have led to rapid development of non-noble metal-based HER catalysts.

Ni/Co-based catalysts are the most popular, widely utilized non-noble metal-based HER catalysts. Element doping can be used to introduce active sites in these catalysts, adjust electronic structures and increase surface roughness, which elevate the performance of Ni/Co-based catalysts in the seawater HER. Du et al. developed a NiFe layered double hydroxide electrode [191]. The catalyst exhibits excellent stability over 9000 h under 1.0 A cm^{-2} in alkaline natural seawater. Also, Ma et al. prepared N-doped carbon shell-coated CoMoP employing a one-step pyrolysis protocol (Figure 18A–C) [192]. The carbon layer in this material protects the catalyst from deactivation by microorganisms and other impurities in seawater. Moreover, N doping increases the electron density of the graphite carbon layer and the H adsorption free energy. In seawater, the prepared catalyst has an excellent HER performance with a high FE of 92.5%.

The alloying effect occurring between transition metals can lead to an increase in the numbers of catalytically active sites in HER catalysts. In this regard, Zhang et al. constructed NiM (M = Co, Cu, Mo, Au, Pt) alloy on Ti foil via electrodeposition as a new catalyst for the HER. The Ni—M bond in this material promotes dissociation of HO—H bond, which is conducive to adsorption and desorption of H*, and a resultant significantly improved HER activity [194]. A system using an optimized Ti/NiCo electrode promotes hydrogen generation in seawater over a 10 h period.

Mo-based materials such as molybdenum carbide (Mo_xC), nitride (Mo_xN_y), phosphide (Mo_xP) and sulfide (MoS_x) are highly abundant and catalytic active HER catalysts. Mo_xC is an ideal substitute for Pt in electrocatalysts because of its similar D-band electronic structure. Abudula et al. has reviewed the preparation of Mo_xC and its application as a catalyst for the HER [195]. In an important effort, Liu et al. developed a HER catalyst composed of embedded Mo_2C/MoP hybrid nanoparticles on a N, P co-doped carbon nanofiber support [196]. The nature of the Mo species on the doped Mo_2C/MoP hybrid-based catalyst electrode was adjusted by changing the annealing temperature. In seawater, the overpotential of the optimized catalyst for the HER is 346 mV at a current density of 10 mA/cm^2, and its activity is stable for long time periods. Wang et al. proposed

2767441x, 2026, 3, Downloaded from https://onlinelibrary.wiley.com/doi/10.1002/idm2.70047 by Battelle Memorial Institute Pacific Northwest Division, Wiley Online Library on [22/06/2026]. See the Terms and Conditions (https://onlinelibrary.wiley.com/terms-and-conditions) on Wiley Online Library for rules of use; OA articles are governed by the applicable Creative Commons License

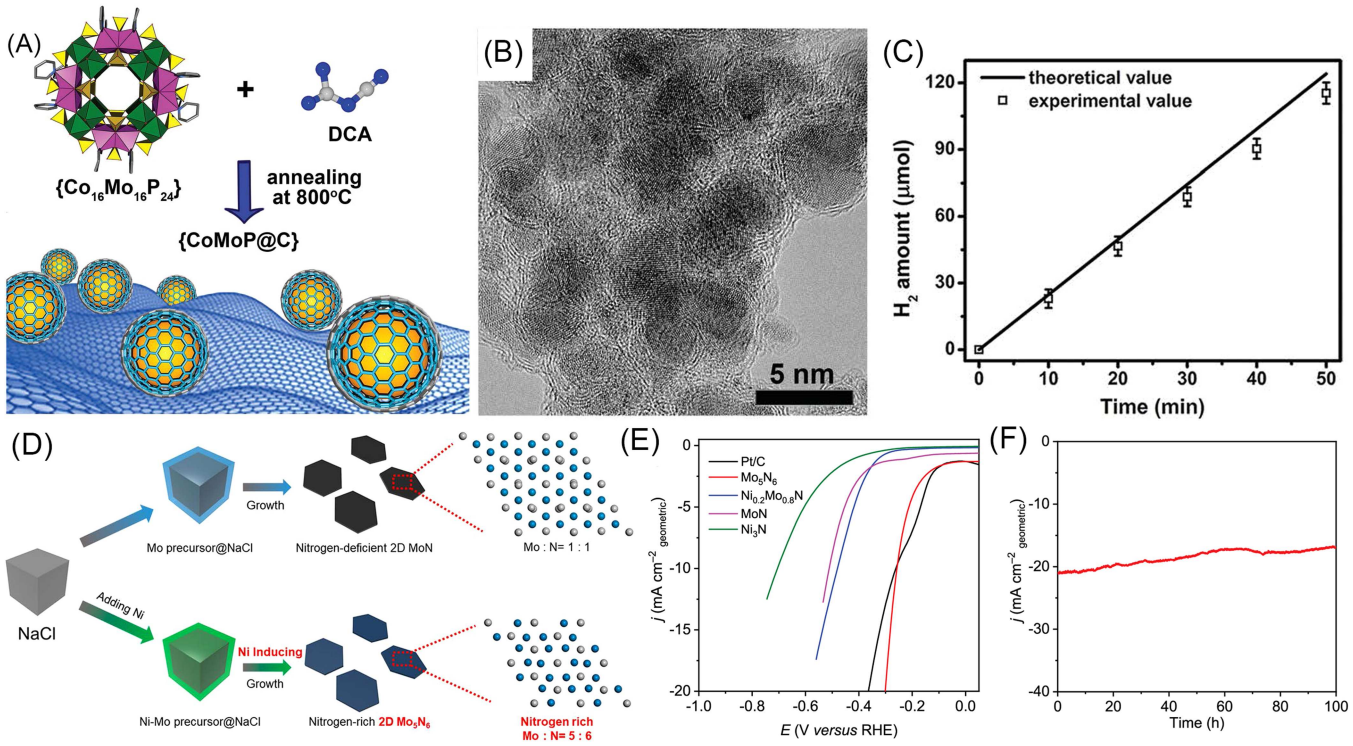

FIGURE 18 | (A) Illustration of the preparation of CoMoP@C. (B) HRTEM image of CoMoP@C. (C) Faradaic efficiency of CoMoP@C toward the HER in seawater at the overpotential of 600 mV. Reproduced with permission [192]. Copyright 2017, Royal Society of Chemistry. (D) Schematic illustration of the synthesis of MoN and Mo_5N_6 nanosheets through ammonization with and without Ni in the precursor. (E) Linear sweep voltammetry curves of different catalysts measured in Ar-saturated natural seawater. (F) Chronoamperometric curve of Mo_5N_6 over 100 h operation using an applied potential of 310 mV. Reproduced with permission [193]. Copyright 2018, American Chemical Society.

incorporating high-valence molybdenum into $Ni(OH)_2$ to enhance both the selectivity and catalytic activity of the OER in alkaline seawater [197]. The introduction of Mo also accelerates the phase transition of $Ni(OH)_2$, redistributes local electronic charge, and promotes a lattice oxygen-mediated reaction pathway.

Mo_xN_y has an inherently outstanding electronic structure and conductivity for use as an electrocatalyst, but it is vulnerable to seawater corrosion. To circumvent this deleterious property, Miao et al. encapsulated *h*-MoN nanoparticles in B/N co-doped CNTs, to avoid agglomeration and seawater erosion [198]. In addition, the high valence state of Mo in Mo_xN_y contributes to making the catalyst resistant to seawater-induced corrosion. Qiao's group reported that an atomically thin Mo_5N_6 nanosheet with a Pt like electronic structure maintains a stable HER catalytic current in seawater for 100 h, and the existence of a high valence state of Mo (+4) in the catalyst prevents active site damage caused by seawater ions (Figure 18D–F) [193]. Phosphidation can potentially change the properties of Mo and improve the activity and stability of Mo-based HER catalysts. Xiao et al. found that MoP catalyst possessing a higher P content displays a better HER performance than do Mo_3P and Mo [199]. The results of theoretical calculations show that the function of P in the composite is equivalent to that of S in MoS_2 in that both provide large numbers of edge active sites. Also, compared with molybdenum phosphide, molybdenum sulfide possesses poor electrical conductivity. Kim's group developed a hybrid HER catalyst that contains a combination of amorphous MoS_x layers and vertical N-doped CNT arrays [200]. Owing to the existence of abundant active sites on the surface of MoS_x and rapid charge transfer in the one-dimensional CNT, the current density of the catalyst is 10 mA/cm^2 at only ca. 110 mV.

4 | Materials for Marine Energy Storage and Utilization

The supply of marine energy is limited by volatility, intermittency, and instability owing to region distribution dependent factors. As a result, efficient energy storage devices that have good grid connections and efficient time dependent access include secondary batteries, represented by lithium ion batteries (LIBs), and supercapacitors, which are the two most prominent and complementary candidates for maritime applications [201–203]. LIBs, the current cornerstone of portable and mobile marine energy storage (e.g., for autonomous underwater vehicles and electric ships), are highlighted first due to their high energy density. LIBs use carbon or Si-based materials as negative electrodes and lithium containing compounds as positive electrodes, and they function by movement of lithium ions between two electrodes [204–206]. LIBs possess several advantageous properties including high operating voltages and energy densities, and long cycle life-times, but their power densities are unsatisfactorily low. LIBs do play important but indirect roles in marine applications such as electric ship and underwater glider propulsion [207–209]. To address the power density limitations of LIBs and manage rapid load fluctuations, supercapacitors are utilized as a vital complementary technology. As a family of energy storage devices, supercapacitors have high power

2767441x, 2026, 3, Downloaded from https://onlinelibrary.wiley.com/doi/10.1002/idm2.70047 by Battelle Memorial Institute Pacific Northwest Division, Wiley Online Library on [22/06/2026]. See the Terms and Conditions (https://onlinelibrary.wiley.com/terms-and-conditions) on Wiley Online Library for rules of use; OA articles are governed by the applicable Creative Commons License

densities (~100 kW/kg) and long cycle life-times (> 100 000 cycles). These types of energy storage devices can be divided into two categories. The first includes electric double layer capacitors (EDLCs), which operate by a physical energy storage mechanism associated with ion adsorption/desorption, while the second group covers pseudocapacitors that function using a reversible surface redox reaction mechanism. Electrode materials for supercapacitors include porous carbon with high specific surface areas, polymers and metal oxides [210, 211]. While other battery technologies (e.g., solid-state, lead-acid, flow, or seawater-based zinc batteries) are employed or investigated in specific marine scenarios, LIBs and supercapacitors are the primary focus of this section because of their widespread applicability and active material research focus. Accordingly, the development of energy storage devices and corresponding materials that possess both high energy and power densities is the focus of studies exploring marine energy storage and utilization.

4.1 | Materials for Lithium-Ion Battery Electrode

Among the array of electrochemical energy storage technologies, LIBs are accorded particular emphasis due to their paramount importance in portable and mobile marine energy systems. While alternative systems, including solid-state batteries (valued for enhanced safety in deep-sea operations), flow batteries (suited to large-scale stationary storage), and conventional lead-acid batteries, have specific niches in maritime applications, the material science of LIBs most comprehensively encapsulates the overarching research thrusts aimed at achieving greater energy density, extended service life, and enhanced durability under marine environmental stresses. Consequently, advances and challenges in developing LIB electrode materials offer a representative and critical lens through which progress in marine-compatible energy storage can be examined.

The key to enhancing the endurance of LIBs lies in the use of robust, marine environment tolerating energy storage materials. Typically utilized LIBs cathode materials include lithium cobalt oxides ($LiCoO_2$, LCO), lithium manganese oxides ($LiMn_2O_4$, LMO), lithium iron phosphates ($LiFePO_4$, LFP) and ternary composites. The inventor of LIBs cathode materials (LCO, LMO, LFP), the Nobel Prize winning scientist J. B. Goodenough, made a revolutionary breakthrough in LIB technology, which not only solved safety problems, but also reduced manufacturing costs [212]. In addition, the anode material governs the ability to reversibly extract and insert of Li^+, a key component of LIBs. Materials used for anodes include carbon, metal oxides, and Si and Sn-based materials. In this group, graphite anodes have been employed in most applications, but their low capacity (372 mAh/g) prevents long-term endurance of LIBs. Thus, it is urgent to develop novel high capacity and low-cost anode materials for next-generation LIBs.

4.1.1 | *Cathode Materials*

LCO, the first LIB cathode material that was commercialized by SONY Corporation in 1992 [202], possesses the advantageous properties including a high working voltage, low self-discharge, high theoretical mass specific capacity (274 mAh/g) and volume specific capacity (1363 mAh/cm^3), as well as a good cycling performance [213]. However, this anode material suffers from high cost owing to the need for Co, low thermal stability and poor safety. Owing to the growing demand for marine equipment that require high endurance batteries, current studies have focused on improving the energy density of LIBs by creating higher voltage LCO materials. As displayed in Figure 19, Li's group developed a heat annealing method for coating LCO with solid electrolyte materials $Li_{1.5}Al_{0.5}Ti_{1.5}(PO_4)_3$, which possess high voltage stable surface layers [214]. The coatings greatly increase the thermal stability of the modified LCOs, which have stable 4.6 V high-voltage cycling performances at both room temperature and 45°C. Metal doping is an effective method to overcome cycle performance degradation caused by changes in the lattice structure of the LCO in the process of high voltage de-lithiation. This research group determined the relationship that exists between the particle structure of micro Ti-Mg-Al co-doped LCO material and the reversibility of the processes occurring during charging and discharging cycles [215, 216]. The results show that doping elements regulate the number and distribution of defects inside LCO particles, which govern the structural phase transition of LCO materials during high voltage operation, and synergistically promote cyclic stability of LCO at high voltages (> 4.5 V). Similarly, Liu et al. developed a battery containing a dual La and Al doped LCO lattice, in which La was acts as a pillar to increase the *c* axis distance and Al serves as a positively charged center to promote diffusion of Li^+ [217]. The optimized LCO created in this effort was shown to inhibit the structural phase transition during the cycle that results in a high capacity of 190 mAh/g. Considering the costs, $LiNiO_2$ (LNO), having the same ideal crystal structure and similar theoretical specific capacity as LCO, has become a candidate material for LIB cathodes [218, 219]. Moreover, metal doping improves the electrochemical performance of the LNO [220, 221]. As a result, $LiNi_{0.8}Co_{0.15}Al_{0.05}O_2$ (NCA) is now a widely used material in commercial LIBs.

The lithium cathode material, LMO, has advantages associated with low cost, large abundance, high-voltage, pollution-free and high safety performance. However, its poor cycling performance

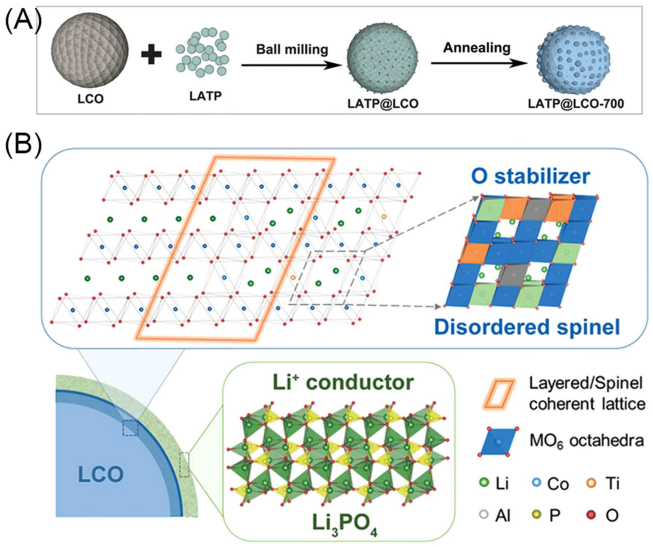

FIGURE 19 | Schematic illustrations of (A) the surface engineering of LCO, and (B) the surface layer growth mechanism. Reproduced with permission [214]. Copyright 2020, Wiley-VCH.

2767441x, 2026, 3, Downloaded from https://onlinelibrary.wiley.com/doi/10.1002/idm2.70047 by Battelle Memorial Institute Pacific Northwest Division, Wiley Online Library on [22/06/2026]. See the Terms and Conditions (https://onlinelibrary.wiley.com/terms-and-conditions) on Wiley Online Library for rules of use; OA articles are governed by the applicable Creative Commons License

and electrochemical stability limit the use of this material for large-scale industrial purposes. In the continuous electrochemical charge–discharge process, because Mn is leached during this process, the structure of LMO can be stabilized by using cationic doping. Su et al. prepared indium/sulfur (In/S) doped LMO with an orthorhombic structure as the cathode material for LIBs by using a hydrothermal method [222]. Compared with its undoped counterpart, In/S doped layered LMO undergoes only partial structural deformation and, as a result, it has improved cycle stability and a high discharge rate.

Pang et al. found that 5% and 10% Cr doping of LMO not only leads to a morphology change and particle size reduction, it also improve cycle performance and reversible capacity [223]. Suresh et al. prepared the Fe and Zn-doped LMOs, $LiMn_{0.95}Zn_{0.05}O_2$ and $LiMn_{0.95}Fe_{0.05}O_2$, by using an ion exchange method, and that they have specific capacities of 180 and 193 mAh/g, respectively [224]. The Zn-doped material has an improved capacity retention only, while the Fe-doped analog has both an improved cyclic stability and specific capacity.

Heterogeneous structure and interface engineering are also useful methods to improve the performance of LMOs. Zhu et al. described the design of a LMO cathode composed of interwoven spinel and layered domains [225], which has an enhanced electrochemical cycle stability. The specific capacity of the modified LMO cathode is 254.3 mAh/g, and the capacity retention rate is about 90.4% after 2000 cycles. In addition, surface coating, oxygen stoichiometry control and cathode material compositing are other methods to improve the electrochemical performance of LMO.

Microwave-assisted synthesis has emerged as a viable method for tuning the physico-chemical and electrochemical properties of LMO and related cathode materials. For example, Nkosi et al. employed both aluminum-doping and microwave to enhance the capacity and capacity retention of LMO [226]. Recently, Haruna et al. showed that microwave irradiation improves the electrochemical performances of LMO by suppressing the Jahn-Teller distortion [227].

LFP, having a theoretical specific capacity of 170 mAh/g, is known to have high cycle stability and good power characteristics, as well as being pollution-free, low cost and high safety. Because of its low ionic conductivity, LFP is usually combined with conductive carbon materials or subjected to cationic doping to improve its electrochemical performance [228–231]. Shin et al. studied the influence of graphite, carbon black and acetylene black coatings on the electrochemical properties of LFP [232]. The results showed that graphite-coated LFP has a lower charge- and Li^+-transfer resistance as well as a stable specific capacity of 120 mAh/g. Zhao et al. prepared a core-shell LFP@C composite using a chemical vapor deposition assisted solid phase reaction, and thoroughly studied the influence of the morphology of this material on electrochemical performance [233]. It should be noted that although introduction of carbon materials improves the conductivity of LFP, it causes the bulk density and the volume specific capacity to be much lower than those of LCO, which hinders its practical application. Fortunately, the related cathode material $LiFeSO_4F$ (LFSF) has a better ionic/electronic conductivity and carbon coating is not needed for its fabrication [234, 235]. LFSF also possesses a high cell voltage and specific capacity of 151 mAh/g. Additional novel cathode materials such as $LiCoPO_4$, $LiNi_{0.5}Co_{0.5}PO_4$ and $Li_3V_2(PO_4)_3$ (LVP) have been developed [236–238]. Among these materials, LVP has an outstanding specific capacity of 197 mAh/g and a high-voltage. Mai's group prepared unique hierarchical LVP/C mesoporous nanowires through a one-pot method (Figure 20A,B), and showed that this material has a high rate and ultra-long life performance [239]. The capacity retention of the nanowires is 88% after 3000 cycles at voltages in the range of 3–4.3 V.

Ternary materials, exemplified by $Li(NiCoMn)O_2$ (NCM) and $Li(NiCoAl)O_2$ (NCA), are multimetallic composite oxides in which the three metals play different roles. Specifically, Ni enhances the materials capacity, Co provides a stable layered structure and Mn (or Al) reduces the cost and improves safety [241, 242]. Ternary composites are among the most promising cathode materials for LIBs, because they have advantageous features including high energy densities, good cycling performances and stable structures. Unfortunately, their initial charging and discharging efficiencies are low. Sun et al. prepared $Li_{1.2}Ni_{0.13}Co_{0.13}Mn_{0.54}O_2$ by using solution assisted co-precipitation and solid state sintering (Figure 20C,D) [240]. The capacity of this cathode material is 186 mAh/g, and it retains 98.5% of its capacity after 200 cycles. Hou et al. showed that coral-like $Li_{1.20}Mn_{0.54}Ni_{0.13}Co_{0.13}O_2$, synthesized by using the hydrothermal method, has a reversible capacity of 210.2 mAh/g, and excellent cycle stability [243]. Also, Jafta et al. [244] combined microwave-assisted synthesis and aluminum-doping to improve the capacity retention of $Li_{1.20}Mn_{0.54}Ni_{0.13}Co_{0.13}O_2$.

4.1.2 | *Anode Materials*

Because of their natural abundance and unique properties, carbon-based materials, including graphite, CNTs, graphene and carbon fibers, have become attractive anode materials for use in LIBs [245–247]. Graphite is currently the preferred anode material for commercial LIBs, but its capacity limitations hinder high-endurance marine applications. Modification of natural graphite by shortening the Li^+ diffusion path, extending the graphite layer spacing and modifying the interface coating have been carried out to optimize its microstructure and specific capacity. Cheng et al. found that forming abundant nanopore channels on the graphite surface using KOH etching effectively shortens the ion diffusion path and increases the charging performance (Figure 21A,B) [248]. Kim et al. observed that expansion of the graphite layer spacing from 0.3359 to 0.3395 nm leads to creation of large numbers of functional groups [250].

In addition, studies have demonstrated that novel carbon anodes have greatly improved electrochemical performances in LIBs. Landi et al. reviewed applications of single-wall CNTs, multi-wall CNTs and their composites to LIBs, and summarized existing methods and proposed new methods to improve the capacity and electrical transport of these anode materials [251]. Although graphene possesses a high conductivity and high capacity, its use in LIBs is hindered by its large initial irreversible capacity loss and low initial coulombic efficiency (CE), as well its high price. Studies have shown that the electrochemical properties of graphene can be improved by altering the graphitization level, and by introducing heteroatom dopants and porous structural features. Zhao's research group

2767441x, 2026, 3, Downloaded from https://onlinelibrary.wiley.com/doi/10.1002/idm2.70047 by Battelle Memorial Institute Pacific Northwest Division, Wiley Online Library on [22/06/2026]. See the Terms and Conditions (https://onlinelibrary.wiley.com/terms-and-conditions) on Wiley Online Library for rules of use; OA articles are governed by the applicable Creative Commons License

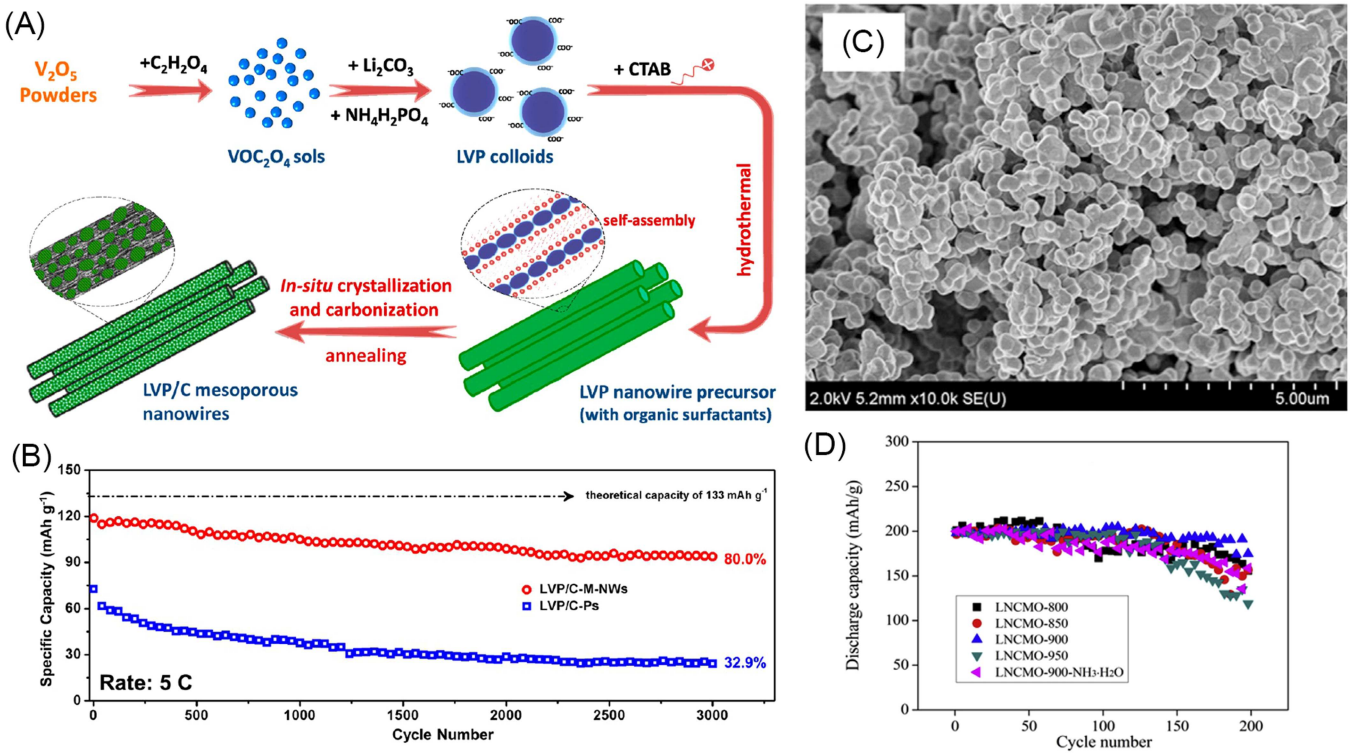

FIGURE 20 | (A) Schematic illustration of the fabrication steps and proposed formation mechanism for LVP/C-M-NWs, (B) ultralong-life cycling performance of the LVP/C-M-NWs and LVP/C-Ps at 5 C. Reproduced with permission [239]. Copyright 2014, American Chemical Society. (C) SEM image of cathode material LNCMO-900, (D) cycling discharge capacities of LNCMO-T and LNMCO-900-NH_3·H_2O cathode materials. Reproduced with permission [240]. Copyright 2017, Elsevier.

reported the results of a study of a mesoporous graphene nanosheet anode material [249]. Ordered mesoporous graphene has a high surface area for Li^+ adsorption and insertion. As a result, it has the excellent reversible capacity of 1040 mAh/g at a current density of 100 mA/g (Figure 21C,D). It is worth mentioning that carbon fiber anode materials with one-dimensional structures have unique advantages for improving the Li^+ diffusion rate. Qie et al. generated a high-performance carbon fiber anode material by carbonization of PPy with KOH [252]. Owing to its unique porous nanostructure and high N dopant content, this anode material retains a high reversible capacity of 943 mAh/g after 600 cycles at a high current density of 2 A/g. Xia et al. prepared B and N double-doped 3D carbon nanofibers as ideal anode materials, which have a capacity retention of 87% after 5000 charge/discharge cycles at 2 A/g [253]. In addition to those described above, other new carbon materials, including MOF derived, graphdiyne and biomass carbon materials, have been developed and applied to LIB technologies [254–256].

Alloy-based materials, consisting mainly of metallic (Sn, Sb) and semi-metallic (Si, Ge) elements in the IVA and VA groups, form binary compounds with lithium. The respective theoretical reversible capacities of $Li_{4.4}Si$, $Li_{4.4}Sn$, $Li_{4.4}Ge$ and Li_3Sb of 4200, 994, 1625 and 665 mAh/g are much higher than those of traditional carbon materials [257]. Therefore, alloy-based anode materials can significantly increase the overall energy density of LIBs to levels that meet the requirements of electric ships, underwater gliders and other marine equipment. However, alloy-based materials tend to undergo volume changes and pulverization during the charge/discharge process, which reduces the mechanical stability of active material, thus, limits rate capacity and cycle stability [258, 259].

Si is considered to be an ideal substitute anode material for graphite because of its abundant reserves, environmentally friendliness and high capacity [260–262]. However, the huge volume expansion of about 300% that takes place upon full lithification and low intrinsic conductivity limit its commercial applications [263]. Therefore, Si is often compounded with carbon materials to optimize the lithium storage performance of anode materials. Cui's research group reported that a mixed anode composed of graphite/carbon embedded in Si nanolayers (SGC) has a high first-cycle CE of 92% [264]. The unique structural design improves the compatibility of Si and graphite, and solves problems caused by structural failure caused by volume expansion. The energy density of SGC is 1043 Wh/L when used as an anode with a LCO cathode in a full cell. Furthermore, this group designed novel yolk-shell structured, Si nanoparticle coated, amorphous carbon shells [265]. The cavity between Si particles and shell allows for free expansion of the Si particles during the charge/discharge process, which gives the anode a high capacity and a long cycle lifetime (Figure 22A,B). Compared with that of the Si material, the volume of silica derivative-based materials changes to lesser extents (~150%) during a cycle. Mai's group reviewed the synthesis and lithium storage properties of the promising anode material silicon oxide [272]. This group designed and prepared a series of silica-oxide-based anode materials (Figure 22C–H), including monodisperse SiO_x/C microspheres, yolk@shell SiO_x/C microspheres, SiO_x/C@C microspheres, pomegranate-like SiO_x/C microspheres, Ni/SiO_2 microspheres and TiO_2/SiO_x hybrid, all of which have excellent lithium storage performances [266–271].

2767441x, 2026, 3, Downloaded from https://onlinelibrary.wiley.com/doi/10.1002/idm2.70047 by Battelle Memorial Institute Pacific Northwest Division, Wiley Online Library on [22/06/2026]. See the Terms and Conditions (https://onlinelibrary.wiley.com/terms-and-conditions) on Wiley Online Library for rules of use; OA articles are governed by the applicable Creative Commons License

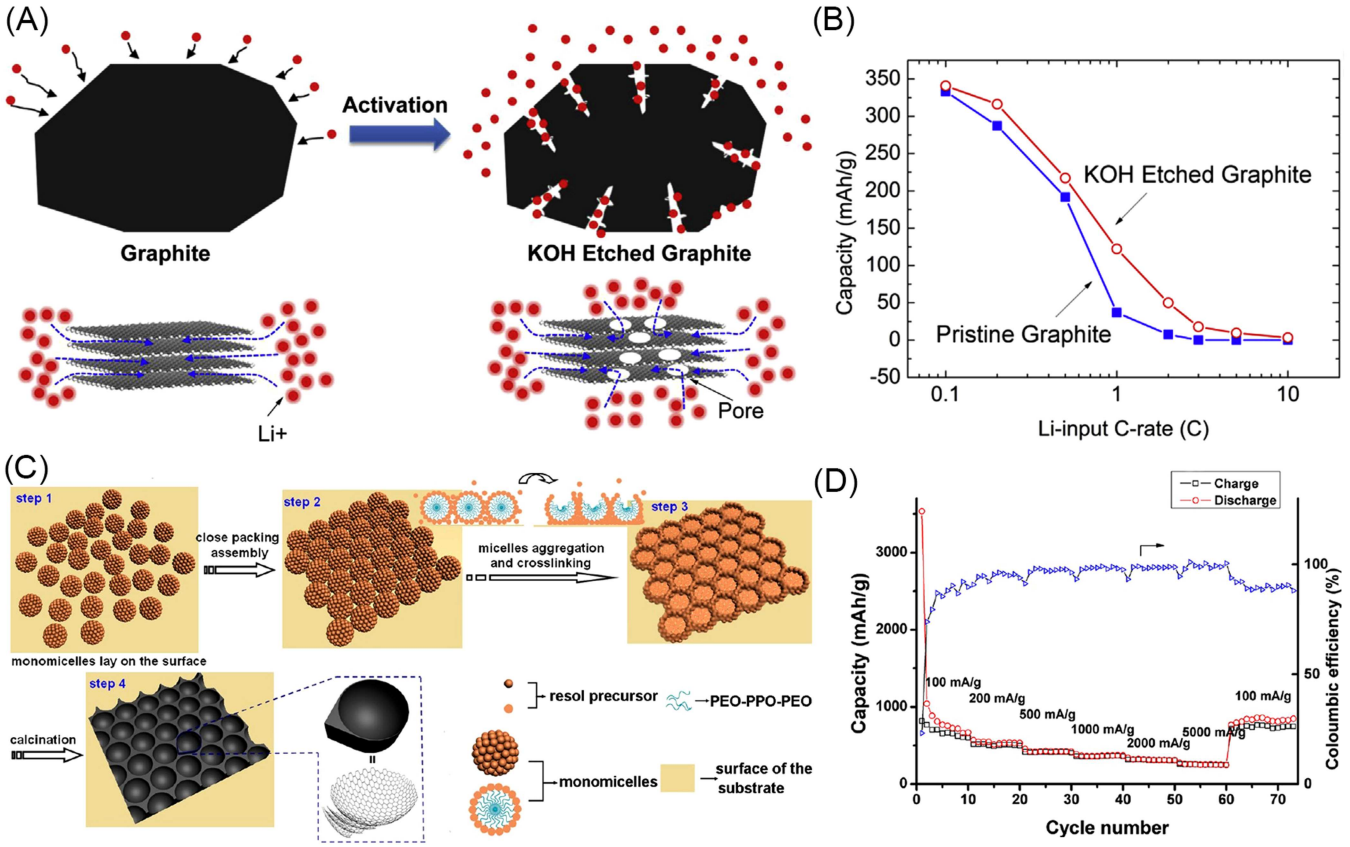

FIGURE 21 | (A) Schematic of pristine and KOH etched graphite. (B) Li-input rate capability of pristine and KOH etched graphite in a half cell. Reproduced with permission [248]. Copyright 2015, Elsevier. (C) Schematic of the formation of ordered mesoporous graphene nanosheets. (D) Cycling performance and the coulombic efficiency of the mesoporous graphene nanosheets at different current densities. Reproduced with permission [249]. Copyright 2013, American Chemical Society.

In addition to Si, Sn and Ge are also commonly used as LIBs anode materials. During lithification, the critical size of a Sn particle fracture is smaller than that of Si. Xu et al found that mechanical damage still occurs when the Sn particle size is 10 nm [273]. Alloying Sn with Fe, Co and other non-active metals effectively alleviates volume expansion. Wang et al. demonstrated that CoSn@C nanocubes have a discharge capacity of 1010.9 mAh/g at 0.5 A/g [274]. Moreover, considering that the conductivity and Li^+ diffusion rate in Ge are higher than those in Si, Wang et al. uniformly embedded Ge quantum dots in a 3D porous carbon framework. The results show that this change effectively reduces the volume change occurring during the process [275]. As an anode, this material has a specific capacity of 1160 mAh/g at 1 A/g, and a capacity retention of more than 90% after 1200 cycles.

Metal oxides and chalcogenides, and organic materials are also commonly used for construction of LIBs anodes. Li et al. summarized and analyzed the status of studies focusing on fast charging anode materials, and discussed modification strategies as well as the mechanism for lithium storage [204]. Similarly, Mahmood et al. reviewed nanostructured LIB anode materials, proposed solutions to challenges facing their applications, and highlighted the importance of methods for in-situ characterization of the lithium storage process [276].

Continuous advancements in both cathode and anode materials are essential to support the large-scale deployment of LIBs in marine energy storage by achieving higher energy density, longer cycle life, and enhanced safety. Beyond these performance metrics, the sustainable supply of lithium—a critical raw material—presents a growing strategic concern. In this regard, the development of efficient technologies for extracting lithium directly from seawater aligns closely with the marine energy theme and offers a promising pathway to ensure resource sustainability.

4.2 | Materials for Supercapacitor Electrode

Supercapacitors have uniquely high-power densities (> 100 kW/kg), long cycle life-times (> 100 000 cycles), wide performance temperatures (−40°C–60°C) and rapid charging capacities (< 3 min). The maritime industry has become increasingly interested in using supercapacitors, especially those for driving high-power equipment [201, 277]. The use of supercapacitors to overcome the impact of power fluctuations on marine electric propulsion systems has become a new approach to the development of future marine propulsion technologies. However, supercapacitors have low energy densities that are far inferior to those of LIBs in terms of endurance over long-distances.

According to the energy density formula ($E = 0.5CV^2$, where E is the energy density, C is the specific capacitance, and V is the operating voltage), an effective way to improve the energy density of devices involves increasing specific capacitance by designing and preparing electrode materials with high specific surface areas and high porosities [278–280]. Porous carbon

2767441x, 2026, 3, Downloaded from https://onlinelibrary.wiley.com/doi/10.1002/idm2.70047 by Battelle Memorial Institute Pacific Northwest Division, Wiley Online Library on [22/06/2026]. See the Terms and Conditions (https://onlinelibrary.wiley.com/terms-and-conditions) on Wiley Online Library for rules of use; OA articles are governed by the applicable Creative Commons License

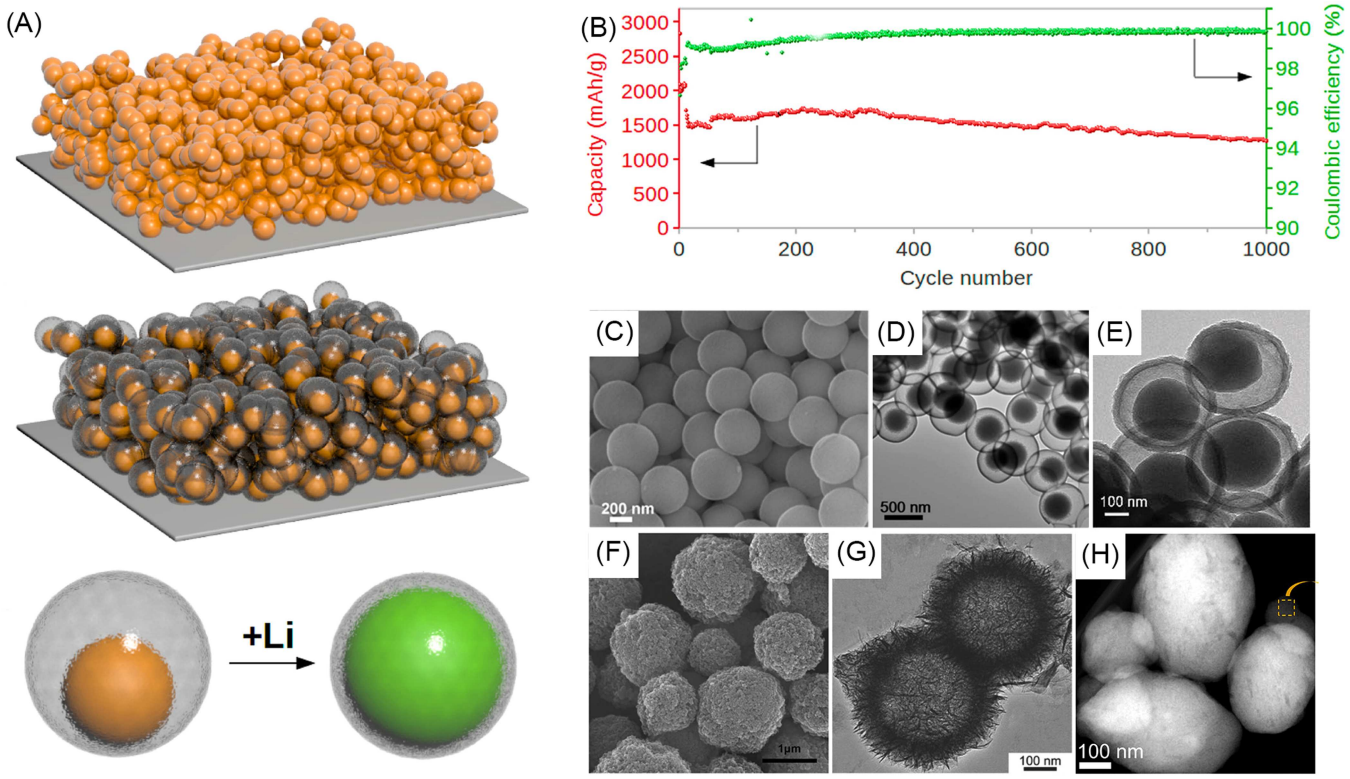

FIGURE 22 | (A) Schematic of the materials design of a conventional slurry coated SiNP electrode and a novel Si@void@C electrode. A magnified schematic of an individual Si@void@C particle showing that the SiNP expands without breaking the carbon coating or disrupting the SEI layer on the outer surface. (B) Electrochemical cycling results for Si@void@C electrodes. Delithiation capacity and CE of the first 1000 galvanostatic cycles between 0.01 and −1 V (alginate binder). Reproduced with permission [265]. Copyright 2012, American Chemical Society. (C) SEM image of SiO_x/C-2. Reproduced with permission [266]. Copyright 2018, Elsevier. (D) TEM image of SiO_x/C. Reproduced with permission [267]. Copyright 2019, Elsevier. (E) TEM image of YS-SiO_x/C@C. Reproduced with permission [268]. Copyright 2020, Royal Society of Chemistry. (F) SEM image of pomegranate-like SiO_x/C microspheres. Reproduced with permission [269]. Copyright 2018, Royal Society of Chemistry. (G) TEM image of Ni/SiO_2-550. Reproduced with permission [270]. Copyright 2018, Wiley-VCH. (H) HAADF-STEM image of the TiO_2/SiO_x hybrid. Reproduced with permission [271]. Copyright 2023, American Chemical Society.

materials, including carbon nanospheres and nanofibers, modified graphene, 3D carbon aerogels, and novel carbon nanocages and graphynes are typically utilized as electrode materials [281–284]. Differing from the carbon materials used in anodes of LIBs, porous carbon materials used in supercapacitors must possess high specific surface areas, hierarchical pore structures, high conductivities and high electrolyte wettabilities in order for ion absorption/desorption to occur rapidly. Moreover, transition metal oxides and hydroxides as well as conductive polymers are often used as pseudocapacitor electrode materials [285, 286]. Because the energy storage process in pseudocapacitors involves chemical reactions, the specific capacitances of these types of materials are high, but their chemical side reaction promoted irreversibility causes their cycle stabilities to be lower than those of EDLCs. For marine equipment applications, it is critical to create supercapacitor devices with both high energy and power densities.

4.2.1 | *Porous Carbon Materials for EDLCs*

Porous carbon materials account for ~30% of the production cost of supercapacitors containing energy storage devices. Currently, commercial carbon materials are prepared mainly by activation of biomass carbon such as that found in coconut shells [287]. However, it is difficult to accurately control the pore structures of carbon materials. As a result, fully utilizing the pore structures of carbon materials to improve their specific capacitance remains the focus of ongoing investigations. In recent years, porous carbon materials having different dimensions have been developed, including 0D carbon quantum dots and nanospheres, 1D CNTs and carbon fibers, 2D modified graphene and carbon nanosheets, and 3D carbon aerogels. As a consequence of these efforts, specific capacitance of carbon materials-based supercapacitors has significantly improved.

Carbon nanospheres are comprised of four types of structure classes including solid, hollow, yolk@shell and multi-shell spheres. All members of this group have good structural regularity, adjustable porosity and a low price [288–290]. In addition, functional porous carbon spheres can be generated by surface modification, heterogeneous element doping and graphitization. Xu et al. has reviewed the controlled synthesis of porous carbon spheres used for supercapacitors, and discussed the correlation that exists between the structures and electrochemical properties of materials [281]. Phenolic resin is a suitable precursor for preparing carbon nanospheres with controlled particle sizes and pore structures [288, 291]. Lu et al. reported the preparation of monodisperse phenolic resin spheres and porous carbon spheres with controllable sizes by using an extension of the Stöber method which utilizes

2767441x, 2026, 3, Downloaded from https://onlinelibrary.wiley.com/doi/10.1002/idm2.70047 by Battelle Memorial Institute Pacific Northwest Division, Wiley Online Library on [22/06/2026]. See the Terms and Conditions (https://onlinelibrary.wiley.com/terms-and-conditions) on Wiley Online Library for rules of use; OA articles are governed by the applicable Creative Commons License

ammonia-ethanol as the solvent system [292]. Yu et al. carried out mass production of monodispersed resin and carbon spheres in pure water by using self-catalytic polymerization. The specific capacitance of N and O co-doped carbon spheres is 282 F/g [293]. Additionally, hollow and yolk-shell carbon spheres possessing cavity structures have high specific surface areas and short ion diffusion distances. By using a one-pot strategy, Zhang et al. prepared hollow mesoporous spheres (MCHS) with a surface area of 1582 m^2/g and adjustable micropore size of 13.9 nm [294]. The specific capacitance of MCHS in EDLCs is 310 F/g, and the capacity retention is 98.6% after 10 000 cycles. More recently, Kim et al. developed a novel method to produce carbon nanospheres which takes advantage of inhibition of the pyrolytic condensation of polymers (Figure 23A–C). The rich distribution of micropores and mesopores in this material leads to a BET surface area of 1124 m^2/g and a specific capacitance of 389 F/g at 1 A/g [295]. Carbon nanospheres with complex structures have excellent capacitances, but their synthesis often requires the use of templates, surfactants and other additives, which are unfavored in commercial applications. Thus, simple, low-cost methods for preparing carbon nanospheres with high specific surface areas and porosities are required.

Carbon nanofibers are an ideal EDLCs electrode material owing to their high aspect ratio and anisotropy, which in supercapacitors lead to rapid axial electron transport and radial ion diffusion. 1D carbon nanofibers are synthesized mainly by utilizing either the soft or hard template method and electrospinning [297–299]. Yu et al. described a method for construction of a new, ultrafine, N-doped carbon nanofiber (N–CNFs) based on self-assembly of phenolic resin and surfactant (Figure 23D–F). The nanofibers have a respective maximum gravimetric specific capacitance and energy density of 380 F/g and 12.35 Wh/kg [296]. Chen et al. reported the carbon nanofibers prepared using a hard Te template and surface coating with PPy, can be employed as high-capacity porous carbon nanofiber electrode materials [282]. The nitrogen dopant content and specific surface area of these materials are 7.22% and 562 m^2/g, respectively, and the maximum power density is 89.57 kW/kg. Mesoporous carbon nanofibers were prepared by Tan et al. using an electrospinning method. This material was utilized as a flexible freestanding electrode for and EDLC that has a specific capacitance of 327 F/g at 1 A/g [300]. CNTs, an important family of 1D carbon materials, are often used as self-supporting flexible electrodes because they have a superior electrical conductivity, and more defined pore structure and stability than those of carbon nanofibers. Lu et al. created a vertically arranged CNTs containing plasma etching derived defects for use as an EDLCs electrode material [301]. The high charge storage/delivery capability of CNTs results in an energy density of 148 Wh/kg and power density of 315 kW/kg. However, the relatively high cost of preparation of CNTs hinders large-scale commercial production. In addition, some 1D carbon materials derived from bacterial cellulose are also used as electrode materials for supercapacitors.

2D layered carbon materials such as graphene and carbon nanosheets are highly suitable as electrode materials for supercapacitors because they have abundant active sites and highly specific surface areas. By using microwave exfoliation and KOH activation, Zhu et al. achieved a breakthrough in generating graphene having a specific surface area of 3100 m^2/g [302]. This 2D highly porous carbon layers in this material consist almost entirely of sp^2-bonded carbons, which is the reason why it has ideal capacitive properties associated with an energy density of 70 Wh/kg and a power density of 250 kW/kg. Due to the existence of van der Waals forces between layers, the 2D graphene sheets undergo ready accumulation and agglomeration. However, inserting other carbon materials between these layers

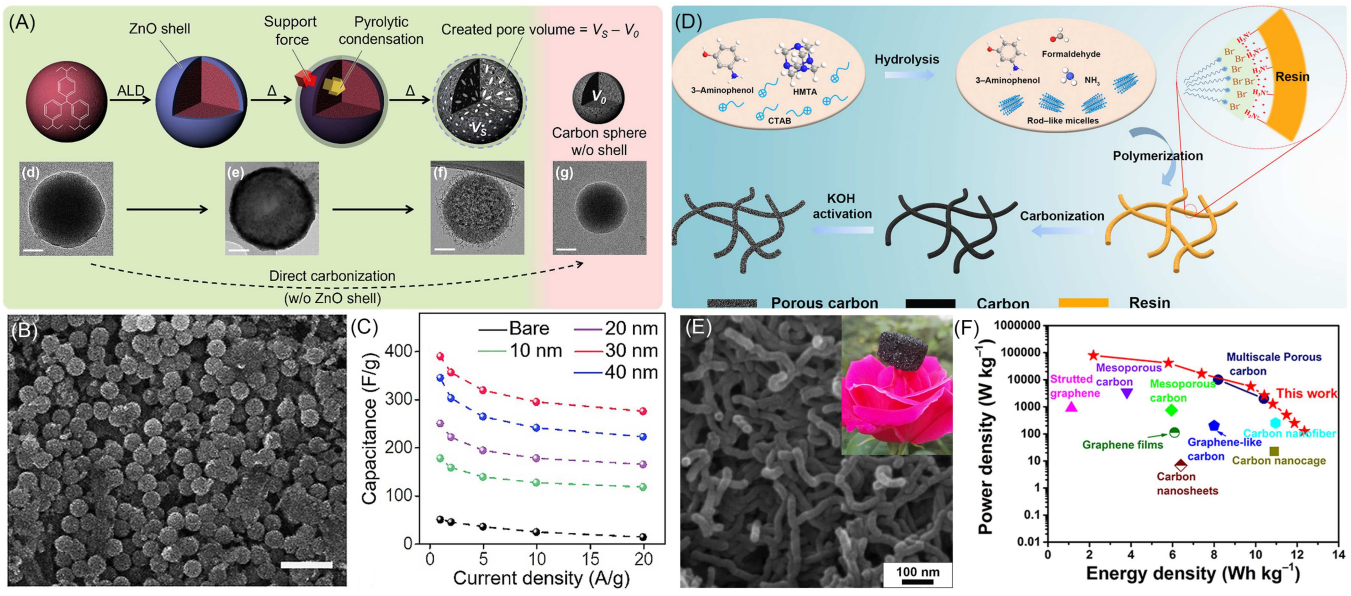

FIGURE 23 | (A) Preparation of porous carbon materials based on inhibition of pyrolytic shrinkage of polymer particles using ZnO shells. (B) SEM image of porous carbon nanosphere electrodes (scale bar: 1 μm). (C) Capacitances at current densities from 1 to 20 A/g. Reproduced under terms of the CC-BY license [295]. Copyright 2023, The Authors, published by PNAS. (D) Schematic illustration of the fabrication of activated N–CNFs. (E) TEM image of the activated N–CNFs. (F) Ragone plots showing the power density versus energy density. Reproduced with permission [296]. Copyright 2019, Elsevier.

2767441x, 2026, 3, Downloaded from https://onlinelibrary.wiley.com/doi/10.1002/idm2.70047 by Battelle Memorial Institute Pacific Northwest Division, Wiley Online Library on [22/06/2026]. See the Terms and Conditions (https://onlinelibrary.wiley.com/terms-and-conditions) on Wiley Online Library for rules of use; OA articles are governed by the applicable Creative Commons License

effectively inhibits agglomeration. Using this approach, Liu et al. covered the surface of graphene with highly ordered mesoporous carbon (OMC) by using the interface induced co-assembly method. The alteration increased the specific capacitance of the material by 51.5% over that of pure graphene (Figure 24A) [303]. Similar to graphene, 2D MXenes also suffer from the problem of agglomeration between layers. Using an approach similar to that employed by Wang et al. inserted ordered mesoporous carbon between the MXene carbon layers to form an all-carbon 2D-2D heterogeneous material, which has improved ion diffusion and electron transfer properties [306]. The maximum energy and power densities of supercapacitors assembled utilizing an organic electrolyte are 35.6 Wh/kg and 196.5 kW/kg, respectively. Similarly, Melchior et al. [307] integrated small amounts of carbon nanospheres between the MXene layers to form 2D-2D heterostructured materials for high-voltage symmetric supercapacitor, and reported specific power and specific energy of 37.6 kW/kg and 14.1 Wh/kg, respectively.

In view of the high cost of large-scale applications of graphene and MXenes, an urgent need exists to develop low-cost controllable technologies for preparation of porous carbon nanosheets. He et al. summarized in detail the advantages of using and methods for synthesis of porous carbon nanosheets [308]. Xi et al. described a soft-hard template assisted approach for the preparation of homogeneous hexagonal ordered mesoporous carbon sheets with an average lateral sizes of ~3–4 μm and thicknesses of ~9 nm [309]. The specific capacitance of EDLCs employing these sheets as an electrode material is 208 F/g at 0.2 A/g.

Carbon aerogel, having a hierarchical pore structure, stable 3D cross networking and high conductivity, plays an important role as a material for free-standing EDLC electrodes. Also, by using selected preparation conditions, it is possible to generate carbon aerogels that have hierarchical pore structures that are conducive to rapid adsorption/desorption of electrolyte ions, which leads to maximal specific capacitance of supercapacitors. Investigations have shown that micropores in this material are

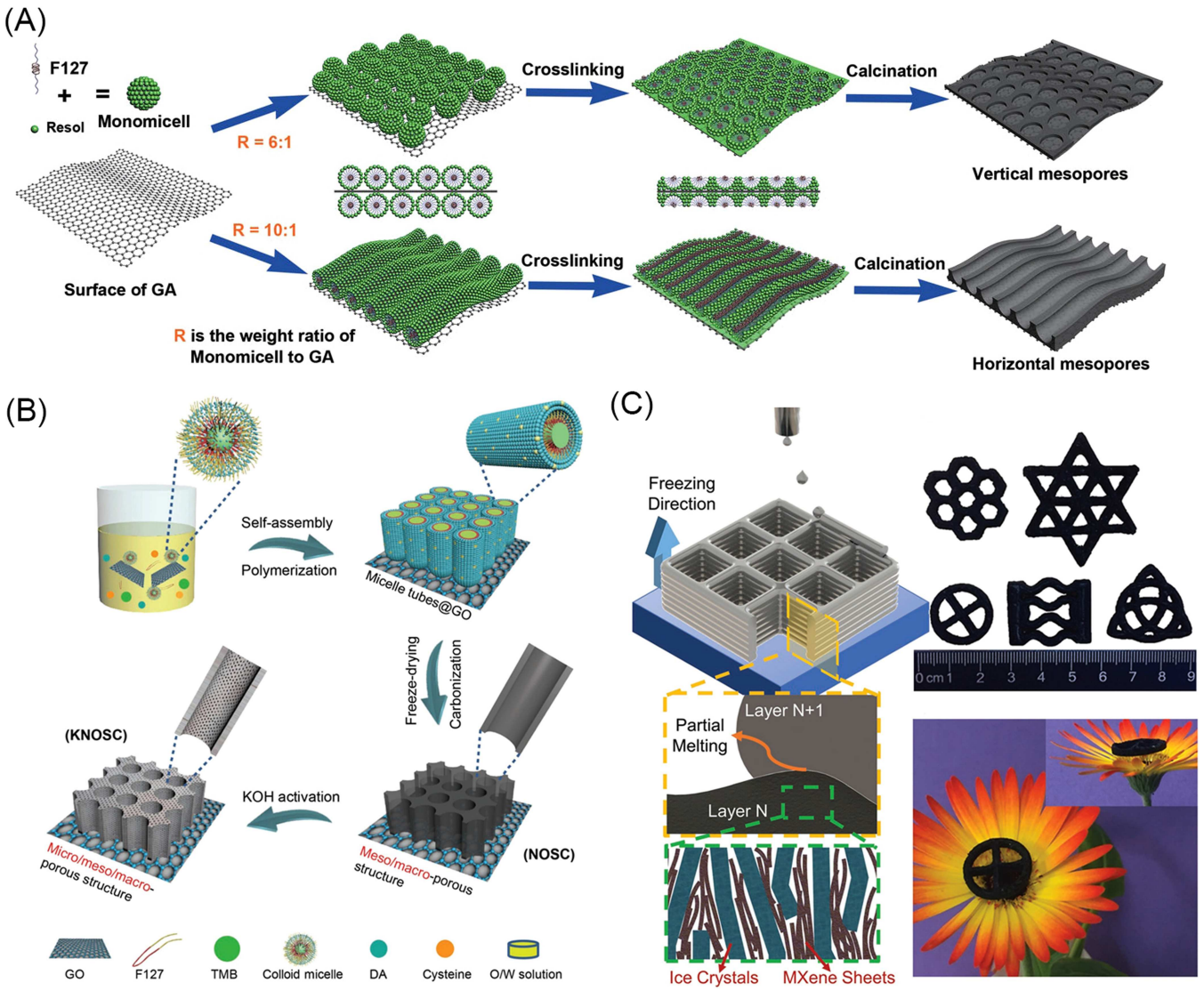

FIGURE 24 | (A) Schematic of the formation of OMC on graphene aerogel. Reproduced with permission [303]. Copyright 2015, Wiley-VCH. (B) Schematic of the synthesis of KNOSC. Reproduced with permission [304]. Copyright 2019, Wiley-VCH. (C) A schematic of the 3DFP process used for fabrication of 3D $Ti_3C_2T_x$ aerogels and a photograph of 3D printed MXene aerogels having various geometries with constant cross-sections. Reproduced with permission [305]. Copyright 2021, Wiley-VCH.

2767441x, 2026, 3, Downloaded from https://onlinelibrary.wiley.com/doi/10.1002/idm2.70047 by Battelle Memorial Institute Pacific Northwest Division, Wiley Online Library on [22/06/2026]. See the Terms and Conditions (https://onlinelibrary.wiley.com/terms-and-conditions) on Wiley Online Library for rules of use; OA articles are governed by the applicable Creative Commons License

the main contributors to capacitance, with mesopores facilitating rapid transfer of electrolyte ions and macropores serving as "small reservoirs" that supply electrolyte ions in a timely manner [310–312]. Using the template method, which is commonly used to prepare hierarchical carbon aerogels, Li's group successfully constructed a multiscale porous carbon foam electrode with a specific surface area of 2905 m^2/g [313]. A supercapacitor that employs this material as an electrode has a specific capacitance of ~375 F/g at 1 A/g. In a later study, this same group created a N, O, S co-doped hierarchical porous carbon foam (KNOSC) by using the soft-template method and demonstrated that it has a macroporous structure including a network of mesoporous channels filled with micropores (Figure 24B) [304]. A symmetrical supercapacitor assembled from this 3D carbon foam can be charged and discharged within 1.52 s, and has a high gravimetric energy density of 15.2 Wh/kg. In addition to the template method, an approach using direct carbonization of melamine sponge has also been applied by Xiao et al. to prepare a porous carbon aerogel. The freestanding, hydrophilic N-doped carbon aerogel prepared using one-step pyrolysis of melamine foam was employed as a component of a high-performance compressible all-solid-state supercapacitor, whose electrochemical performance is unaffected by arbitrary compression under 60% strain [314]. Xu et al. also used sponge loading GO and KOH followed by carbonization to form a 3D hierarchical carbon aerogel [315]. The energy density of symmetric supercapacitor based on the $BMIMPF_6$/AN electrolyte assembly was found to be 89 Wh/kg. Recently, utilization of 3D printing to prepare carbon aerogels has attracted great attention. Tetik et al. developed a 3D freeze-printing (3DFP) method to manufacture an ultralight 3D MXene aerogel, which was utilized to construct an all-solid-state micro-supercapacitor composed of horizontally and vertically aligned MXene sheets (Figure 24C) [305]. Tao et al. obtained 3D carbon materials having both a high porosity and density (1.58 g/cm^3) by evaporation-induced drying of a graphene hydrogel [316]. The volumes energy densities of supercapacitors assembled employing an aqueous system and organic electrolyte are 13.1 and 37.1 Wh/L, respectively. In addition to demonstrating exceptional properties, practical deployment of such nano-engineered carbons hinges on solving challenges related to the high-costs of precursors, controlled large-volume synthesis, and integration of these fragile structures into robust, packaged devices suitable for marine conditions.

4.2.2 | *Pseudocapacitor Materials*

The mechanism for energy storage in pseudocapacitor electrodes is different from those comprised of porous carbon, the latter of which involve Faraday reactions such as reversible oxidation and reduction [317, 318]. Therefore, pseudocapacitors can provide higher specific capacitances and energy densities, but their power densities and cycle stabilities are inferior to those of EDLCs owing to the poor conductivity of active materials and occurrence of irreversible side reactions. The main pseudocapacitor materials include noble metal oxides, transition metal oxides/hydroxides and conductive polymers.

RuO_2, a representative noble metal oxide, has a high theoretical specific capacitance, conductivity and chemical stability. The pseudocapacitance of RuO_2 mainly derives from the surface oxidation–reduction reaction. As a result, its specific capacitance can be effectively improved by altering the specific surface area and crystallinity. RuO_2 with high crystallinity tends to have a large proton diffusion resistance, while its amorphous counterpart displays stable electrochemical performance. Gujar et al. showed that amorphous RuO_2, prepared by using the spray pyrolysis technique, has a highly reversible capacitance in an acidic electrolyte associated with a specific capacitance of 551 F/g [319]. In addition, the presence of bound water is conducive to the diffusion of cations in the active electrode layer of RuO_2. Patil et al. showed that an amorphous, porous and hydrous RuO_2 thin film electrode, generated using chemical bath deposition on a substrate, has excellent specific energy and coulombic efficiency (94%) [320].

Owing to its high cost and scarcity in nature, RuO_2 is often combined with porous carbon, metal oxide or other less expensive materials. Numerous studies have focused on reducing the use of RuO_2 and improving the efficiency of its utilization. Shen et al. reported that an asymmetric supercapacitor electrode, comprised of ultrathin carbon layer encapsulated RuO_2 nanodots anchored in reduced graphene oxide, has an ultrahigh energy density (103 Wh/kg) and cycle stability (100 000 cycles) [321]. Jiang et al. prepared an all pseudocapacitor asymmetric device by combining MXene and RuO_2. This material has 86% capacity retention after 20 000 charge-discharge cycles (Figure 25A–C) [322]. Tan et al. described a series of hollow MO_x-RuO_2 (M = Co, Cu, Fe, Ni and CuNi) nanostructures for use as active electrodes in supercapacitors [325]. This group showed that the specific capacitance of the NiO-RuO_2 composite loaded on CNTs is 740 F/g at 1 A/g. In general, designing highly dispersed nanoscale RuO_2 and selecting a suitable conductive carbon substrate is an ideal approach to improve the performances of supercapacitors.

Transition metal oxides/hydroxides, such as MnO_2, Co_3O_4, Fe_2O_3, NiO and FeOOH, are the most widely studied faradaic materials that can replace RuO_2 in supercapacitors. In particular, MnO_2 has advantages as an electrode material that arise from its high theoretical specific capacitance (~1100 F/g) and abundance, but it also has the disadvantages of poor conductivity and an unstable lattice structure during charge and discharge cycles. Thus far, MnO_2 having different crystal structures (amorphous, α-, β-, γ-, λ- and δ-) and morphologies has been shown to have improved electrochemical performance. Brousse et al. studied the effects of the crystal structure of MnO_2 on electrochemical properties [326]. Matching positive and negative metal oxide capacitances, and voltage is also an important challenge when assembling supercapacitor devices. Taking this requirement into account, several workers have sought measures to enhance manganese oxides as pseudocapacitor electrode materials. For example, Makgopa et al. [327] used highly graphitized onion-like carbon (OLC) to modify birnessite-type MnO_2 to achieve a symmetric pseudocapacitor of high power density of 74.8 kW/kg with excellent capacity retention when subjected to voltage-holding experiments for 50 h. Similarly, OLC was used to modify tetragonal hausmannite Mn_3O_4 and found to perform better than other conventional carbon materials such as CNT, reduced graphene oxide (RGO) and activated carbon (AC). The OLC/Mn_3O_4 nanohybrids gave power density of 52 kW/kg [328]. Liu et al. integrated a MnO_2 nanoflake cathode and Fe_2O_3 nanoparticle anode to form a asymmetric micro-supercapacitor that has a high capacitance of 60 F/cm^3 and high

2767441x, 2026, 3, Downloaded from https://onlinelibrary.wiley.com/doi/10.1002/idm2.70047 by Battelle Memorial Institute Pacific Northwest Division, Wiley Online Library on [22/06/2026]. See the Terms and Conditions (https://onlinelibrary.wiley.com/terms-and-conditions) on Wiley Online Library for rules of use; OA articles are governed by the applicable Creative Commons License

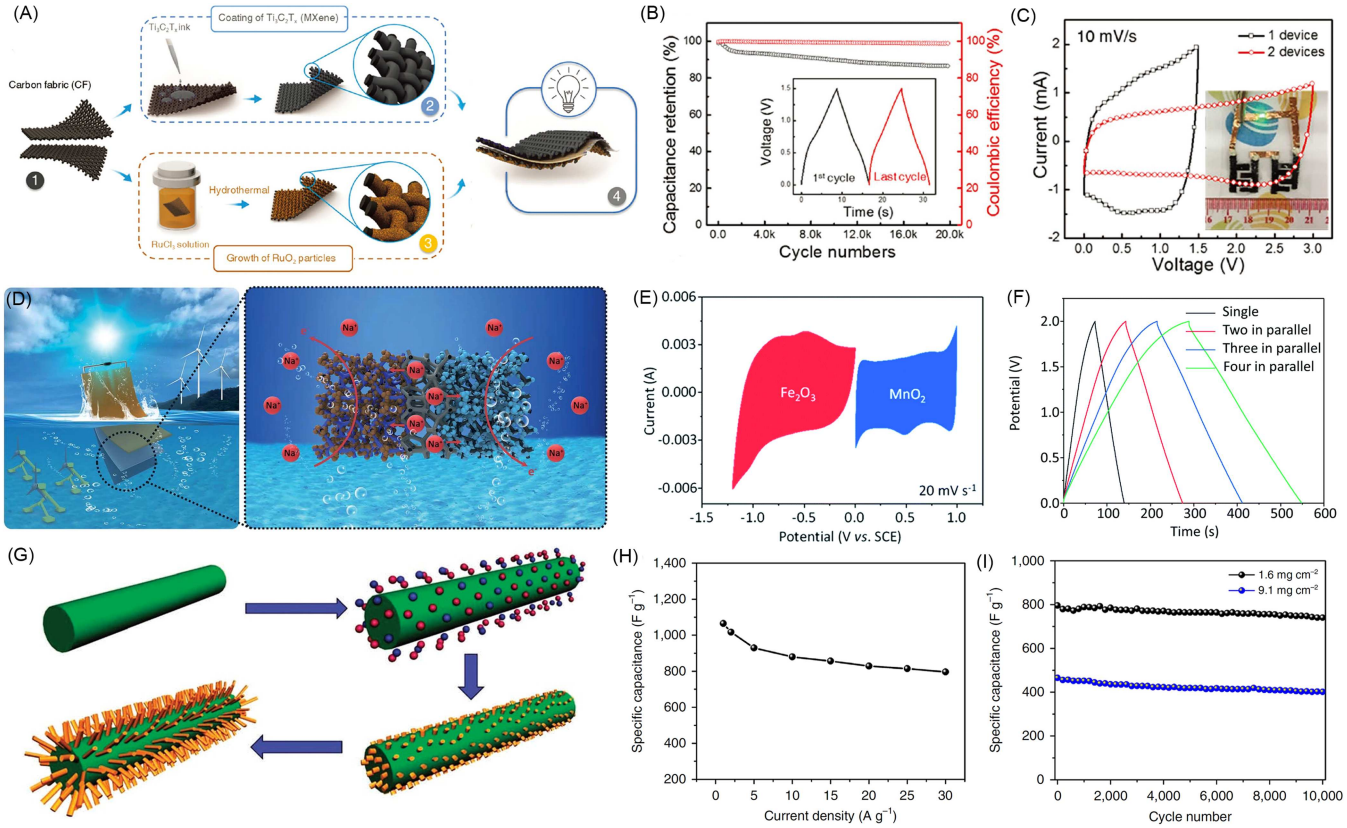

FIGURE 25 | (A) Schematic illustrating fabrication of an asymmetric supercapacitor. (B) Cycling stability and coulombic efficiency of the asymmetric device. (C) Cyclic voltammograms of a RuO_2//$Ti_3C_2T_x$ tandem in-plane device at scan rate of 10 mV/s. Reproduced with permission [322]. Copyright 2018, Wiley-VCH. (D) A schematic illustration of the paper-like all-in-one supercapacitor. (E) CV curves of the Fe_2O_3@CNFs electrode and MnO_2@CNTs electrode at 20 mV/s. (F) Galvanostatic charging–discharging (GCD) curves of the integrated supercapacitor device with the parallel mode recorded at 0.5 A/cm^3. Reproduced with permission [277]. Copyright 2021, Royal Society of Chemistry. (G) Schematic for the construction of hierarchical $MnMoO_4$/$CoMoO_4$ nanowires. Reproduced with permission [323]. Copyright 2011, Springer Nature. (H) Specific gravimetric capacitance as a function of current density. (I) Cycling performance of the FeOOH nanoparticle anode at 1.6 and 9.1 mg/cm^2. Reproduced with permission [324]. Copyright 2017, Springer Nature.

energy density of 12 mWh/cm^2 [329]. For electrochemical energy storage in marine environments, Cheng et al. designed a flexible "paper-like" integrated seawater supercapacitor that has a power density of 99 mW/cm^3 by utilizing MnO_2@CNTs and Fe_2O_3@CNFs as the respective cathode and anode (Figure 25D–F) [277]. In addition, specific morphologies of active materials expose more active specific surface area that improve the ion diffusion rate. Mai et al. showed that hierarchical heterostructured nanowires electrode comprised of the 3D multicomponent oxide, $MnMoO_4$/$CoMoO_4$ (Figure 25G) has a specific capacitance of 187.1 F/g and good cycle reversibility [323]. In a study of materials other than metal oxides, Owusu et al. prepared low-crystalline FeOOH nanoparticles by using hydrothermal growth and electrochemical conversion of α-Fe_2O_3 nanoparticles. This material has a specific capacitance of 1066 F/g and 91% capacitance retention after 10 000 cycles (Figure 25H,I) [324].

Conductive polymers not only play an important role in the field of marine energy conversion and transmission, but they also have a wide range of applications to supercapacitors. The activities of conductive polymers in electrode materials is mainly caused by reversible oxidation/reduction of π-conjugated bonds in polymer chains. Polymers such as PANI, PPy, and PEDOT become attractive faradaic materials due to their high conductivities and specific capacitances. Like other faradaic materials, conductive polymers generally suffer from cyclic instability due to structural degradation of electrodes caused by expansion and contraction during charging and discharging. Therefore, conductive polymers are usually compounded with other materials that complement their electrochemical properties, such as graphene/PANI, CNT/PANI, PANI/MnO_2, PPy/Fe_2O_3, and RuO_2/PEDOT:PSS [330–334]. Snook et al. reviewed the advantages and development prospects of conductive polymers as electrode materials for supercapacitors, and analyzed in detail the electrochemical properties of different polymer composites [335]. Although these materials have great development prospects, efforts are needed to reduce costs and improve cycle stability that will strengthen the possibility of commercialization.

5 | Conclusions and Perspectives

Marine renewable energy is an increasingly important clean energy supply. The total amount of marine energy is very large, but its energy density and utilization efficiency are low. The utilization of marine energy requires integration of ocean, machinery, materials and specific technologies. Importantly, the development of advanced material preparation technologies has promoted an efficient utilization of marine energy in recent years. In the present review, we first summarized materials that are used for marine energy capture and conversion,

2767441x, 2026, 3, Downloaded from https://onlinelibrary.wiley.com/doi/10.1002/idm2.70047 by Battelle Memorial Institute Pacific Northwest Division, Wiley Online Library on [22/06/2026]. See the Terms and Conditions (https://onlinelibrary.wiley.com/terms-and-conditions) on Wiley Online Library for rules of use; OA articles are governed by the applicable Creative Commons License

and then discussed the nature of power generating systems that are based on tidal, wave, ocean current, thermal and salinity gradient energy. Secondly, we summarized materials used for submarine cables for marine energy transmission and discussed HER catalyst materials employed for converting marine energy into portable and storable hydrogen. Finally, we discussed materials storage and utilization of marine energy, focusing on the design and electrochemical performances of electrode materials for use in battery-based energy storage devices.

According to the literature, different material requirements exist for marine energy capture and conversion systems. Coating materials are widely used in power generating, hydraulic turbine equipment and related components. With the prospect of deriving marine energy from deep ocean sources, research and development of multifunctional coating materials having corrosion, fouling and pressure resistance, along with noise reduction properties, and other functions are urgently needed. A critical, parallel priority is the establishment of standardized accelerated testing protocols that can reliably correlate short-term laboratory performance with long-term service life in real marine environments. Moreover, the design of materials that meet the requirements of new marine energy conversion devices is a current focus of studies to improve the efficiency of materials for power generation, such as surface modification, defect engineering, and stress-strain regulation of polymers and carbon materials. For marine energy transmission purposes, submarine cables will be needed in the future for transmission of high voltage and DC power, which place high restrictions on materials used for insulation, compression and wear resistance, and waterproof performance. Large-scale production of high activity, low cost and corrosion resistant HER catalyst materials requires the availability of new electro-active materials. The primary objective is the development of non noble metal catalysts or ultra low loading noble metal systems in which high activity and exceptional stability against chloride corrosion and Mg/Ca precipitate fouling are retained during direct seawater electrolysis under industrial-scale current densities ($> 1\ A/cm^2$). In addition, the availability of high-capacity electrode materials and highly safe electrolytes is a prerequisite for creating high energy density and power density energy storage devices needed for marine energy harvesting and storage. Marine-specific challenges must be addressed through the development of electrode materials and electrolytes that guarantee long-term cyclability and safety under conditions of fluctuating temperature and high humidity.

From an application perspective, materials present distinct trade-offs in performance, cost, and scalability. When used in energy capture and conversion, coatings improve corrosion and fouling resistance, but their durability and large scale cost are concerns. Composites like carbon fiber reinforced polymers offer high strength to weight ratios, but they have high production costs and underdeveloped recycling abilities. In energy transmission, submarine cable materials must combine high insulation, strength, and waterproofing. While cross-linked polyethylene is a commercial material, its long term reliability for high voltage DC use needs further validation. For hydrogen production via seawater electrolysis, noble metal catalysts are efficient but costly and scarce, whereas non noble metal alternatives are more affordable but require improvements in activity and stability in complex seawater. In energy storage, LIBs materials provide high energy density, but have cost and safety limitations for large scale marine use. While supercapacitor carbon materials deliver high power and long cycle life, their lower energy densities limit use in long duration storage. To systematically address these trade-offs and reduce the levelized cost of energy, material design must be tightly coupled with system engineering in future development. This

FIGURE 26 | Future outlook roadmap for marine energy materials.

2767441x, 2026, 3, Downloaded from https://onlinelibrary.wiley.com/doi/10.1002/idm2.70047 by Battelle Memorial Institute Pacific Northwest Division, Wiley Online Library on [22/06/2026]. See the Terms and Conditions (https://onlinelibrary.wiley.com/terms-and-conditions) on Wiley Online Library for rules of use; OA articles are governed by the applicable Creative Commons License

includes the creation of digital twin models in which material degradation data are integrated to predict system lifespan and optimize maintenance, as well as the adoption of circular economy principles through the design for recyclability and the integration of bio-based materials where practicable. Overall, future development must balance performance, cost, scalable manufacturing, and lifecycle environmental impact to enable the shift from laboratory to industry (Figure 26).

Future development of marine energy materials hinges on addressing several unique interdisciplinary core challenges. Future efforts should focus on four key challenges. The first is developing materials capable of withstanding multiple marine environmental stresses simultaneously. The marine environment demands materials that integrate corrosion resistance, biofouling prevention, pressure tolerance, and fatigue resistance. Creating materials with these properties requires deep collaboration between materials science, marine corrosion science, fluid dynamics, and related fields. The second challenge is advancing laboratory materials toward large-scale marine engineering applications. Many high-performance materials (e.g., nanocatalysts, 2D membranes) are only at the laboratory stage of the development. An urgent need exists to develop mass production processes that are scalable, cost-effective, and meet the stringent requirements of marine engineering. A third goal is developing material systems with intelligent response capabilities. Future materials should be able to sense environmental changes, achieve self-healing, or adapt autonomously, thereby enhancing their reliability and operational efficiency for use in marine energy equipment. A final challenge is integrating sustainability and circularity into material designs. Priority should be given to abundantly available elements, designing recyclable composite material systems, and exploring the application of bio-based materials in specific scenarios to achieve green and low-carbon life cycles.

The account given above clearly shows that uncovering materials for exploitation of marine energy is an important interdisciplinary topic, which has epoch-making significance to explorations for solutions that ensure energy security and reduce global carbon emissions.

Acknowledgments

This study was supported by the Major Program (JD) of Hubei Province (2023BAA003), National Natural Science Foundation of China (52130208, 42406221), Key R&D Program of Shandong Province (2023CXGC010314), Laoshan Laboratory (LSKJ202501700), Shandong Institute of Chinese Engineering S&T Strategy for Development (202502SDZD02) and South Africa's DSI-NRF-Wits SARChI Chair in Materials Electrochemistry and Energy Technologies (MEET, UID #132739).

Conflicts of Interest

The authors declare no conflicts of interest.

References

1. J. Gong, C. Li, and M. R. Wasielewski, "Advances in Solar Energy Conversion," *Chemical Society Reviews* 48 (2019): 1862–1864.

2. Y. Kumar, J. Ringenberg, S. S. Depuru, et al., "Wind Energy: Trends and Enabling Technologies," *Renewable and Sustainable Energy Reviews* 53 (2016): 209–224.

3. P. A. J. Bonar, I. G. Bryden, and A. G. L. Borthwick, "Social and Ecological Impacts of Marine Energy Development," *Renewable and Sustainable Energy Reviews* 47 (2015): 486–495.

4. O. Ellabban, H. Abu-Rub, and F. Blaabjerg, "Renewable Energy Resources: Current Status, Future Prospects and Their Enabling Technology," *Renewable and Sustainable Energy Reviews* 39 (2014): 748–764.

5. D. Curto, V. Franzitta, and A. Guercio, "Sea Wave Energy. A Review of the Current Technologies and Perspectives," *Energies* 14, no. 20 (2021): 6604.

6. A. Voss, "Waves, Currents, Tides—Problems and Prospects," *Energy* 4, no. 5 (1979): 823–831.

7. H. Liu, S. Ma, W. Li, H. Gu, Y. Lin, and X. Sun, "A Review on the Development of Tidal Current Energy in China," *Renewable and Sustainable Energy Reviews* 15 (2011): 1141–1146.

8. E. Callaway, "Energy: To Catch a Wave," *Nature* 450 (2007): 156–159.

9. S. H. Salter, "Wave Power," *Nature* 249 (1974): 720–724.

10. M. Rey and F. Lauro, "Ocean Thermal Energy and Desalination," *Desalination* 39 (1981): 159–168.

11. R. E. Pattle, "Production of Electric Power by Mixing Fresh and Salt Water in the Hydroelectric Pile," *Nature* 174 (1954): 660.

12. M. Kadiri, R. Ahmadian, B. Bockelmann-Evans, W. Rauen, and R. Falconer, "A Review of the Potential Water Quality Impacts of Tidal Renewable Energy Systems," *Renewable and Sustainable Energy Reviews* 16, no. 1 (2012): 329–341.

13. S. A. Sannasiraj and V. Sundar, "Assessment of Wave Energy Potential and Its Harvesting Approach Along the Indian Coast," *Renewable Energy* 99 (2016): 398–409.

14. X. Ma, Z. Jing, P. Chang, et al., "Western Boundary Currents Regulated by Interaction Between Ocean Eddies and the Atmosphere," *Nature* 535 (2016): 533–537.

15. N. I. Xiros, "Ocean Renewable Energy," in *Ocean Renewable Energy*, ed. N. I. Xiros (Springer, 2016), 1099–1266.

16. A. Etemadi, A. Emdadi, O. AsefAfshar, and Y. Emami, "Electricity Generation by the Ocean Thermal Energy," *Energy Procedia* 12 (2011): 936–943.

17. N. Y. Yip, D. Brogioli, H. V. M. Hamelers, and K. Nijmeijer, "Salinity Gradients for Sustainable Energy: Primer, Progress, and Prospects," *Environmental Science & Technology* 50, no. 22 (2016): 12072–12094.

18. K. Narula, "Renewable Energy From Oceans," in *The Maritime Dimension of Sustainable Energy Security*, ed. K. Narula (Springer Nature, 2019), 174–175.

19. M. Sharma, A. Chakraborty, J. Kuttippurath, and A. K. Yadav, "Potential Power Production From Salinity Gradient at the Hooghly Estuary System," *Innovative Energy & Research* 7 (2018): 1000210.

20. N. Khan, A. Kalair, N. Abas, and A. Haider, "Review of Ocean Tidal, Wave and Thermal Energy Technologies," *Renewable and Sustainable Energy Reviews* 72 (2017): 590–604.

21. J. Tollefson, "Power From the Oceans: Blue Energy," *Nature* 508 (2014): 302–304.

22. E. De Ranieri, "Marine Energy: In Deep Water," *Nature Energy* 1 (2016): 16007.

23. Z. L. Yong-liang Zhang and Q.-lin Liu, "Marine Renewable Energy in China: Current Status and Perspectives," *Water Science and Engineering* 7 (2014): 288–305.

24. O. Rahman, S. Shi, J. Ding, D. Wang, S. Ahmad, and H. Yu, "Lignin Nanoparticles: Synthesis, Characterization and Corrosion Protection Performance," *New Journal of Chemistry* 42 (2018): 3415–3425.

25. R. Reuben, *Materials in Marine Technology* (Springer, 1994).

2767441x, 2026, 3, Downloaded from https://onlinelibrary.wiley.com/doi/10.1002/idm2.70047 by Battelle Memorial Institute Pacific Northwest Division, Wiley Online Library on [22/06/2026]. See the Terms and Conditions (https://onlinelibrary.wiley.com/terms-and-conditions) on Wiley Online Library for rules of use; OA articles are governed by the applicable Creative Commons License

26. S. Li, K. Feng, J. Li, et al., "Marine Antifouling Strategies: Emerging Opportunities for Seawater Resource Utilization," *Chemical Engineering Journal* 486 (2024): 149859.

27. M. Melikoglu, "Current Status and Future of Ocean Energy Sources: A Global Review," *Ocean Engineering* 148 (2018): 563–573.

28. M. H. Sotoude Haghighi, S. M. Mirghavami, M. M. Ghorani, A. Riasi, and S. F. Chini, "A Numerical Study on the Performance of a Superhydrophobic Coated Very Low Head (VLH) Axial Hydraulic Turbine Using Entropy Generation Method," *Renewable Energy* 147 (2020): 409–422.

29. H. Gonabadi, A. Oila, A. Yadav, and S. Bull, "Structural Performance of Composite Tidal Turbine Blades," *Composite Structures* 278 (2021): 114679.

30. E. Quaranta and P. Davies, "Emerging and Innovative Materials for Hydropower Engineering Applications: Turbines, Bearings, Sealing, Dams and Waterways, and Ocean Power," *Engineering* 8 (2022): 148–158.

31. B. S. Mann and V. Arya, "Abrasive and Erosive Wear Characteristics of Plasma Nitriding and HVOF Coatings: Their Application in Hydro Turbines," *Wear* 249, no. 5–6 (2001): 354–360.

32. B. S. Mann, "High-Energy Particle Impact Wear Resistance of Hard Coatings and Their Application in Hydroturbines," *Wear* 237, no. 1 (2000): 140–146.

33. H. S. Grewal, H. Singh, and A. Agrawal, "Microstructural and Mechanical Characterization of Thermal Sprayed Nickel–Alumina Composite Coatings," *Surface and Coatings Technology* 216 (2013): 78–92.

34. R.-Z. Zhang, Y.-Y. Ren, D.-K. Yan, P.-Y. Guo, and L.-J. Li, "Synthesis of Hydrophobic Fluorinated Polyurethanes and Their Properties of Resistance to Cavitation and Wear," *Progress in Organic Coatings* 104 (2017): 11–19.

35. C. Syamsundar, D. Chatterjee, M. Kamaraj, and A. K. Maiti, "Erosion Characteristics of Nanoparticle-Reinforced Polyurethane Coatings on Stainless Steel Substrate," *Journal of Materials Engineering and Performance* 24 (2015): 1391–1405.

36. V. Rico, J. Mora, P. García, et al., "Robust Anti-Icing Superhydrophobic Aluminum Alloy Surfaces by Grafting Fluorocarbon Molecular Chains," *Applied Materials Today* 21 (2020): 100815.

37. R.-G. J. A. Eslava-Hernandez Abel, Carlos Rubio-Gonzalez, Armando I. Martinez-Perez, and Edgar E. Vera-Cardenas, "Effect of Seawater Aging on the Erosive Wear Response of Aramid Fiber Reinforced Composites," *Journal of Composite Materials* 58 (2024): 1167–1178.

38. F. W. V. Jaksic and C. Ó. Brádaigh, Presented in Part at the 12th European Wave and Tidal Energy Conference (2017).

39. P. Liu, Y. Gao, F. Wang, et al., "Superhydrophobic and Self-Cleaning Behavior of Portland Cement With Lotus-Leaf-Like Microstructure," *Journal of Cleaner Production* 156 (2017): 775–785.

40. N. You, J. Shi, and Y. Zhang, "Corrosion Behaviour of Low-Carbon Steel Reinforcement in Alkali-Activated Slag-Steel Slag and Portland Cement-Based Mortars Under Simulated Marine Environment," *Corrosion Science* 175 (2020): 108874.

41. D. Berman, A. Erdemir, and A. V. Sumant, "Graphene: A New Emerging Lubricant," *Materials Today* 17 (2014): 31–42.

42. K. Gunn and C. Stock-Williams, "Quantifying the Global Wave Power Resource," *Renewable Energy* 44 (2012): 296–304.

43. G. Liu, H. Guo, S. Xu, C. Hu, and Z. L. Wang, "Oblate Spheroidal Triboelectric Nanogenerator for All-Weather Blue Energy Harvesting," *Advanced Energy Materials* 9 (2019): 1900801.

44. H. S. Kim, D. Y. Kim, J. E. Kim, et al., "Ferroelectric-Polymer-Enabled Contactless Electric Power Generation in Triboelectric Nanogenerators," *Advanced Functional Materials* 29 (2019): 1905816.

45. W. Jiang, H. Li, Z. Liu, et al., "Fully Bioabsorbable Natural-Materials-Based Triboelectric Nanogenerators," *Advanced Materials* 30 (2018): e1801895.

46. A. F. O. Falcão, "Wave Energy Utilization: A Review of the Technologies," *Renewable and Sustainable Energy Reviews* 14 (2010): 899–918.

47. B. Drew, A. R. Plummer, and M. N. Sahinkaya, "A Review of Wave Energy Converter Technology," *Proceedings of the Institution of Mechanical Engineers, Part A: Journal of Power and Energy* 223 (2016): 887–902.

48. C. Rodrigues, D. Nunes, D. Clemente, et al., "Emerging Triboelectric Nanogenerators for Ocean Wave Energy Harvesting: State of the Art and Future Perspectives," *Energy & Environmental Science* 13 (2020): 2657–2683.

49. M. Gao, Z. Yang, Y. Pang, et al., "Triboelectric Nanogenerators for Condition Monitoring of Machines, Infrastructure and Environment," *Interdisciplinary Materials* 4 (2025): 645–685.

50. L. Lin, Y. Xie, S. Niu, S. Wang, P. K. Yang, and Z. L. Wang, "Robust Triboelectric Nanogenerator Based on Rolling Electrification and Electrostatic Induction at an Instantaneous Energy Conversion Efficiency of ~55%," *ACS Nano* 9 (2015): 922–930.

51. Y. Jiang, P. Chen, J. Han, et al., "High-Performance Triboelectric Nanogenerator Based on a Double-Spiral Zigzag-Origami Structure for Continuous Sensing and Signal Transmission in Marine Environment," *Interdisciplinary Materials* 4 (2025): 201–212.

52. T. Jiang, H. Pang, J. An, et al., "Robust Swing-Structured Triboelectric Nanogenerator for Efficient Blue Energy Harvesting," *Advanced Energy Materials* 10 (2020): 2000064.

53. X. Li, J. Tao, X. Wang, J. Zhu, C. Pan, and Z. L. Wang, "Networks of High Performance Triboelectric Nanogenerators Based on Liquid-Solid Interface Contact Electrification for Harvesting Low-Frequency Blue Energy," *Advanced Energy Materials* 8 (2018): 1800705.

54. Q. Zheng, L. Fang, H. Guo, et al., "Highly Porous Polymer Aerogel Film-Based Triboelectric Nanogenerators," *Advanced Functional Materials* 28 (2018): 1706365.

55. M. Xu, T. Zhao, C. Wang, et al., "High Power Density Tower-Like Triboelectric Nanogenerator for Harvesting Arbitrary Directional Water Wave Energy," *ACS Nano* 13 (2019): 1932–1939.

56. C. Yao, A. Hernandez, Y. Yu, Z. Cai, and X. Wang, "Triboelectric Nanogenerators and Power-Boards From Cellulose Nanofibrils and Recycled Materials," *Nano Energy* 30 (2016): 103–108.

57. J. Wang, Z. Wen, Y. Zi, et al., "All-Plastic-Materials Based Self-Charging Power System Composed of Triboelectric Nanogenerators and Supercapacitors," *Advanced Functional Materials* 26 (2016): 1070–1076.

58. S. S. Kwak, S. M. Kim, H. Ryu, et al., "Butylated Melamine Formaldehyde as a Durable and Highly Positive Friction Layer for Stable, High Output Triboelectric Nanogenerators," *Energy & Environmental Science* 12 (2019): 3156–3163.

59. L. W. Martin and A. M. Rappe, "Thin-Film Ferroelectric Materials and Their Applications," *Nature Reviews Materials* 2 (2016): 16087.

60. S. Hajra, V. Vivekananthan, M. Sahu, G. Khandelwal, N. P. M. Joseph Raj, and S.-J. Kim, "Triboelectric Nanogenerator Using Multiferroic Materials: An Approach for Energy Harvesting and Self-Powered Magnetic Field Detection," *Nano Energy* 85 (2021): 105964.

61. A. Šutka, K. Mālnieks, A. Linarts, et al., "Inversely Polarised Ferroelectric Polymer Contact Electrodes for Triboelectric-Like Generators From Identical Materials," *Energy & Environmental Science* 11 (2018): 1437–1443.

62. B. Jiang, J. Iocozzia, L. Zhao, et al., "Barium Titanate at the Nanoscale: Controlled Synthesis and Dielectric and Ferroelectric Properties," *Chemical Society Reviews* 48 (2019): 1194–1228.

63. W. Seung, H.-J. Yoon, T. Y. Kim, et al., "Boosting Power-Generating Performance of Triboelectric Nanogenerators via Artificial Control of Ferroelectric Polarization and Dielectric Properties," *Advanced Energy Materials* 7 (2017): 1600988.

2767441x, 2026, 3, Downloaded from https://onlinelibrary.wiley.com/doi/10.1002/idm2.70047 by Battelle Memorial Institute Pacific Northwest Division, Wiley Online Library on [22/06/2026]. See the Terms and Conditions (https://onlinelibrary.wiley.com/terms-and-conditions) on Wiley Online Library for rules of use; OA articles are governed by the applicable Creative Commons License

64. Y. Park, Y. E. Shin, J. Park, et al., "Ferroelectric Multilayer Nanocomposites With Polarization and Stress Concentration Structures for Enhanced Triboelectric Performances," *ACS Nano* 14 (2020): 7101–7110.

65. Y. Jie, X. Jia, J. Zou, et al., "Natural Leaf Made Triboelectric Nanogenerator for Harvesting Environmental Mechanical Energy," *Advanced Energy Materials* 8 (2018): 1703133.

66. Y. Feng, L. Zhang, Y. Zheng, D. Wang, F. Zhou, and W. Liu, "Leaves Based Triboelectric Nanogenerator (TENG) and TENG Tree for Wind Energy Harvesting," *Nano Energy* 55 (2019): 260–268.

67. Y. Chen, Y. Jie, J. Wang, et al., "Triboelectrification on Natural Rose Petal for Harvesting Environmental Mechanical Energy," *Nano Energy* 50 (2018): 441–447.

68. S. An, A. Sankaran, and A. L. Yarin, "Natural Biopolymer-Based Triboelectric Nanogenerators via Fast, Facile, Scalable Solution Blowing," *ACS Applied Materials & Interfaces* 10 (2018): 37749–37759.

69. S. Roy, H.-U. Ko, P. K. Maji, L. Van Hai, and J. Kim, "Large Amplification of Triboelectric Property by Allicin to Develop High Performance Cellulosic Triboelectric Nanogenerator," *Chemical Engineering Journal* 385 (2020): 123723.

70. H.-J. Kim, E.-C. Yim, J.-H. Kim, S.-J. Kim, J.-Y. Park, and I.-K. Oh, "Bacterial Nano-Cellulose Triboelectric Nanogenerator," *Nano Energy* 33 (2017): 130–137.

71. A. Chandrasekhar, N. R. Alluri, B. Saravanakumar, S. Selvarajan, and S.-J. Kim, "A Microcrystalline Cellulose Ingrained Polydimethylsiloxane Triboelectric Nanogenerator as a Self-Powered Locomotion Detector," *Journal of Materials Chemistry C* 5 (2017): 1810–1815.

72. M. Sadoughipour, J. VanZwieten, and Y. Tang, "Drifter-Based Global Ocean Current Energy Resource Assessment," *Renewable Energy* 244 (2025): 122576.

73. A. A. Matarru, M. Syahid, D. Yoesgiantoro, and S. Hadi, "Analyzing Resistance of Al-10Si-5Mg Alloy From Stress Corrosion Cracking for Ocean Current Turbine Applications," *IOP Conference Series: Materials Science and Engineering* 686 (2019): 012016.

74. J. Wang and N. Müller, "Numerical Investigation on Composite Material Marine Current Turbine Using CFD," *Central European Journal of Engineering* 1 (2011): 334–340.

75. J. Wang and N. Müller, "Performance Prediction of Array Arrangement on Ducted Composite Material Marine Current Turbines (CMMCTs)," *Ocean Engineering* 41 (2012): 21–26.

76. Y. Yoshioka, T. Honda, K. Kasamura, Y. Nakashima, H. Higaki, and Y. Nakanishi, "Use of Hydrated Material for Dynamic Seal Faces in Shaft Seal," *Mechanical Engineering Letters* 5 (2019): 19–00001.

77. S. Ke, W. Wen-Quan, and Y. Yan, "Experimental and Numerical Analysis of a Multilayer Composite Ocean Current Turbine Blade," *Ocean Engineering* 198 (2020): 106977.

78. Y. O. Yoshitaka Nakanishi and H. Higaki, Presented in Part at the 3rd International Conference on Renewable Energy Research and Applications, Milwakuee, USA (2014).

79. Y. Wang, X. Liu, T. Chen, et al., "An Underwater Flag-Like Triboelectric Nanogenerator for Harvesting Ocean Current Energy Under Extremely Low Velocity Condition," *Nano Energy* 90 (2021): 106503.

80. K. Rajagopalan and G. C. Nihous, "Estimates of Global Ocean Thermal Energy Conversion (OTEC) Resources Using an Ocean General Circulation Model," *Renewable Energy* 50 (2013): 532–540.

81. Z. Hu, Z. Deng, W. Gao, and Y. Chen, "Experimental Study of the Absorption Refrigeration Using Ocean Thermal Energy and Its Under-Lying Prospects," *Renewable Energy* 213 (2023): 47–62.

82. A. Copping, H. Farr, C. Rumple, K. Park, and Z. Yang, "Feasibility of Multi-Use Ocean Thermal Energy Conversion (OTEC) Platforms," *Journal of Marine Science and Engineering* 14 (2026): 64.

83. A. A. Azmi, T. Yasunaga, K. Fontaine, et al., "Basic Design Optimization of Power and Desalinated Water for Hybrid Cycle Ocean Thermal Energy Conversion System Integrated With Desalination Plant," *Journal of Marine Science and Technology* 29 (2024): 333–352.

84. B. F. Tchanche, G. Lambrinos, A. Frangoudakis, and G. Papadakis, "Low-Grade Heat Conversion Into Power Using Organic Rankine Cycles—A Review of Various Applications," *Renewable and Sustainable Energy Reviews* 15 (2011): 3963–3979.

85. G. J. Snyder and A. H. Snyder, "Figure of Merit *ZT* of a Thermoelectric Device Defined From Materials Properties," *Energy & Environmental Science* 10 (2017): 2280–2283.

86. J. B. Darby, "Ocean Thermal Energy Conversion—Materials Issues," *Journal of Materials for Energy Systems* 6 (1984): 130–137.

87. E. R. Morgan, "Fuel Production Systems for Remote Areas via an Aluminum Energy Vector," *Energy & Fuels* 32 (2018): 9033–9042.

88. D. E. Cavrot, "Economics of Ocean Thermal Energy Conversion (OTEC)," *Renewable Energy* 3 (1993): 891–896.

89. A. Vinoth Jebaraj, L. Ajaykumar, C. R. Deepak, and K. V. V. Aditya, "Weldability, Machinability and Surfacing of Commercial Duplex Stainless Steel AISI2205 for Marine Applications - A Recent Review," *Journal of Advanced Research* 8 (2017): 183–199.

90. A. A. Kholodnyi, Y. I. Matrosov, and S. V. Sosin, "Effect of Molybdenum on Microstructure, Mechanical Properties, and Hydrogen Induced Cracking Resistance of Pipe Steel Plates," *Metallurgist* 61 (2017): 230–237.

91. E. Qin, G. Chen, Z. Tan, and S. Wu, "Shot Peening and Thermal Stress Relaxation in 17-4 PH Stainless Steel," *Journal of Materials Engineering and Performance* 24 (2015): 4578–4583.

92. P. Maj, B. Adamczyk-Cieslak, M. Lewczuk, J. Mizera, S. Kut, and T. Mrugala, "Formability, Microstructure and Mechanical Properties of Flow-Formed 17-4 PH Stainless Steel," *Journal of Materials Engineering and Performance* 27 (2018): 6435–6442.

93. C. Gayner and K. K. Kar, "Recent Advances in Thermoelectric Materials," *Progress in Materials Science* 83 (2016): 330–382.

94. H. J. Goldsmid and R. W. Douglas, "The Use of Semiconductors in Thermoelectric Refrigeration," *British Journal of Applied Physics* 5 (1954): 386–390.

95. C. Han, Q. Sun, Z. Li, and S. X. Dou, "Thermoelectric Enhancement of Different Kinds of Metal Chalcogenides," *Advanced Energy Materials* 6 (2016): 1600498.

96. H.-S. Kim, N. A. Heinz, Z. M. Gibbs, Y. Tang, S. D. Kang, and G. J. Snyder, "High Thermoelectric Performance in $(Bi_{0.25}Sb_{0.75})_2Te_3$ Due to Band Convergence and Improved by Carrier Concentration Control," *Materials Today* 20 (2017): 452–459.

97. T. H. Geballe and G. W. Hull, "Seebeck Effect in Silicon," *Physical Review* 98 (1955): 940–947.

98. J. P. Dismukes, L. Ekstrom, E. F. Steigmeier, I. Kudman, and D. S. Beers, "Thermal and Electrical Properties of Heavily Doped Ge-Si Alloys Up to 1300°K," *Journal of Applied Physics* 35 (1964): 2899–2907.

99. G. H. Zhu, H. Lee, Y. C. Lan, et al., "Increased Phonon Scattering by Nanograins and Point Defects in Nanostructured Silicon With a Low Concentration of Germanium," *Physical Review Letters* 102 (2009): 196803.

100. D. Beretta, N. Neophytou, J. M. Hodges, et al., "Thermoelectrics: From History, a Window to the Future," *Materials Science and Engineering: R: Reports* 138 (2019): 100501.

101. Y. Sun, Z. Wei, W. Xu, and D. Zhu, "A Three-In-One Improvement in Thermoelectric Properties of Polyaniline Brought by Nanostructures," *Synthetic Metals* 160 (2010): 2371–2376.

102. I. Kunadian, R. Andrews, M. Pinar Mengüç, and D. Qian, "Thermoelectric Power Generation Using Doped MWCNTs," *Carbon* 47 (2009): 589–601.

2767441x, 2026, 3, Downloaded from https://onlinelibrary.wiley.com/doi/10.1002/idm2.70047 by Battelle Memorial Institute Pacific Northwest Division, Wiley Online Library on [22/06/2026]. See the Terms and Conditions (https://onlinelibrary.wiley.com/terms-and-conditions) on Wiley Online Library for rules of use; OA articles are governed by the applicable Creative Commons License

103. Y. Yin, B. Tudu, and A. Tiwari, "Recent Advances in Oxide Thermoelectric Materials and Modules," *Vacuum* 146 (2017): 356–374.

104. R. Berthelot, D. Carlier, and C. Delmas, "Electrochemical Investigation of the P2-Na_xCoO_2 Phase Diagram," *Nature Materials* 10 (2011): 74–80.

105. N. Kanas, B. A. D. Williamson, F. Steinbach, et al., "Tuning the Thermoelectric Performance of $CaMnO_3$-Based Ceramics by Controlled Exsolution and Microstructuring," *ACS Applied Energy Materials* 5 (2022): 12396–12407.

106. W. Lu, Z. Ji, L. Pfeiffer, K. W. West, and A. J. Rimberg, "Real-Time Detection of Electron Tunnelling in a Quantum Dot," *Nature* 423 (2003): 422–425.

107. B. Paul, E. M. Björk, A. Kumar, J. Lu, and P. Eklund, "Nanoporous $Ca_3Co_4O_9$ Thin Films for Transferable Thermoelectrics," *ACS Applied Energy Materials* 1 (2018): 2261–2268.

108. Y. Sun, C. Zhang, C. Cao, J. Fu, and L. Peng, "Enhanced Thermoelectric Properties in BiCuSeO Oxyselenides via Zn and S Dual-Site Substitution," *Journal of Electronic Materials* 46 (2017): 5909–5915.

109. B. Zhang, J. Wang, T. Zou, et al., "High Thermoelectric Performance of Nb-Doped $SrTiO_3$ Bulk Materials With Different Doping Levels," *Journal of Materials Chemistry C* 3 (2015): 11406–11411.

110. L. D. Zhao, J. He, D. Berardan, et al., "BiCuSeO Oxyselenides: New Promising Thermoelectric Materials," *Energy & Environmental Science* 7 (2014): 2900–2924.

111. S. Acharya, B. K. Yu, J. Hwang, J. Kim, and W. Kim, "High Thermoelectric Performance of Zno by Coherent Phonon Scattering and Optimized Charge Transport," *Advanced Functional Materials* 31 (2021): 2105008.

112. S. El Oualid, I. Kogut, M. Benyahia, et al., "High Power Density Thermoelectric Generators With Skutterudites," *Advanced Energy Materials* 11 (2021): 2100580.

113. S. Yeon, S. Shin, H. Jo, et al., "p-Type to n-Type Conversion Through the 'Bypass' Phase Transition in the Zintl-Phase Thermoelectric Materials," *Chemistry of Materials* 33 (2021): 6761–6773.

114. B. B. Iversen, A. E. C. Palmqvist, D. E. Cox, et al., "Why Are Clathrates Good Candidates for Thermoelectric Materials?," *Journal of Solid State Chemistry* 149 (2000): 455–458.

115. Y. Du, S. Z. Shen, K. Cai, and P. S. Casey, "Research Progress on Polymer–Inorganic Thermoelectric Nanocomposite Materials," *Progress in Polymer Science* 37 (2012): 820–841.

116. S. Zhang, Z. Fan, X. Wang, Z. Zhang, and J. Ouyang, "Enhancement of the Thermoelectric Properties of PEDOT:PSS via One-Step Treatment With Cosolvents or Their Solutions of Organic Salts," *Journal of Materials Chemistry A* 6 (2018): 7080–7087.

117. S. Horike, Q. Wei, K. Kirihara, M. Mukaida, Y. Koshiba, and K. Ishida, "Anomalous n-Type Conversion of Thermoelectric Polarity in Ionic Hydrogels Using PEDOT:PSS Electrodes," *Journal of Materials Chemistry C* 9 (2021): 15813–15819.

118. M. Fujii, X. Zhang, H. Xie, et al., "Measuring the Thermal Conductivity of a Single Carbon Nanotube," *Physical Review Letters* 95 (2005): 065502.

119. K. A. Ritter and J. W. Lyding, "The Influence of Edge Structure on the Electronic Properties of Graphene Quantum Dots and Nanoribbons," *Nature Materials* 8 (2009): 235–242.

120. Y. Xu, Z. Li, and W. Duan, "Thermal and Thermoelectric Properties of Graphene," *Small* 10 (2014): 2182–2199.

121. T. A. Amollo, G. T. Mola, M. S. K. Kirui, and V. O. Nyamori, "Graphene for Thermoelectric Applications: Prospects and Challenges," *Critical Reviews in Solid State and Materials Sciences* 43 (2017): 133–157.

122. Z. Jia, B. Wang, S. Song, and Y. Fan, "Blue Energy: Current Technologies for Sustainable Power Generation From Water Salinity Gradient," *Renewable and Sustainable Energy Reviews* 31 (2014): 91–100.

123. J. W. Post, J. Veerman, H. V. M. Hamelers, et al., "Salinity-Gradient Power: Evaluation of Pressure-Retarded Osmosis and Reverse Electrodialysis," *Journal of Membrane Science* 288 (2007): 218–230.

124. J. Ju, Y. Choi, S. Lee, and N. Jeong, "Comparison of Fouling Characteristics Between Reverse Electrodialysis (RED) and Pressure Retarded Osmosis (PRO)," *Desalination* 497 (2021): 114648.

125. X. Zhou, W.-B. Zhang, X.-W. Han, et al., "Principles and Materials of Mixing Entropy Battery and Capacitor for Future Harvesting Salinity Gradient Energy," *ACS Applied Energy Materials* 5 (2022): 3979–4001.

126. X. Tong, S. Liu, J. Crittenden, and Y. Chen, "Nanofluidic Membranes to Address the Challenges of Salinity Gradient Power Harvesting," *ACS Nano* 15 (2021): 5838–5860.

127. Y. Zhou and L. Jiang, "Bioinspired Nanoporous Membrane for Salinity Gradient Energy Harvesting," *Joule* 4 (2020): 2244–2248.

128. X. Ma, M. Neek-Amal, and C. Sun, "Advances in Two-Dimensional Ion-Selective Membranes: Bridging Nanoscale Insights to Industrial-Scale Salinity Gradient Energy Harvesting," *ACS Nano* 18 (2024): 12610–12638.

129. J. Hao, Q. Sun, W. Wang, M. Zhao, H. Liu, and X. Sui, "Biomimetic Asymmetric GO/Polymer Nanocomposite Membrane for Energy Harvesting," *Journal of Power Sources* 560 (2023): 232701.

130. Y. Guo, X. Sun, S. Ding, et al., "Charge-Gradient Sulfonated Poly (Ether Ether Ketone) Membrane With Enhanced Ion Selectivity for Osmotic Energy Conversion," *ACS Nano* 18 (2024): 7161–7169.

131. J. Hao, B. Bao, J. Zhou, et al., "A Euryhaline-Fish-Inspired Salinity Self-Adaptive Nanofluidic Diode Leads to High-Performance Blue Energy Harvesters," *Advanced Materials* 34 (2022): e2203109.

132. C. Li, L. Wen, X. Sui, Y. Cheng, L. Gao, and L. Jiang, "Large-Scale, Robust Mushroom-Shaped Nanochannel Array Membrane for Ultrahigh Osmotic Energy Conversion," *Science Advance* 7 (2021): eabg2183.

133. C. Zhang, T. Xiao, B. Lu, J. He, Y. Wang, and J. Zhai, "Large-Area Covalent Organic Polymers Membrane via Sol-Gel Approach for Harvesting the Salinity Gradient Energy," *Small* 18 (2022): e2107600.

134. W. Hu, C. Peng, W. Luo, et al., "Graphene-Based Antibacterial Paper," *ACS Nano* 4 (2010): 4317–4323.

135. C. Li, H. Jiang, P. Liu, et al., "One Porphyrin Per Chain Self-Assembled Helical Ion-Exchange Channels for Ultrahigh Osmotic Energy Conversion," *Journal of the American Chemical Society* 144 (2022): 9472–9478.

136. R. Li, J. Jiang, Q. Liu, Z. Xie, and J. Zhai, "Hybrid Nanochannel Membrane Based on Polymer/MOF for High-Performance Salinity Gradient Power Generation," *Nano Energy* 53 (2018): 643–649.

137. H. Gao, W. Chen, C. Xu, S. Liu, X. Tong, and Y. Chen, "Two-Dimensional $Ti_3C_2T_x$ MXene/GO Hybrid Membranes for Highly Efficient Osmotic Power Generation," *Environmental Science & Technology* 54 (2020): 2931–2940.

138. W. Xin, L. Jiang, and L. Wen, "Two-Dimensional Nanofluidic Membranes Toward Harvesting Salinity Gradient Power," *Accounts of Chemical Research* 54 (2021): 4154–4165.

139. R. Mantovani, "The Otranto-Valona Cable and the Origins of Submarine Telegraphy in Italy," *Advances in Historical Studies* 06 (2017): 18–39.

140. M. Ardelean and P. Minnebo, *HVDC Submarine Power Cables in the World*, (Luxembourg, 2015).

141. K. R. Schell, J. Claro, and S. D. Guikema, "Probabilistic Cost Prediction for Submarine Power Cable Projects," *International Journal of Electrical Power & Energy Systems* 90 (2017): 1–9.

142. Q. Sha, S. Wang, L. Yan, et al., "10,000-h-Stable Intermittent Alkaline Seawater Electrolysis," *Nature* 639 (2025): 360–367.

2767441x, 2026, 3, Downloaded from https://onlinelibrary.wiley.com/doi/10.1002/idm2.70047 by Battelle Memorial Institute Pacific Northwest Division, Wiley Online Library on [22/06/2026]. See the Terms and Conditions (https://onlinelibrary.wiley.com/terms-and-conditions) on Wiley Online Library for rules of use; OA articles are governed by the applicable Creative Commons License

143. X. Ma and C. Jiang, "Global Submarine Cable Network and Digital Divide," *Journal of Geographical Sciences* 35 (2025): 1204–1232.

144. F. Dinmohammadi, D. Flynn, C. Bailey, et al., "Predicting Damage and Life Expectancy of Subsea Power Cables in Offshore Renewable Energy Applications," *IEEE Access* 7 (2019): 54658–54669.

145. M. A. Hamdan, J. A. Pilgrim, and P. L. Lewin, "Analysis of Thermo-Mechanical Stress in Three Core Submarine Power Cables," *IEEE Transactions on Dielectrics and Electrical Insulation* 27 (2020): 1288–1296.

146. K. Yamaguchi, H. Kishi, and T. Nagasawa, "On the Use of Polyethylene Insulation in the Manufacture of Submarine Cables," *IEEE Transactions on Electrical Insulation* EI–12 (1977): 75–79.

147. J. Hao, Z. Liu, R. Liao, and J. Li, "Electro-Thermal Breakdown Measurement of 500 KV Cross-Linked Polyethylene Submarine Cable Insulation Material and Its Lifetime Model Analysis," *IET Science, Measurement & Technology* 14 (2020): 862–869.

148. Z. Zhang, J. Zhao, W. Zhao, et al., "Influence of Morphological Variations on the AC Breakdown of XLPE Insulation in Submarine Cable Factory Joints," *High Voltage* 5 (2020): 69–75.

149. A. M. Pourrahimi, R. T. Olsson, and M. S. Hedenqvist, "The Role of Interfaces in Polyethylene/Metal-Oxide Nanocomposites for Ultrahigh-Voltage Insulating Materials," *Advanced Materials* 30 (2018): 1703624.

150. P. D. Dragic, M. Cavillon, and J. Ballato, "Materials for Optical Fiber Lasers: A Review," *Applied Physics Reviews* 5 (2018): 041301.

151. J. Ballato and P. Dragic, "Materials Development for Next Generation Optical Fiber," *Materials* 7 (2014): 4411–4430.

152. K. Schuster, S. Unger, C. Aichele, et al., "Material and Technology Trends in Fiber Optics," *Advanced Optical Technologies* 3 (2014): 447–468.

153. A. S. L. Gomes, V. L. Da Silva, J. R. Taylor, B. J. Ainslie, and S. P. Craig, "Picosecond Stimulated Raman Scattering in P_2O_5-SiO_2 Based Single Mode Optical Fibre," *Optics Communications* 64 (1987): 373–378.

154. Q. Liao, N.-B. Zhong, X. Zhu, and R. Chen, "High-Performance Biofilm Photobioreactor Based on a GeO_2–SiO_2–Chitosan-Medium-Coated Hollow Optical Fiber," *International Journal of Hydrogen Energy* 39 (2014): 10016–10027.

155. Q. Zu, S. Huang, Y. Zhang, S. Huang, J. Liu, and H. Li, "Compositional Effects on Mechanical Properties, Viscosity, and Crystallization of (Li_2O, B_2O_3, MgO)-Al_2O_3-SiO_2 Glasses," *Journal of Alloys and Compounds* 728 (2017): 552–563.

156. R. Mossadegh, J. S. Sanghera, D. Schaafsma, et al., "Fabrication of Single-Mode Chalcogenide Optical Fiber," *Journal of Lightwave Technology* 16 (1998): 214–217.

157. M. F. Churbanov, "High-Purity Chalcogenide Glasses as Materials for Fiber Optics," *Journal of Non-Crystalline Solids* 184 (1995): 25–29.

158. Y. Yu, X. Gai, P. Ma, et al., "A Broadband, Quasi-Continuous, Mid-Infrared Supercontinuum Generated in a Chalcogenide Glass Waveguide," *Laser & Photonics Reviews* 8 (2014): 792–798.

159. P. Ma, D. Y. Choi, Y. Yu, et al., "Low-Loss Chalcogenide Waveguides for Chemical Sensing in the Mid-Infrared," *Optics Express* 21 (2013): 29927–29937.

160. Y. Yu, X. Gai, T. Wang, et al., "Mid-Infrared Supercontinuum Generation in Chalcogenides," *Optical Materials Express* 3 (2013): 1075–1086.

161. Y. Koike and M. Asai, "The Future of Plastic Optical Fiber," *NPG Asia Materials* 1 (2009): 22–28.

162. Y. Koike and K. Koike, "Progress in Low-Loss and High-Bandwidth Plastic Optical Fibers," *Journal of Polymer Science, Part B: Polymer Physics* 49 (2011): 2–17.

163. Y. Koike, "High-Bandwidth Graded-Index Polymer Optical Fibre," *Polymer* 32 (1991): 1737–1745.

164. A. F. Garito, J. Wang, and R. Gao, "Effects of Random Perturbations in Plastic Optical Fibers," *Science* 281 (1998): 962–967.

165. M. Rothmaier, M. P. Luong, and F. Clemens, "Textile Pressure Sensor Made of Flexible Plastic Optical Fibers," *Sensors* 8 (2008): 4318–4329.

166. H. Xie, Z. Zhao, T. Liu, et al., "A Membrane-Based Seawater Electrolyser for Hydrogen Generation," *Nature* 612 (2022): 673–678.

167. L. Yu, M. Ning, Y. Wang, C. Yuan, and Z. Ren, "Direct Seawater Electrolysis for Hydrogen Production," *Nature Reviews Materials* 10 (2025): 857–873.

168. G. Liu, Y. Xu, T. Yang, and L. Jiang, "Recent Advances in Electrocatalysts for Seawater Splitting," *Nano Materials Science* 5 (2023): 101–116.

169. Y. Kuang, M. J. Kenney, Y. Meng, et al., "Solar-Driven, Highly Sustained Splitting of Seawater Into Hydrogen and Oxygen Fuels," *Proceedings of the National Academy of Sciences* 116 (2019): 6624–6629.

170. C. Zhuang, C. Zhang, D. Zhang, et al., "Role of Transmission Electron Microscopy in Heterogeneous Structural Nanomaterials for Photocatalytic Applications," *Journal of Materials Science & Technology* 239 (2025): 195–233.

171. T. Liu, C. Lan, M. Tang, et al., "Redox-Mediated Decoupled Seawater Direct Splitting for H_2 Production," *Nature Communications* 15 (2024): 8874.

172. W. Tong, M. Forster, F. Dionigi, et al., "Electrolysis of Low-Grade and Saline Surface Water," *Nature Energy* 5 (2020): 367–377.

173. X. He, Y. Yao, M. Zhang, et al., "Engineered PW_{12}-Polyoxometalate Docked Fe Sites on CoFe Hydroxide Anode for Durable Seawater Electrolysis," *Nature Communications* 16 (2025): 5541.

174. D. Yan, X. Cheng, X. Dong, et al., "Engineering W-O-Co Interfacial Electron Bridge in Transition Metal Phosphide/Tungsten Oxide Heterostructure Enables Ampere-Level Hydrogen Production From Seawater Electrolysis," *Applied Catalysis B: Environment and Energy* 384 (2026): 126203.

175. J. Liang, Z. Cai, Z. Li, et al., "Efficient Bubble/Precipitate Traffic Enables Stable Seawater Reduction Electrocatalysis at Industrial-Level Current Densities," *Nature Communications* 15 (2024): 2950.

176. J. Liang, Z. Cai, X. He, et al., "Electroreduction of Alkaline/Natural Seawater: Self-Cleaning Pt/Carbon Cathode and On-Site Co-Synthesis of H_2 and Mg Hydroxide Nanoflakes," *Chem* 10 (2024): 3067–3087.

177. D. Kirk and A. Ledas, "Precipitate Formation During Sea Water Electrolysis," *International Journal of Hydrogen Energy* 7 (1982): 925–932.

178. S. Trasatti, "Work Function, Electronegativity, and Electrochemical Behaviour of Metals," *Journal of Electroanalytical Chemistry and Interfacial Electrochemistry* 39 (1972): 163–184.

179. J. Mahmood, F. Li, S. M. Jung, et al., "An Efficient and pH-Universal Ruthenium-Based Catalyst for the Hydrogen Evolution Reaction," *Nature Nanotechnology* 12, no. issue (2017): 441–446.

180. M. Li, K. Duanmu, C. Wan, et al., "Single-Atom Tailoring of Platinum Nanocatalysts for High-Performance Multifunctional Electrocatalysis," *Nature Catalysis* 2 (2019): 495–503.

181. L. W. Shen, Y. Wang, J. B. Chen, et al., "A RuCoBO Nanocomposite for Highly Efficient and Stable Electrocatalytic Seawater Splitting," *Nano Letters* 23 (2023): 1052–1060.

182. Y. Liu, X. Hu, B. Huang, and Z. Xie, "Surface Engineering of Rh Catalysts With N/S-Codoped Carbon Nanosheets Toward High-Performance Hydrogen Evolution From Seawater," *ACS Sustainable Chemistry & Engineering* 7 (2019): 18835–18843.

183. C. Zhuang, A. Zhang, Y. Zhang, et al., "Photocatalytic Cocatalysts: Classification, Structural Design and Crucial Role in Various Reactions," *Coordination Chemistry Reviews* 542 (2025): 216867.

2767441x, 2026, 3, Downloaded from https://onlinelibrary.wiley.com/doi/10.1002/idm2.70047 by Battelle Memorial Institute Pacific Northwest Division, Wiley Online Library on [22/06/2026]. See the Terms and Conditions (https://onlinelibrary.wiley.com/terms-and-conditions) on Wiley Online Library for rules of use; OA articles are governed by the applicable Creative Commons License

184. X. Duan, Q. Sha, P. Li, et al., "Dynamic Chloride Ion Adsorption on Single Iridium Atom Boosts Seawater Oxidation Catalysis," *Nature Communications* 15 (2024): 1973.

185. N. Cheng, S. Stambula, D. Wang, et al., "Platinum Single-Atom and Cluster Catalysis of the Hydrogen Evolution Reaction," *Nature Communications* 7 (2016): 13638.

186. F. Li, G. F. Han, H. J. Noh, et al., "Balancing Hydrogen Adsorption/Desorption by Orbital Modulation for Efficient Hydrogen Evolution Catalysis," *Nature Communications* 10 (2019): 4060.

187. J. Li, X. Yu, Q. Sun, et al., "Exploring the Predominant Factors Influencing the Oxygen Reduction Performance of PtCo/C Catalysts," *Chemical Research in Chinese Universities* 40 (2024): 753–760.

188. C. Zhuang, W. Li, Y. Chang, et al., "Coordination Environment Dominated Catalytic Selectivity of Photocatalytic Hydrogen and Oxygen Reduction Over Switchable Gallium and Nitrogen Active Sites," *Journal of Materials Chemistry A* 12 (2024): 5711–5718.

189. J. Zheng, Y. Zhao, H. Xi, and C. Li, "Seawater Splitting for Hydrogen Evolution by Robust Electrocatalysts From Secondary M (M = Cr, Fe, Co, Ni, Mo) Incorporated Pt," *RSC Advances* 8 (2018): 9423–9429.

190. H. Li, Q. Tang, B. He, and P. Yang, "Robust Electrocatalysts From an Alloyed Pt–Ru–M (M = Cr, Fe, Co, Ni, Mo)-Decorated Ti Mesh for Hydrogen Evolution by Seawater Splitting," *Journal of Materials Chemistry A* 4 (2016): 6513–6520.

191. J. Du, Z. Li, L. Wang, et al., "Anion Exchange Membrane Seawater Electrolysis at 1.0 A cm^{-2} With an Anode Catalyst Stable for 9000 H," *Advanced Science* 12 (2025): 2416661.

192. Y.-Y. Ma, C.-X. Wu, X.-J. Feng, et al., "Highly Efficient Hydrogen Evolution From Seawater by a Low-Cost and Stable CoMoP@C Electrocatalyst Superior to Pt/C," *Energy & Environmental Science* 10 (2017): 788–798.

193. H. Jin, X. Liu, A. Vasileff, et al., "Single-Crystal Nitrogen-Rich Two-Dimensional Mo_5N_6 Nanosheets for Efficient and Stable Seawater Splitting," *ACS Nano* 12 (2018): 12761–12769.

194. Y. Zhang, P. Li, X. Yang, W. Fa, and S. Ge, "High-Efficiency and Stable Alloyed Nickel Based Electrodes for Hydrogen Evolution by Seawater Splitting," *Journal of Alloys and Compounds* 732 (2018): 248–256.

195. Y. Ma, G. Guan, X. Hao, J. Cao, and A. Abudula, "Molybdenum Carbide as Alternative Catalyst for Hydrogen Production—A Review," *Renewable and Sustainable Energy Reviews* 75 (2017): 1101–1129.

196. T. Liu, H. Liu, X. Wu, et al., "Molybdenum Carbide/Phosphide Hybrid Nanoparticles Embedded P, N Co-Doped Carbon Nanofibers for Highly Efficient Hydrogen Production in Acidic, Alkaline Solution and Seawater," *Electrochimica Acta* 281 (2018): 710–716.

197. Z. Teng, C. Liu, R. Zhang, et al., "In Situ Adsorption of a Lewis Base Triggers Selective Seawater Oxidation Based on the Lattice Oxygen-Mediated Mechanism," *ACS Nano* 19 (2025): 30930–30940.

198. J. Miao, Z. Lang, X. Zhang, et al., "Polyoxometalate-Derived Hexagonal Molybdenum Nitrides (MXenes) Supported by Boron, Nitrogen Codoped Carbon Nanotubes for Efficient Electrochemical Hydrogen Evolution From Seawater," *Advanced Functional Materials* 29 (2018): 1805893.

199. P. Xiao, M. A. Sk, L. Thia, et al., "Molybdenum Phosphide as an Efficient Electrocatalyst for the Hydrogen Evolution Reaction," *Energy and Environmental Science* 7 (2014): 2624–2629.

200. D. J. Li, U. N. Maiti, J. Lim, et al., "Molybdenum Sulfide/N-Doped CNT Forest Hybrid Catalysts for High-Performance Hydrogen Evolution Reaction," *Nano Letters* 14 (2014): 1228–1233.

201. Z. Zhou, M. Benbouzid, J. Frédéric Charpentier, F. Scuiller, and T. Tang, "A Review of Energy Storage Technologies for Marine Current Energy Systems," *Renewable and Sustainable Energy Reviews* 18 (2013): 390–400.

202. M. Li, J. Lu, Z. Chen, and K. Amine, "30 years of Lithium-Ion Batteries," *Advanced Materials* 30 (2018): 1800561.

203. Y. Wang, Y. Song, and Y. Xia, "Electrochemical Capacitors: Mechanism, Materials, Systems, Characterization and Applications," *Chemical Society Reviews* 45 (2016): 5925–5950.

204. S. Li, K. Wang, G. Zhang, et al., "Fast Charging Anode Materials for Lithium-Ion Batteries: Current Status and Perspectives," *Advanced Functional Materials* 32 (2022): 2200796.

205. X. Hu, Z. Wang, H. Zhang, et al., "High-Entropy Design in Battery Materials for High Performance Electrochemical Energy Storage," *Interdisciplinary Materials* 4 (2025): 795–811.

206. Y. Yang, S. Biswas, R. Xu, et al., "Capacity Recovery by Transient Voltage Pulse In Silicon-Anode Batteries," *Science* 386 (2024): 322–327.

207. J. Verma and D. Kumar, "Recent Developments in Energy Storage Systems for Marine Environment," *Materials Advances* 2 (2021): 6800–6815.

208. H. Wang, E. Oterkus, and S. Oterkus, "Peridynamic Modelling of Fracture in Marine Lithium-Ion Batteries," *Ocean Engineering* 151 (2018): 257–267.

209. R. Gitzendanner, F. Puglia, C. Martin, D. Carmen, E. Jones, and S. Eaves, "High Power and High Energy Lithium-Ion Batteries for Under-Water Applications," *Journal of Power Sources* 136 (2004): 416–418.

210. C. Choi, D. S. Ashby, D. M. Butts, et al., "Achieving High Energy Density and High Power Density With Pseudocapacitive Materials," *Nature Reviews Materials* 5 (2019): 5–19.

211. X. Liu, D. Lyu, C. Merlet, et al., "Structural Disorder Determines Capacitance in Nanoporous Carbons," *Science* 384 (2024): 321–325.

212. J. B. Goodenough, "How We Made the Li-Ion Rechargeable Battery," *Nature Electronics* 1 (2018): 204.

213. D. Li, Y. Li, H. Liu, et al., "Constructing Uniform Ionic Conductor Coatings on $LiCoO_2$ Cathode to Realize 4.6 V High-Voltage All-Solid-State Lithium Batteries," *Interdisciplinary Materials* 4 (2025): 775–7785.

214. Y. Wang, Q. Zhang, Z. C. Xue, et al., "An In Situ Formed Surface Coating Layer Enabling $LiCoO_2$ With Stable 4.6 V High-Voltage Cycle Performances," *Advanced Energy Materials* 10 (2020): 2001413.

215. Y.-S. Hong, X. Huang, C. Wei, et al., "Hierarchical Defect Engineering for $LiCoO_2$ Through Low-Solubility Trace Element Doping," *Chem* 6 (2020): 2759–2769.

216. J.-N. Zhang, Q. Li, C. Ouyang, et al., "Trace Doping of Multiple Elements Enables Stable Battery Cycling of $LiCoO_2$ at 4.6 V," *Nature Energy* 4 (2019): 594–603.

217. Q. Liu, X. Su, D. Lei, et al., "Approaching the Capacity Limit of Lithium Cobalt Oxide in Lithium Ion Batteries via Lanthanum and Aluminium Doping," *Nature Energy* 3 (2018): 936–943.

218. Y. Zhang and C. Y. Wang, "Cycle-Life Characterization of Automotive Lithium-Ion Batteries With $LiNiO_2$ Cathode," *Journal of the Electrochemical Society* 156 (2009): A527–A535.

219. M. Bianchini, M. Roca-Ayats, P. Hartmann, T. Brezesinski, and J. Janek, "There and Back Again-The Journey of $LiNiO_2$ as a Cathode Active Material," *Angewandte Chemie International Edition* 58 (2019): 10434–10458.

220. Z. Liu, H. Zhen, Y. Kim, and C. Liang, "Synthesis of $LiNiO_2$ Cathode Materials With Homogeneous Al Doping at the Atomic Level," *Journal of Power Sources* 196 (2011): 10201–10206.

221. C. S. Yoon, M.-J. Choi, D.-W. Jun, et al., "Cation Ordering of Zr-Doped $LiNiO_2$ Cathode for Lithium-Ion Batteries," *Chemistry of Materials* 30 (2018): 1808–1814.

2767441x, 2026, 3, Downloaded from https://onlinelibrary.wiley.com/doi/10.1002/idm2.70047 by Battelle Memorial Institute Pacific Northwest Division, Wiley Online Library on [22/06/2026]. See the Terms and Conditions (https://onlinelibrary.wiley.com/terms-and-conditions) on Wiley Online Library for rules of use; OA articles are governed by the applicable Creative Commons License

222. Z. Su, Z. W. Lu, X. P. Gao, P. W. Shen, X. J. Liu, and J. Q. Wang, "Preparation and Electrochemical Properties of Indium- and Sulfur-Doped $LiMnO_2$ With Orthorhombic Structure as Cathode Materials," *Journal of Power Sources* 189 (2009): 411–415.

223. W. K. Pang, J. Y. Lee, Y. S. Wei, and S. H. Wu, "Preparation and Characterization of Cr-Doped $LiMnO_2$ Cathode Materials by Pechini's Method for Lithium Ion Batteries," *Materials Chemistry and Physics* 139 (2013): 241–246.

224. P. Suresh, A. K. Shukla, and N. Munichandraiah, "Characterization of Zn- and Fe-Substituted $LiMnO_2$ as Cathode Materials in Li-Ion Cells," *Journal of Power Sources* 161 (2006): 1307–1313.

225. X. Zhu, F. Meng, Q. Zhang, et al., "$LiMnO_2$ Cathode Stabilized by Interfacial Orbital Ordering for Sustainable Lithium-Ion Batteries," *Nature Sustainability* 4 (2020): 392–401.

226. F. P. Nkosi, C. J. Jafta, M. Kebede, L. L. le Roux, M. K. Mathe, and K. I. Ozoemena, "Microwave-Assisted Optimization of the Manganese Redox States for Enhanced Capacity and Capacity Retention of $LiAl_xMn_{2-x}O_4$ ($x = 0$ and 0.3) Spinel Materials," *RSC Advances* 5 (2015): 32256–32262.

227. A. B. Haruna, D. H. Barrett, C. B. Rodella, et al., "Microwave Irradiation Suppresses the Jahn-Teller Distortion in Spinel $LiMn_2O_4$ Cathode Material for Lithium-Ion Batteries," *Electrochimica Acta* 426 (2022): 140786.

228. C. Gong, Z. Xue, S. Wen, Y. Ye, and X. Xie, "Advanced Carbon Materials/Olivine $LiFePO_4$ Composites Cathode for Lithium Ion Batteries," *Journal of Power Sources* 318 (2016): 93–112.

229. Y. Wang, Y. Wang, E. Hosono, K. Wang, and H. Zhou, "The Design of a $LiFePO_4$/Carbon Nanocomposite With a Core-Shell Structure and Its Synthesis by an In Situ Polymerization Restriction Method," *Angewandte Chemie International Edition* 47 (2008): 7461–7465.

230. H. Shu, X. Wang, Q. Wu, et al., "Improved Electrochemical Performance of $LiFePO_4$/C Cathode via Ni and Mn Co-Doping for Lithium-Ion Batteries," *Journal of Power Sources* 237 (2013): 149–155.

231. P. Zhang, Y. Wang, M. Lin, D. Zhang, X. Ren, and Q. Yuan, "Doping Effect of Nb^{5+} on the Microstructure and Defects of $LiFePO_4$," *Journal of the Electrochemical Society* 159 (2012): A402–A409.

232. H. C. Shin, W. I. Cho, and H. Jang, "Electrochemical Properties of Carbon-Coated $LiFePO_4$ Cathode Using Graphite, Carbon Black, and Acetylene Black," *Electrochimica Acta* 52 (2006): 1472–1476.

233. B. Zhao, Y. Jiang, H. Zhang, H. Tao, M. Zhong, and Z. Jiao, "Morphology and Electrical Properties of Carbon Coated $LiFePO_4$ Cathode Materials," *Journal of Power Sources* 189 (2009): 462–466.

234. M. Ben Yahia, F. Lemoigno, G. Rousse, F. Boucher, J.-M. Tarascon, and M.-L. Doublet, "Origin of the 3.6 V to 3.9 V Voltage Increase in the $LiFeSO_4$ Cathodes for Li-Ion Batteries," *Energy & Environmental Science* 5 (2012): 9584–9594.

235. L. Zhang, J. M. Tarascon, M. T. Sougrati, G. Rousse, and G. Chen, "Influence of Relative Humidity on the Structure and Electrochemical Performance of Sustainable $LiFeSO_4F$ Electrodes for Li-Ion Batteries," *Journal of Materials Chemistry A* 3 (2015): 16988–16997.

236. K. Amine, "Olivine $LiCoPO_4$ as 4.8 V Electrode Material for Lithium Batteries," *Electrochemical and Solid-State Letters* 3 (1999): 178–179.

237. K. K. Surthi, K. K. Kar, and R. Janakarajan, "Shape Depended Electrochemical Properties of $LiNi_{0.5}Co_{0.5}PO_4$/C Composites for High Voltage Secondary, Flexible Li-Ion Batteries," *Chemical Engineering Journal* 418 (2021): 129362.

238. X. Rui, Q. Yan, M. Skyllas-Kazacos, and T. M. Lim, "$Li_3V_2(PO_4)_3$ Cathode Materials for Lithium-Ion Batteries: A Review," *Journal of Power Sources* 258 (2014): 19–38.

239. Q. Wei, Q. An, D. Chen, et al., "One-Pot Synthesized Bicontinuous Hierarchical $Li_3V_2(PO_4)_3$/C Mesoporous Nanowires for High-Rate and Ultralong-Life Lithium-Ion Batteries," *Nano Letters* 14 (2014): 1042–1048.

240. Y. Sun, Y. Zhou, L. Zhang, Y. Shen, and J. Zeng, "Preparation and Characterization of Lithium-Rich Ternary Cathode Materials Using Novel Chelating Agent and Solvent," *Journal of Alloys and Compounds* 723 (2017): 1142–1149.

241. D. Song, X. Wang, E. Zhou, P. Hou, F. Guo, and L. Zhang, "Recovery and Heat Treatment of the $Li(Ni_{1/3}Co_{1/3}Mn_{1/3})O_2$ Cathode Scrap Material for Lithium Ion Battery," *Journal of Power Sources* 232 (2013): 348–352.

242. B. Wang, F. Zhang, X. Zhou, et al., "Which of the Nickel-Rich NCM and NCA Is Structurally Superior as a Cathode Material for Lithium-Ion Batteries?," *Journal of Materials Chemistry A* 9 (2021): 13540–13551.

243. X. Hou, Y. Huang, S. Ma, X. Zou, S. Hu, and Y. Wu, "Facile Hydrothermal Method Synthesis of Coralline-Like $Li_{1.2}Mn_{0.54}Ni_{0.13}Co_{0.13}O_2$ Hierarchical Architectures as Superior Cathode Materials for Lithium-Ion Batteries," *Materials Research Bulletin* 63 (2015): 256–264.

244. C. J. Jafta, K. Raju, M. K. Mathe, N. Manyala, and K. I. Ozoemena, "Microwave Irradiation Controls the Manganese Oxidation States of Nanostructured ($Li[Li_{0.2}Mn_{0.52}Ni_{0.13}Co_{0.13}Al_{0.02}]O_2$) Layered Cathode Materials for High-Performance Lithium Ion Batteries," *Journal of the Electrochemical Society* 162 (2015): A768–A773.

245. Y. Ou, B. Zhang, R. Zhan, et al., "A Salt-Free Medium Facilitating Electrode Prelithiation Towards Fast-Charging and High-Energy Lithium-Ion Batteries," *Nature Communications* 16 (2025): 7956.

246. Y. P. Wu, E. Rahm, and R. Holze, "Carbon Anode Materials for Lithium Ion Batteries," *Journal of Power Sources* 114 (2003): 228–236.

247. L. Deng, Y. Liu, H. Qi, et al., "A Nanoengineered Lithium-Hosting Carbon/Zinc Oxide Composite Electrode Material for Efficient Non-Aqueous Lithium Metal Batteries," *Nature Nanotechnology* 20 (2025): 1439–1448.

248. Q. Cheng, R. Yuge, K. Nakahara, N. Tamura, and S. Miyamoto, "KOH Etched Graphite for Fast Chargeable Lithium-Ion Batteries," *Journal of Power Sources* 284 (2015): 258–263.

249. Y. Fang, Y. Lv, R. Che, et al., "Two-Dimensional Mesoporous Carbon Nanosheets and Their Derived Graphene Nanosheets: Synthesis and Efficient Lithium Ion Storage," *Journal of the American Chemical Society* 135 (2013): 1524–1530.

250. T.-H. Kim, E. K. Jeon, Y. Ko, B. Y. Jang, B.-S. Kim, and H.-K. Song, "Enlarging the d-Spacing of Graphite and Polarizing Its Surface Charge for Driving Lithium Ions Fast," *Journal of Materials Chemistry A: Materials for Energy and Sustainability* 2 (2014): 7600–7605.

251. B. J. Landi, M. J. Ganter, C. D. Cress, R. A. DiLeo, and R. P. Raffaelle, "Carbon Nanotubes for Lithium Ion Batteries," *Energy & Environmental Science* 2 (2009): 638–654.

252. L. Qie, W. M. Chen, Z. H. Wang, et al., "Nitrogen-Doped Porous Carbon Nanofiber Webs as Anodes for Lithium Ion Batteries With a Superhigh Capacity and Rate Capability," *Advanced Materials* 24 (2012): 2047–2050.

253. Q. Xia, H. Yang, M. Wang, et al., "High Energy and High Power Lithium-Ion Capacitors Based on Boron and Nitrogen Dual-Doped 3D Carbon Nanofibers as Both Cathode and Anode," *Advanced Energy Materials* 7 (2017): 1701336.

254. Z. Tai, M. Shi, S. Chong, et al., "N-Doped ZIF-8-Derived Carbon (NC-ZIF) as an Anodic Material for Lithium-Ion Batteries," *Journal of Alloys and Compounds* 800 (2019): 1–7.

255. H. Shang, Z. Zuo, L. Li, et al., "Ultrathin Graphdiyne Nanosheets Grown In Situ on Copper Nanowires and Their Performance as Lithium-Ion Battery Anodes," *Angewandte Chemie International Edition* 57 (2018): 774–778.

256. J. Ou, Y. Zhang, L. Chen, et al., "Nitrogen-Rich Porous Carbon Derived From Biomass as a High Performance Anode Material for

2767441x, 2026, 3, Downloaded from https://onlinelibrary.wiley.com/doi/10.1002/idm2.70047 by Battelle Memorial Institute Pacific Northwest Division, Wiley Online Library on [22/06/2026]. See the Terms and Conditions (https://onlinelibrary.wiley.com/terms-and-conditions) on Wiley Online Library for rules of use; OA articles are governed by the applicable Creative Commons License

Lithium Ion Batteries," *Journal of Materials Chemistry A* 3 (2015): 6534–6541.

257. R. Chen, R. Luo, Y. Huang, F. Wu, and L. Li, "Advanced High Energy Density Secondary Batteries With Multi-Electron Reaction Materials," *Advanced Science* 3 (2016): 1600051.

258. J. W. Choi and D. Aurbach, "Promise and Reality of Post-Lithium-Ion Batteries With High Energy Densities," *Nature Reviews Materials* 1 (2016): 16013.

259. S. Y. Han, C. Lee, J. A. Lewis, et al., "Stress Evolution During Cycling of Alloy-Anode Solid-State Batteries," *Joule* 5 (2021): 2450–2465.

260. H. Wu and Y. Cui, "Designing Nanostructured Si Anodes for High Energy Lithium Ion Batteries," *Nano Today* 7 (2012): 414–429.

261. Y. Jin, B. Zhu, Z. Lu, N. Liu, and J. Zhu, "Challenges and Recent Progress in the Development of Si Anodes for Lithium-Ion Battery," *Advanced Energy Materials* 7 (2017): 1700715.

262. L. Sun, Y. Liu, R. Shao, J. Wu, R. Jiang, and Z. Jin, "Recent Progress and Future Perspective on Practical Silicon Anode-Based Lithium Ion Batteries," *Energy Storage Materials* 46 (2022): 482–502.

263. M. T. McDowell, S. W. Lee, W. D. Nix, and Y. Cui, "25th Anniversary Article: Understanding the Lithiation of Silicon and Other Alloying Anodes for Lithium-Ion Batteries," *Advanced Materials* 25 (2013): 4966–4985.

264. M. Ko, S. Chae, J. Ma, et al., "Scalable Synthesis of Silicon-Nanolayer-Embedded Graphite for High-Energy Lithium-Ion Batteries," *Nature Energy* 1 (2016): 16113.

265. N. Liu, H. Wu, M. T. McDowell, Y. Yao, C. Wang, and Y. Cui, "A Yolk-Shell Design for Stabilized and Scalable Li-Ion Battery Alloy Anodes," *Nano Letters* 12 (2012): 3315–3321.

266. Z. Liu, D. Guan, Q. Yu, et al., "Monodisperse and Homogeneous SiO/C Microspheres: A Promising High-Capacity and Durable Anode Material for Lithium-Ion Batteries," *Energy Storage Materials* 13 (2018): 112–118.

267. Z. Liu, Y. Zhao, R. He, et al., "Yolk@Shell SiO/C Microspheres With Semi-Graphitic Carbon Coating on the Exterior and Interior Surfaces for Durable Lithium Storage," *Energy Storage Materials* 19 (2019): 299–305.

268. Y. Zhang, G. Hu, Q. Yu, et al., "Polydopamine Sacrificial Layer Mediated Sio_x/C@C Yolk@Shell Structure for Durable Lithium Storage," *Materials Chemistry Frontiers* 4 (2020): 1656–1663.

269. Q. Yu, P. Ge, Z. Liu, et al., "Ultrafine SiO_x/C Nanospheres and Their Pomegranate-Like Assemblies for High-Performance Lithium Storage," *Journal of Materials Chemistry A* 6 (2018): 14903–14909.

270. C. Tang, Y. Liu, C. Xu, et al., "Ultrafine Nickel-Nanoparticle-Enabled SiO_2 Hierarchical Hollow Spheres for High-Performance Lithium Storage," *Advanced Functional Materials* 28 (2018): 1704561.

271. R. Yu, Y. Pan, Y. Liu, et al., "Constructing Sub 10 nm Scale Interfused TiO_2/SiO_x Bicontinuous Hybrid With Mutual-Stabilizing Effect for Lithium Storage," *ACS Nano* 17 (2023): 2568–2579.

272. Z. Liu, Q. Yu, Y. Zhao, et al., "Silicon Oxides: A Promising Family of Anode Materials for Lithium-Ion Batteries," *Chemical Society Reviews* 48 (2019): 285–309.

273. L. Xu, C. Kim, A. K. Shukla, et al., "Monodisperse Sn Nanocrystals as a Platform for the Study of Mechanical Damage During Electrochemical Reactions With Li," *Nano Letters* 13 (2013): 1800–1805.

274. S. Wang, Z. Yi, X. Wang, Q. Sun, Y. Cheng, and L. Wang, "A Rational Design to Buffer Volume Expansion of CoSn Intermetallic in Lithium and Sodium Storage: Multicore-Shell Versus Monocore-Shell," *Energy Storage Materials* 23 (2019): 629–635.

275. Y. Wang, S. Luo, M. Chen, and L. Wu, "Uniformly Confined Germanium Quantum Dots in 3D Ordered Porous Carbon Framework for High-Performance Li-Ion Battery," *Advanced Functional Materials* 30 (2020): 2000373.

276. N. Mahmood, T. Tang, and Y. Hou, "Nanostructured Anode Materials for Lithium Ion Batteries: Progress, Challenge and Perspective," *Advanced Energy Materials* 6 (2016): 1600374.

277. S. Cheng, Z. Dai, J. Fu, et al., "Towards Large-Scale Electrochemical Energy Storage in the Marine Environment With a Highly-Extensible 'Paper-Like' Seawater Supercapacitor Device," *Journal of Materials Chemistry A* 9 (2021): 622–631.

278. J. Yan, Q. Wang, T. Wei, and Z. Fan, "Recent Advances in Design and Fabrication of Electrochemical Supercapacitors With High Energy Densities," *Advanced Energy Materials* 4 (2014): 1300816.

279. D. Liu, Y. Xue, X. Yang, et al., "Flexible Fiber-Shaped Supercapacitors: Structures, Materials, Fabrication Methods, and Applications," *Interdisciplinary Materials* 4 (2025): 377–411.

280. H. Zhang, Y. Zhang, and Z. Wen, "Disorder Over Pore Size: Boosting Supercapacitor Efficiency," *Angewandte Chemie International Edition* 63 (2024): e202411039.

281. M. Xu, Q. Yu, Z. Liu, et al., "Tailoring Porous Carbon Spheres for Supercapacitors," *Nanoscale* 10 (2018): 21604–21616.

282. L. F. Chen, X. D. Zhang, H. W. Liang, et al., "Synthesis of Nitrogen-Doped Porous Carbon Nanofibers as an Efficient Electrode Material for Supercapacitors," *ACS Nano* 6 (2012): 7092–7102.

283. T. Lin, I. W. Chen, F. Liu, et al., "Nitrogen-Doped Mesoporous Carbon of Extraordinary Capacitance for Electrochemical Energy Storage," *Science* 350 (2015): 1508–1513.

284. M. Liu, Y. Xie, F. Liu, et al., "Edge-Rich Graphene Nanomesh Thermally Self-Exfoliated From Metal-Organic Frameworks for Boosting CO_2 Electroreduction," *Advanced Functional Materials* 35 (2025): 2509429.

285. B. R. P. Yip, C. Chen, Y. Jiang, D. Ohayon, G. C. Bazan, and X. Wang, "Aqueous Asymmetric Pseudocapacitor Featuring High Areal Energy and Power Using Conjugated Polyelectrolytes and $Ti_3C_2T_x$ MXene," *Nature Communications* 16 (2025): 7984.

286. W. Fu, E. Zhao, X. Ren, A. Magasinski, and G. Yushin, "Hierarchical Fabric Decorated With Carbon Nanowire/Metal Oxide Nanocomposites for 1.6 V Wearable Aqueous Supercapacitors," *Advanced Energy Materials* 8 (2018): 1703454.

287. C. Schütter, S. Pohlmann, and A. Balducci, "Industrial Requirements of Materials for Electrical Double Layer Capacitors: Impact on Current and Future Applications," *Advanced Energy Materials* 9 (2019): 1900334.

288. D. S. Bin, Z. X. Chi, Y. Li, et al., "Controlling the Compositional Chemistry in Single Nanoparticles for Functional Hollow Carbon Nanospheres," *Journal of the American Chemical Society* 139 (2017): 13492–13498.

289. J. Du, Q. Han, Y. Chen, M. Peng, L. Xie, and A. Chen, "Micro/Meso-Porous Double-Shell Hollow Carbon Spheres Through Spatially Confined Pyrolysis for Supercapacitors and Zinc-Ion Capacitor," *Angewandte Chemie International Edition* 63 (2024): e202411066.

290. S. Huang, D.-D. Ma, S. Zhai, et al., "Kinetics-Controlled Superfast Co-Assembly to Construct Hollow Mesoporous Carbon Spheres for High-Performance Supercapacitors," *Journal of Power Sources* 598 (2024): 234195.

291. T. Wang, Y. Sun, L. Zhang, et al., "Space-Confined Polymerization: Controlled Fabrication of Nitrogen-Doped Polymer and Carbon Microspheres With Refined Hierarchical Architectures," *Advanced Materials* 31 (2019): e1807876.

292. J. Liu, S. Z. Qiao, H. Liu, et al., "Extension of The Stöber Method to the Preparation of Monodisperse Resorcinol–Formaldehyde Resin Polymer and Carbon Spheres," *Angewandte Chemie International Edition* 50 (2011): 5947–5951.

2767441x, 2026, 3, Downloaded from https://onlinelibrary.wiley.com/doi/10.1002/idm2.70047 by Battelle Memorial Institute Pacific Northwest Division, Wiley Online Library on [22/06/2026]. See the Terms and Conditions (https://onlinelibrary.wiley.com/terms-and-conditions) on Wiley Online Library for rules of use; OA articles are governed by the applicable Creative Commons License

293. Q. Yu, D. Guan, Z. Zhuang, et al., "Mass Production of Monodisperse Carbon Microspheres With Size-Dependent Supercapacitor Performance via Aqueous Self-Catalyzed Polymerization," *ChemPlusChem* 82 (2017): 872–878.

294. H. Zhang, O. Noonan, X. Huang, et al., "Surfactant-Free Assembly of Mesoporous Carbon Hollow Spheres With Large Tunable Pore Sizes," *ACS Nano* 10 (2016): 4579–4586.

295. J. Kim, D. Lee, C. Kim, H. Lee, S. Baek, and J. H. Moon, "Electrochemically Active Porous Carbon Nanospheres Prepared by Inhibition of Pyrolytic Condensation of Polymers," *Proceedings of the National Academy of Sciences* 120 (2023): e2222050120.

296. Q. Yu, J. Lv, Z. Liu, et al., "Macroscopic Synthesis of Ultrafine N-Doped Carbon Nanofibers for Superior Capacitive Energy Storage," *Science Bulletin* 64 (2019): 1617–1624.

297. L.-F. Chen, Y. Feng, H.-W. Liang, Z.-Y. Wu, and S.-H. Yu, "Macroscopic-Scale Three-Dimensional Carbon Nanofiber Architectures for Electrochemical Energy Storage Devices," *Advanced Energy Materials* 7 (2017): 1700826.

298. X. Lu, C. Wang, F. Favier, and N. Pinna, "Electrospun Nanomaterials for Supercapacitor Electrodes: Designed Architectures and Electrochemical Performance," *Advanced Energy Materials* 7 (2017): 1601301.

299. X.-Q. Zhang, Q. Sun, W. Dong, et al., "Synthesis of Superior Carbon Nanofibers With Large Aspect Ratio and Tunable Porosity for Electrochemical Energy Storage," *Journal of Materials Chemistry A* 1 (2013): 9449.

300. J. Tan, Y. Han, L. He, et al., "In Situ Nitrogen-Doped Mesoporous Carbon Nanofibers as Flexible Freestanding Electrodes for High-Performance Supercapacitors," *Journal of Materials Chemistry A* 5 (2017): 23620–23627.

301. W. Lu, L. Qu, K. Henry, and L. Dai, "High Performance Electrochemical Capacitors From Aligned Carbon Nanotube Electrodes and Ionic Liquid Electrolytes," *Journal of Power Sources* 189 (2009): 1270–1277.

302. Y. Zhu, S. Murali, M. D. Stoller, et al., "Carbon-Based Supercapacitors Produced by Activation of Graphene," *Science* 332 (2011): 1537–1541.

303. R. Liu, L. Wan, S. Liu, L. Pan, D. Wu, and D. Zhao, "An Interface-Induced Co-Assembly Approach Towards Ordered Mesoporous Carbon/Graphene Aerogel for High-Performance Supercapacitors," *Advanced Functional Materials* 25 (2015): 526–533.

304. H. Peng, B. Yao, X. Wei, et al., "Pore and Heteroatom Engineered Carbon Foams for Supercapacitors," *Advanced Energy Materials* 9 (2019): 1803665.

305. H. Tetik, J. Orangi, G. Yang, et al., "3D Printed MXene Aerogels With Truly 3D Macrostructure and Highly Engineered Microstructure for Enhanced Electrical and Electrochemical Performance," *Advanced Materials* 34 (2022): 2104980.

306. J. Wang, J. Tang, B. Ding, et al., "Hierarchical Porous Carbons With Layer-by-Layer Motif Architectures From Confined Soft-Template Self-Assembly in Layered Materials," *Nature Communications* 8 (2017): 15717.

307. S. A. Melchior, K. Raju, I. S. Ike, et al., "High-Voltage Symmetric Supercapacitor Based on 2D Titanium Carbide (MXene, Ti_2CT_x)/Carbon Nanosphere Composites in a Neutral Aqueous Electrolyte," *Journal of the Electrochemical Society* 165 (2018): A501–A511.

308. Y. He, X. Zhuang, C. Lei, et al., "Porous Carbon Nanosheets: Synthetic Strategies and Electrochemical Energy Related Applications," *Nano Today* 24 (2019): 103–119.

309. X. Xi, D. Wu, L. Han, et al., "Highly Uniform Carbon Sheets With Orientation-Adjustable Ordered Mesopores," *ACS Nano* 12 (2018): 5436–5444.

310. J. Chmiola, G. Yushin, Y. Gogotsi, C. Portet, P. Simon, and P. L. Taberna, "Anomalous Increase in Carbon Capacitance at Pore Sizes Less Than 1 Nanometer," *Science* 313 (2006): 1760–1763.

311. M. D. Levi, S. Sigalov, D. Aurbach, and L. Daikhin, "In Situ Electrochemical Quartz Crystal Admittance Methodology for Tracking Compositional and Mechanical Changes in Porous Carbon Electrodes," *Journal of Physical Chemistry C* 117 (2013): 14876–14889.

312. J. M. Griffin, A. C. Forse, W. Y. Tsai, P. L. Taberna, P. Simon, and C. P. Grey, "In Situ NMR and Electrochemical Quartz Crystal Microbalance Techniques Reveal the Structure of the Electrical Double Layer in Supercapacitors," *Nature Materials* 14 (2015): 812–819.

313. F. Zhang, T. Liu, M. Li, et al., "Multiscale Pore Network Boosts Capacitance of Carbon Electrodes for Ultrafast Charging," *Nano Letters* 17 (2017): 3097–3104.

314. K. Xiao, L. X. Ding, G. Liu, H. Chen, S. Wang, and H. Wang, "Freestanding, Hydrophilic Nitrogen-Doped Carbon Foams for Highly Compressible All Solid-State Supercapacitors," *Advanced Materials* 28 (2016): 5997–6002.

315. J. Xu, Z. Tan, W. Zeng, et al., "A Hierarchical Carbon Derived From Sponge-Templated Activation of Graphene Oxide for High-Performance Supercapacitor Electrodes," *Advanced Materials* 28 (2016): 5222–5228.

316. Y. Tao, X. Xie, W. Lv, et al., "Towards Ultrahigh Volumetric Capacitance: Graphene Derived Highly Dense but Porous Carbons for Supercapacitors," *Scientific Reports* 3 (2013): 2975.

317. V. Augustyn, P. Simon, and B. Dunn, "Pseudocapacitive Oxide Materials for High-Rate Electrochemical Energy Storage," *Energy & Environmental Science* 7 (2014): 1597–1614.

318. M. Salanne, B. Rotenberg, K. Naoi, et al., "Efficient Storage Mechanisms for Building Better Supercapacitors," *Nature Energy* 1 (2016): 16070.

319. T. P. Gujar, V. R. Shinde, C. D. Lokhande, W.-Y. Kim, K.-D. Jung, and O.-S. Joo, "Spray Deposited Amorphous RuO_2 for an Effective Use in Electrochemical Supercapacitor," *Electrochemistry Communications* 9 (2007): 504–510.

320. U. M. Patil, S. B. Kulkarni, V. S. Jamadade, and C. D. Lokhande, "Chemically Synthesized Hydrous RuO_2 Thin Films for Supercapacitor Application," *Journal of Alloys and Compounds* 509 (2011): 1677–1682.

321. B. Shen, X. Zhang, R. Guo, J. Lang, J. Chen, and X. Yan, "Carbon Encapsulated RuO_2 Nano-Dots Anchoring on Graphene as an Electrode for Asymmetric Supercapacitors With Ultralong Cycle Life in an Ionic Liquid Electrolyte," *Journal of Materials Chemistry A* 4 (2016): 8180–8189.

322. Q. Jiang, N. Kurra, M. Alhabeb, Y. Gogotsi, and H. N. Alshareef, "All Pseudocapacitive Mxene-RuO_2 Asymmetric Supercapacitors," *Advanced Energy Materials* 8 (2018): 1703043.

323. L. Q. Mai, F. Yang, Y. L. Zhao, X. Xu, L. Xu, and Y. Z. Luo, "Hierarchical $MnMoO_4/CoMoO_4$ Heterostructured Nanowires With Enhanced Supercapacitor Performance," *Nature Communications* 2 (2011): 381.

324. K. A. Owusu, L. Qu, J. Li, et al., "Low-Crystalline Iron Oxide Hydroxide Nanoparticle Anode for High-Performance Supercapacitors," *Nature Communications* 8 (2017): 14264.

325. Q. Tan, P. Wang, H. Liu, Y. Xu, Y. Chen, and J. Yang, "Hollow MO_x -RuO_2 (M = Co, Cu, Fe, Ni, CuNi) Nanostructures as Highly Efficient Electrodes for Supercapacitors," *Science China Materials* 59 (2016): 323–336.

326. T. Brousse, M. Toupin, R. Dugas, L. Athouël, O. Crosnier, and D. Bélanger, "Crystalline MnO_2 as Possible Alternatives to Amorphous Compounds in Electrochemical Supercapacitors," *Journal of the Electrochemical Society* 153 (2006): A2171–A2180.

2767441x, 2026, 3, Downloaded from https://onlinelibrary.wiley.com/doi/10.1002/idm2.70047 by Battelle Memorial Institute Pacific Northwest Division, Wiley Online Library on [22/06/2026]. See the Terms and Conditions (https://onlinelibrary.wiley.com/terms-and-conditions) on Wiley Online Library for rules of use; OA articles are governed by the applicable Creative Commons License

327. K. Makgopa, P. M. Ejikeme, C. J. Jafta, et al., "A High-Rate Aqueous Symmetric Pseudocapacitor Based on Highly Graphitized Onion-Like Carbon/Birnessite-Type Manganese Oxide Nanohybrids," *Journal of Materials Chemistry A* 3 (2015): 3480–3490.

328. K. Makgopa, K. Raju, P. M. Ejikeme, and K. I. Ozoemena, "High-Performance Mn_3O_4/Onion-Like Carbon (OLC) Nanohybrid Pseudocapacitor: Unravelling the Intrinsic Properties of OLC Against Other Carbon Supports," *Carbon* 117 (2017): 20–32.

329. Z. Liu, X. Tian, X. Xu, et al., "Capacitance and Voltage Matching Between MnO_2 Nanoflake Cathode and Fe_2O_3 Nanoparticle Anode for High-Performance Asymmetric Micro-Supercapacitors," *Nano Research* 10 (2017): 2471–2481.

330. H.-P. Cong, X.-C. Ren, P. Wang, and S.-H. Yu, "Flexible Graphene–Polyaniline Composite Paper for High-Performance Supercapacitor," *Energy & Environmental Science* 6 (2013): 1185–1191.

331. R. Malik, L. Zhang, C. McConnell, et al., "Three-Dimensional, Free-Standing Polyaniline/Carbon Nanotube Composite-Based Electrode for High-Performance Supercapacitors," *Carbon* 116 (2017): 579–590.

332. J. Zhou, L. Yu, W. Liu, et al., "High Performance All-Solid Supercapacitors Based on the Network of Ultralong Manganese Dioxide/Polyaniline Coaxial Nanowires," *Scientific Reports* 5 (2015): 17858.

333. L. Wang, H. Yang, X. Liu, et al., "Constructing Hierarchical Tectorum-Like α-Fe_2O_3/PPy Nanoarrays on Carbon Cloth for Solid-State Asymmetric Supercapacitors," *Angewandte Chemie International Edition* 56 (2017): 1105–1110.

334. C. Zhang, T. M. Higgins, S.-H. Park, et al., "Highly Flexible and Transparent Solid-State Supercapacitors Based on RuO_2/PEDOT:PSS Conductive Ultrathin Films," *Nano Energy* 28 (2016): 495–505.

335. G. A. Snook, P. Kao, and A. S. Best, "Conducting-Polymer-Based Supercapacitor Devices and Electrodes," *Journal of Power Sources* 196 (2011): 1–12.

2767441x, 2026, 3, Downloaded from https://onlinelibrary.wiley.com/doi/10.1002/idm2.70047 by Battelle Memorial Institute Pacific Northwest Division, Wiley Online Library on [22/06/2026]. See the Terms and Conditions (https://onlinelibrary.wiley.com/terms-and-conditions) on Wiley Online Library for rules of use; OA articles are governed by the applicable Creative Commons License